SUB-PIXEL REMOTE SENSING FOR MAPPING AND

MODELLING INVASIVE TAMARIX: A CASE

STUDY IN WEST TEXAS, 1993-2005

DISSERTATION

Presented to the Graduate Council of
Texas State University-San Marcos
in Partial Fulfillment
of the Requirements

for the Degree

DOCTOR OF PHILOSOPHY

by

José L. Silván-Cárdenas, M.E. Eng.

San Marcos, Texas
May 2009

SUB-PIXEL REMOTE SENSING FOR MAPPING AND

MODELLING INVASIVE TAMARIX: A CASE

STUDY IN WEST TEXAS, 1993-2005

Committee Members Approved:

_____

F. Benjamin Zhan, Chair

_____

Le Wang

_____

Mark Fonstad

_____

Kelley A. Crews

Approved:

_____

J. Michael Willoughby
Dean of the Graduate College

To Verónica, Brenda and Victoria, my motivations in life.

ACKNOWLEDGMENTS

Time would fail me to tell of how much help I have received from multitudes of people while working on this dissertation, but thanks to God for letting all these people to come into my life.

To Dr. Carmen Reyes Guerrero for giving me the opportunity to fall in love with geosciences. To my advisor, Dr. Ben Zhan, for his kind support, especially for the assistantship that complemented my income and allowed me to come to Texas State. To my former advisor and committee member, Dr. Le Wang, for all his support, constant encouraging and for sharing his professional experience. It was a great honor to have also Dr. Kelley A. Crews and Dr. Mark Fonstad as part of my evaluation committee. Their relevant critics on my proposal influenced the level achieved in this dissertation and shaped much of the content in Chapter 5. I am also thankful with all my professors for challenging me in my doctoral studies and for their willingness to answer my inquires.

To my dear wife Verónica, for her unconditional love, her invaluable company, and her ever increasing patience. To my daughters who added to my reasons-for-success list and made my life more exciting everyday. To my parents and siblings for their love, sacrifices and patience. To my friends Viviana and

TABLE OF CONTENTS

LIST OF TABLES

LIST OF FIGURES

ABSTRACT

SUB-PIXEL REMOTE SENSING FOR MAPPING AND

MODELLING INVASIVE TAMARIX: A CASE

STUDY IN WEST TEXAS, 1993-2005

by

José L. Silván-Cárdenas, Ph.D.

Texas State University-San Marcos
May 2009

SUPERVISING PROFESOR: F. Benjamin Zhan

A number of economical and environmental issues involved with invasive species worldwide is demanding the analysis of large-scale observations made through remote sensing. The saltcedar invasion in the Western US represents a high priority case where some remote sensing observations can play an important role in both controlling and researching the invasion process. Unfortunately, the analysis of these complex datasets still offers a number of challenges that hinders their widespread adoption. For example, recent studies in remote sensing of vegetation

have proposed a simple parameterization of the light-canopy interaction that would allow more accurate estimations of the relative abundance of plant species. These non-linear mixture models are, however, difficult to invert and their application for large-scale studies is still to be assessed. Furthermore, the accuracy assessment of this new level of information represents a bottleneck for furthering the data analysis. This dissertation reviews and tests a number of existing and custom-developed methods for studying the saltcedar invasion along the Rio Grande in West Texas. These techniques include cross-comparison matrices for assessing the accuracy of sub-pixel land cover classifications (Chapter 2), methods for retrieving the sub-pixel canopy coverage of saltcedar and associated native species (Chapter 3), a post-classification change detection method based on sub-pixel maps (Chapter 4) and a metapopulation model for linking remote sensing land cover change to population dynamics (Chapter 5). It is shown how moderate resolution observations from Landsat satellite coupled with sub-pixel techniques can provide a cost-effective means to support control efforts by providing continuous monitoring of its distribution, as well as a way to study its invasion by providing information on location, abundance, and rate of change, which are particularly useful for a factorial analysis and for the assessment of its impacts on the water availability. A spatially explicit metapopulation model is introduced as a means to enable remote sensing to access population parameters along the riparian corridor and as hypothesis-testing framework for general invasion processes. The analysis of multitemporal Landsat images allowed to assess the status of invasion long a segment of the Rio Grande river, from Candelaria, Texas to Presidio, Texas.

The observations support prior in-situ observations on saltcedar dynamics and its competitive superiority over the native species. Although not extensively tested, the metapopulation model has led to the identification of conditions for invasiveness under competition and could be potentially useful to explain distribution patterns observed through remote sensing.

Chapter 1

INTRODUCTION

1.1 Problem overview

Around 20% percent of species in any given country are estimated to be non-native, which represents a significant component of global change and a major cause of species extinction (Alpert *et al.*, 2000; Drake *et al.*, 1989; Vitousek *et al.*, 1996). A general consensus is that the negative ecological and economical implications of most non-native invasive species surpass their beneficial use by humans. Among other things, newly introduced species may act as vectors of disease, drive native species to extinction, reduce biodiversity and alter ecosystems by depleting resources. They also imply tremendous costs from direct loss of affected crops, rangelands and commercial forrests, as well as from expenses associated with controlling the invasion. In the United States the overall economic loss due to the presence of invasive species is estimated over $137 billion per year, greater than all other natural disasters combined (National Invasive Species Council, 2001).

Indeed, most riparian systems in the Western US have undergone extensive changes in flow regimes over the past 100 years, due primarily to human impacts resulting from water storage and diversion projects. Human-induced flow regimes have created conditions unfavorable to most native species that are adapted to

predictable spring flooding caused by snowmelt (Howe and Knopf, 1991). This has resulted in the explosive colonization of riparian habitats by a number of exotic species. One of the greatest invasive threats to western riparian systems is from saltcedar (*Tamarix* spp.), an exotic shrub native to Eurasia that has been subject to many control and environmental restoration efforts since the 1960s (Shafroth *et al.*, 2005). The Rio Grande (or Rio Bravo del Norte in Mexico) has not been the exception to saltcedar invasion (Busch and Smith, 1995; Everitt, 1998; Howe and Knopf, 1991). As a matter of fact, the Rio Grande was recently identified as the most vulnerable site to saltcedar in the nation (Morisette *et al.*, 2006), where the most recurrent issue linked to saltcedar invasion is a decrease in water quantity and quality due to its higher water consumption rates (Brotherson and Field, 1987; Cleverly *et al.*, 2002; Di Tomaso, 1998; Everitt, 1998; Smith *et al.*, 1998).

The efficient control of invasive species demands early discovery and continuous monitoring of their spread (Lass *et al.*, 2005). However, performing frequent and detailed assessment of species distribution in order to conduct scientifically sound environmental management can be prohibitively expensive by direct means (Hunt *et al.*, 2003; Turner *et al.*, 2003). Therefore, remote sensing, coupled with other geospatial technologies, provides a practical means for collecting information on species abundance and distribution, which represents a departure point for analyzing the factors that affect their spread and assessing their impacts on native ecosystems (Joshi *et al.*, 2004). This approach, among other things, increases accessibility to remote and dangerous places, increases area coverage, allows consistency in repetitive observations, improves spatial resolution

and geometric fidelity, and provides continuous monitoring capability.

1.2 Context and related works

1.2.1 A review on saltcedar invasion

Eight species of the genus *Tamarix*, family *Tamaricaceae*, were introduced into the US since early 1800's from Eurasia. These species were originally used as agent of erosion prevention of river banks, as wind shields and for ornamentation (Baum, 1967). According to herbarium collections, saltcedar escaped cultivation by the 1870's, but its spread was slow and almost unnoticed until the 1920's when its proliferation and associated problems were more evident (Brotherson and Field, 1987). To date, saltcedar extent is estimated to exceed 600,000 ha (1.5 million acres) only in the Southwestern US, but its range has continued to expand northward into Montana and Canada (Pearce and Smith, 2003), and southward into northwestern Mexico, reaching elevations as high as 2,135 m (Di Tomaso, 1998). Of the eight introduced species, three are more weedy and more widely distributed across north America (*T. parviflora* DC., *T. ramosissima* Ledeb, *T. chinensis* Lour[1]), but all invasive forms have similar ecological relationships (Di Tomaso, 1998). *T. chinensis* which is native to China, Mongolia, and Japan, and *T. ramosissima*, which is widespread from eastern Turkey to Korea (Baum, 1967), are the most difficult to distinguish from each other and are more widely distributed in the Southwestern US. Interestingly, the most common saltcedar plant in the US invasion is a hybrid combination of these two species, which are

---

[1]These three species together with the hybrids are collectively referred to as saltcedar throughout this dissertation. Other common names found in the literature are salt cedar, tamarisk and tamarix.

geographically isolated in their native Eurasian range (Gaskin and Schaal, 2002).

The impacts of saltcedar on native ecosystems are well documented (Brotherson and Field, 1987; Busch and Smith, 1995; Di Tomaso, 1998; Smith *et al.*, 1998). Saltcedar grows faster than the native plants, including cottonwood (*Populus* spp.), willow (*Salix* spp.) and mesquite (*Prosopis* spp.), and can quickly form dense stands, out-competing native plants for sunlight, moisture, and nutrients. The plant brings salts to the surface by excreting it through the leaves and dropping into the soil surface below the canopy. Only xeric species (plants requiring little water) or halophytes (salt-tolerant species) can tolerate the understory environment of saltcedar thus excluding most native species (Brotherson and Field, 1987). Furthermore, leave-drop increases combustible materials at the plant base. Over the years, this material builds-up and dries creating a surface that fuels allowing wildfire to move between contiguous saltcedar plants even when there is no wind to move the fire. Fire kills all above the ground, but root reserves quickly output dense shoots and growth (Stenquist, 2000). The hydrological implications of saltcedar invasion are perhaps the most worrying. The invasion of floodplain or river bank usually leads to depletion of stream/river flow, lower water table, increase the area inundated by floods due to clogging of stream channels, and increase sediment production leading to poor water quality (Di Tomaso, 1998; Smith *et al.*, 1998). It also endangers fish by changing stream morphology and diminishes human enjoyment of and interaction with the river environment (Tamarisk Coalition, 2003). As saltcedar moves into adjacent upland habitats, it consumes even more water as it replaces the native

grass/sage/rabbit brush plant communities which are low water consumers. Although estimates on water consumption by saltcedar and associated species vary greatly depending on location, maturity, density, and depth to groundwater, a reasonable estimation indicates an over-consumption of saltcedar over 1 foot per year for riparian areas and 4 feet per year for upland areas (Tamarisk Coalition, 2003). Nonetheless, as the water table declines, its deep root system (of up to 100 feet) enables it to survive where some native species cannot.

The negative effects of saltcedar on native ecosystems are not compensated with its ecological value. The wildlife species diversity tied to saltcedar is remarkably low compared to that of native riparian vegetation. Wildlife habitat of saltcedar is limited to screening cover for mammals, nesting sites for some birds, including the endangered southwestern willow flycatcher, and pollen source for bees (Stenquist, 2000).

1.2.2 A review on remote sensing of saltcedar

One of the first approximations for species occurrence has been land cover analysis, along which remote sensing research has flourished since its early years. Other indirect approaches that provide the potential to infer species composition are based on remote sensing of primary productivity, climate, and habitat structure (Turner *et al.*, 2003). As technology and methods become more sophisticated, the capability for direct detection down to the individual level improves. A promising approach to detect vegetation down to species level is the remote sensing of phenological change, including fruiting/flowering events and

early/late onset greenness or senescence (Turner *et al.*, 2003). In particular, saltcedar has been identified using the unique orange-brown color prior to leaf drop which contrasts with the greenish and darker tones of associated native species (Everitt, 1996; Everitt and DeLoach, 1990; Everitt *et al.*, 1992). Although the improved quality, lower costs, and increasing availability of remote sensing data, which also concur with the development of more accessible geographic information systems (GIS), are providing historic opportunity for advancing applications in mapping and modelling distribution of invasive species, the progress has been slow, perhaps due to the lack of an integrative approach (Joshi *et al.*, 2004). To date, remote sensing has been successfully applied for direct detection of canopy-dominant plant species, but limitations still exist when it comes to detecting understory plants or animal species (Joshi *et al.*, 2004). In these cases, however, educated guesses made through indirect approaches and supported with field observations can be equally valuable (Turner *et al.*, 2003).

Early work on remote sensing of saltcedar was based on aerial photography. Aerial photographs have been useful to detect a number of weeds having unique growth patterns different from surrounding vegetation, such as saltcedar (Everitt, 1996; Lass *et al.*, 2005). Unfortunately, the high-cost of color infrared film and processing, variable interpretation, and the requirement for manual scanning or digitizing to use in a GIS prevented their extensive use for weed detection in rangelands and pastures (Lass *et al.*, 2005). Carruthers *et al.* (2006) assessed the spectral separability of scanned aerial photographs and found limitations in separating saltcedar from surrounding habitats along Cache Creek, in California.

However, they showed that separability can be improved when texture information is also used for automatic interpretation (Carruthers *et al.*, 2006). Digital camera photography and videography were introduced as inexpensive, easily available and flexible alternatives to standard photography. Everitt *et al.* (1992) introduced videography to detect weedy species, including saltcedar, along the Rio Grande near Yuma, Arizona, and Presidio, Texas. Assessment of computer classifications of digitized conventional color video images showed higher false detections than omissions (overestimation error was around 6.2% of the total area mapped) and identified the reddish soils and some dry vegetation as major sources of confusion (Everitt *et al.*, 1992). Later on, the integration of GPS technology with videography allowed researchers to geo-reference video frames for producing regional maps of saltcedar infestations along the Colorado River in southwestern Arizona and the Rio Grande in West Texas (Everitt, 1996). Unfortunately, the coarse spectral resolution of these sensors (with typically 1 to 4 wide bands) tends to limit its application for species identification.

With the advent of hyperspectral sensors, which can measure from a few dozen to several hundreds of narrow bands of the electromagnetic spectrum, came the potential to identify unique spectral signatures of invasive plants relative to background of native species. However, the methods for processing these type of data are still *ad hoc* and generally more complex. High spatial resolution hyperspectral sensors have been recently assessed for mapping saltcedar in riparian habitats of Southern California (Hamada *et al.*, 2007) and have been found effective for saltcedar bio-control assessment (Carruthers *et al.*, 2006). Although

overall accuracies as high as 95% have been reported for classification from hyperspectral sensors, results have also indicated that the price of higher accuracies includes larger false detections and higher processing times (Hamada *et al.*, 2007). Therefore, the application of this approach in monitoring large geographical regions is still unfeasible due primarily to the high volume of data and the lack of efficient methods for accurate detection.

Alternatives to airborne sensors are space-borne sensors mounted on satellites orbiting the Earth. Examples of satellites include the Landsat and SPOT series. These type of remote sensing systems have the advantages of covering larger spatial extents and providing continuous monitoring capability while maintaining spatial and temporal consistency. Nevertheless, their relatively coarse resolution had limited their application to the detection of relatively large stands of weeds (Hunt *et al.*, 2003). High-spatial resolution space-borne sensors are also available from commercial satellites such as IKONOS and Quickbird. IKONOS records four visible or near-infrared (NIR) channels of data at 4-m resolution and one panchromatic channel with 1-m resolution over an 11-km swath. Quickbird records one 61-cm panchromatic and four 2.44-m VNIR channel images over a 16.5-km swath. Data from both IKONOS and Quickbird sensors have been used for detecting individual species and capturing plant phenological state (Turner *et al.*, 2003). National Aerospace Administration (NASA)'s EO-1 satellite is carrying the Advanced Land Imager (ALI) and Hyperion instruments. The ALI sensor provides 10 bands including a panchromatic with 10-m spatial resolution and a thermal band with 30-m spatial resolution. The Hyperion instrument is a

grating imaging spectrometer that possesses a 30 meter ground sample distance over a 7.7-km swath. It provides 10-nm contiguous bands (up to 220 spectral bands) of the solar reflected spectrum from 400 nm to 2500 nm. The effectiveness of these sensors in detecting saltcedar is still to be seen.

With so many sensors already operating and many others under development, there is an increasing need for more effective, ready-to-use techniques that can aid to embrace the new technologies for invasive species management and research.

1.2.3   Status of the study site

The Rio Grande, with its 3034 km (1885 miles) length, is the third longest river system in the United States and one of the American Heritage Rivers since 1997. Its headwaters are situated in the southern Colorado Rockies surrounding the San Juan Valley. From El Paso, Texas, to the Gulf of Mexico, the river forms the international boundary between the US and Mexico since 1848. The twin cities of El Paso-Juarez, with their more than 1.5 million inhabitants, represent the largest site where the river is heavily used. With no tributary to replace the water withdrawn for irrigation, the river frequently dries up by the time it reaches Fort Quitman, Texas. The major tributary, the Rio Conchos, enters at Ojinaga, Chihuaha, below Presidio, Texas, and supplies most of the water in the Texas-Mexico border segment. The 320-kilometer (200-mile) stretch of the river that flows from Fort Quitman, below El Paso-Juarez, to its confluence with the Rio Conchos at Presidio-Ojinaga has been called the "Forgotten River" due to the

little research performed in it and the absence of important cities along its way (Harris, 1999). In this site, the river channel has been taken over by dense thickets of saltcedar, and the native cottonwood (*Populus* spp.), that once dominated the area, is completely absent.

The present state of the Forgotten River reach may be attributed to 125 years of water development, which resulted in over appropriation of this resource and a consequent transformation of the river's hydraulic and ecological capacities. In 1915, Elephant Butte reservoir was built upstream of El Paso/Juarez area, causing most of the sediment load to drop into the dam. The construction of the dam was not the only factor that impacted the river flow. In 1926 saltcedar trees were deliberately brought in to the middle Rio Grande as a soil conservation experiment (Everitt, 1998). In 1942 two successive flood events caused Elephant Butte to spill. This dramatically increased the presence of saltcedar in the area, and dug a deeper channel decreasing the average channel width from 30 meters to 10 meters (Everitt, 1998; Harris, 1999). After this flood event, in 1951-1958, an extended drought existed that caused zero flows for 10 consecutive months. This extreme drought killed most of the native vegetation and provided a growth advantage to the invasive saltcedar, which is able to get water by extending its root system to reach falling water tables (Di Tomaso, 1998).

Reeling from a decade of severe drought and over-use, the river failed to reach the Gulf of Mexico for the first time in recorded history in the summer of 2001. The event repeated in the summer of 2002. As of 2008, when this dissertation is written, the river reaches the Gulf of Mexico once again. However,

the full irrigation utilization, increased riparian evapotranspiration, and long lasting droughts have led ecologists to fear an imminent extinction of the river were no strict water conservation measures adopted.

1.3   Study objectives and research questions

The recent advancements in sub-pixel mapping techniques have increased potential for moderate spatial resolution sensors for weed detection. However, the adoption of these techniques in management operations is still hindered by the lack of standardized procedures for accuracy assessment, change detection analysis, and modelling. It is along these research lines that the main contribution of this dissertation fits.

Specifically, this dissertation aims at providing answers to the following research questions: How can saltcedar mapping be improved using recent developments on spectral mixture analysis and multiple scattering concepts? How can the accuracy of these representations be assessed in a way that is consistent with the standardized confusion matrix of crisp classifications? How can these representations be useful to study invasion dynamics, support control efforts, and contribute to conservation of native ecosystems? Can moderate resolution observations confirm known trends in saltcedar occurrence, dynamics and impacts? What are the most important environmental factors that may be driving saltcedar dynamics? How can this new level of information and knowledge in analysis and modelling may help to advance theoretical concepts related to invasive species?

The general research objective of this dissertation is to develop and test

new remote sensing methods that may assist in facing saltcedar invasion along the Rio Grande. However, in order to look for appropriate answers to main research question posed above, this dissertation has the following specific objectives:

1. Review the existing methods for sub-pixel accuracy assessment, identify limitations and needs, and develop theoretical grounds for a more general framework.

2. Assess existing and newly developed methods for sub-pixel detection of saltcedar, particularly toward understanding the role of incorporating recent models of multiple scattering phenomena on the detection accuracy, and determining the advantages and practical implications of incorporating such non-linear relationships for regional mapping applications.

3. Apply sub-pixel change detection analysis of moderate resolution observations in order to identify the role of environmental factors affecting saltcedar spread and the impacts of its spread on the water availability along a riparian habitat.

4. Develop a spatially explicit model that can incorporate the main factors involved in plant invasion process and competition concepts, determine, by using computer simulations, conditions for invasiveness of saltcedar under competition of a native species prototype, and identify ways in which available remote sensing observations and environmental measurements may enhance the model-based research.

1.4 Relevance and contributions

The relevance of remote sensing of invasive species research is made evident by the exponential increment in the number of related publications during the past two decades (Joshi *et al.*, 2004; Lockwood *et al.*, 2007). The beginning of this increased interest on invasive species coincides with the publication of a whole series of books and journal articles on the topic produced by the Scientific Committee on Problems of the Environment (SCOPE) in mid-1980's (www.icsu-scope.org). Furthermore, invasive species research is currently one of the twelve elements of application of national priority identified by NASA's Applied Science Program (http://nasascience.nasa.gov/earth-science). Therefore, the topic is pertinent and tuned with ongoing efforts for building capabilities to detect and predict invasive species by a number of government agencies such as NASA's Office of Earth System Science and the US Geological Survey which are currently developing the Invasive Species Forecasting System (ISFC, 2008). By using remote sensing products coupled with ecological models, the ISFS is aimed at providing regional-scale distributions of invasive species such as saltcedar while identifying the most vulnerable habitats.

The study presented here makes contribution to both remote sensing research and to saltcedar invasion research. From a pure remote sensing perspective, this dissertation contributes to expand the concepts of accuracy assessment and change detection analysis when a sub-pixel ontology is adopted for analysis. From an invasive species standpoint it provides tested methods that can be readily used for estimating population parameters, which are required for

several management operations and research. Moreover, the findings support a long suspected significant impact in the river flow and confirmed that saltcedar is not actively displacing the native species, but rather taking advantages of hydrologic disturbances. Knowledge and products derived may be useful to support decision-making by several agencies that are undertaking the bio-control of saltcedar (DeLoach *et al.*, 2004; Shafroth *et al.*, 2005) as well as in the restoration of riparian ecosystems endangered by saltcedar invasion (Harris, 1999; Hart *et al.*, 2005; Taylor and McDaniel, 1998).

1.5   About this dissertation

The substantive content of this dissertation is organized as follows. Chapter 2 provides a thorough review of the existing alternatives, while identifying major drawbacks and desirable properties, for sub-pixel accuracy assessment based on cross-comparison matrices, and develops theoretical grounds, for a more general accuracy assessment of soft classifications, that account for the sub-pixel class distribution uncertainty.

Chapter 3 reports results on the assessment of several linear and non-linear spectral mixture models for repeatable mapping of sub-pixel canopy cover of saltcedar and associated native species from Landsat measurements. The research focus is on identifying the advantages and practical implication of incorporating non-linear relationships that result from multiple-scattering processes.

Chapter 4 introduces a post-classification change detection method based on sub-pixel classifications for studying the dynamics of saltcedar along the

segment of the Rio Grande river between the towns of Candelaria, Texas, and Presidio, Texas. The research focuses on testing the role of several environmental factors in driving observed distributions and changes, and estimate the relationship of saltcedar encroachment with reductions of river flow.

Chapter 5 describes a spatially-explicit metapopulation model for linking remote sensing land cover change to population parameters and for hypothesis formulation on the study of general invasion process under competition. This chapter focuses on the theoretical derivation of a land cover change model, referred to as the COEXOD (COlonization-EXtinction-Occlusion-Dominance) model, and its coupling with remote sensing observations for population parameters estimation. While the COEXOD model is derived from a spatially explicit metapopulation model, the latter is also used to determine conditions for invasiveness under competition through simulated populations, where saltcedar invasion under the presence of established mesquite is taken as a case study.

Chapter 6 presents a discussion on conclusions drawn from results reported in prior Chapters.

Chapter 2

CROSS-TABULATION MATRICES FOR SUB-PIXEL CLASSIFICATION ANALYSIS*

2.1 Introduction

The significance of land cover as an environmental variable has made remote sensing one of the most attractive tools for the production of thematic maps of the earth's surface. However, in order for remote sensing to succeed as a valuable source of land cover information, more reliable accuracy measures are needed (Foody, 2002). In the past few decades, the prevailing concerns on ecological and environmental issues, occurring especially at regional to global scales, have prompted significant advances on the use of remote sensing data for the estimation of land cover information at sub-pixel level (Carpenter *et al.*, 1999; Cross *et al.*, 1991; Fisher and Pathirana, 1990; Gutman and Ignatov, 1998; Roberts *et al.*, 1993). However, the quality of such classification products, as well as the performance of the classification protocol employed, are difficult to quantify. Moreover, there is an increasing need for sub-pixel and super-pixel assessment of classification products made evident by recent remote sensing research (Latifovic and Olthof, 2004; Okeke and Karnieli, 2006; Ozdogan and Woodcock, 2006; Shabanov *et al.*, 2005). The assessment of the conventional (hard) allocation of

---

*An extended version of this chapter appeared in the Remote Sensing of Environment Journal (see Silván-Cárdenas and Wang, 2008b, for further details).

16

image pixels to discrete classes has been standardized (to some extent) through the confusion matrix and some derived measures (Congalton, 1991; Congalton and Green, 1999; Stehman and Czaplewski, 1998). However, this method is appropriate only for hard classifications, where it is assumed that each pixel is associated with only one class in both the assessed and the reference datasets. For soft classifications, where multiple classes are assigned to a single pixel, a comparable standardized assessment procedure has not been established yet.

For the evaluation of soft classifications in general, various suggestions have been made (Binaghi *et al.*, 1999; Congalton and Green, 1999; Foody, 1995; Gopal and Woodcock, 1994; Green and Congalton, 2004; Lewis and Brown, 2001; Pontius Jr and Cheuk, 2006; Townsend, 2000), among which, the fuzzy error matrix (Binaghi *et al.*, 1999) is one of the most appealing approaches, as it represents a generalization (grounded on the fuzzy set theory) of the traditional confusion matrix. In spite of its sound theoretical basis, the fuzzy error matrix is not generally adopted as a standard accuracy report and statement for soft classifications. Some reasons for this have been highlighted as counterintuitive characteristics (Pontius Jr and Cheuk, 2006). Specifically, for a cross-comparison to be consistent with the traditional confusion matrix, it is desirable that the cross-comparison results in a diagonal matrix when a map is compared to itself, and that its marginal totals match the total of membership grades. More importantly, a cross-comparison should convey readily interpretable information on the confusion among the classes. A composite operator for computing a cross-comparison matrix that exhibits some of the aforementioned desirable

characteristics was then proposed as a tool for the sub-pixel comparison of maps (Pontius Jr and Cheuk, 2006; Pontius Jr and Connors, 2006). Nevertheless, its utility has not been demonstrated beyond the use of traditional accuracy indices, and neither has the use of the off-diagonal cells been demonstrated, nor is their interpretation clear.

In light of the above, the objectives of this research are:

1. Review the existing alternatives, while identifying major drawbacks and desirable properties, for sub-pixel accuracy assessment based on cross-comparison matrices, and

2. Develop theoretical grounds for a more general cross-comparison of sub-pixel classifications accounting for the sub-pixel class distribution uncertainty.

The remaining of the chapter is organized as follows. In Section 2.2, a theoretical framework for generalized cross-comparison matrices is discussed, and various potential cross-comparison matrices for sub-pixel accuracy assessment are compared within this framework. In Section 2.3, a new cross-comparison matrix that reports the confusion interval in the form of a center value plus-minus maximum error is introduced. The new matrix is referred to as *sub-pixel confusion-uncertainty matrix* (SCM). Sub-pixel accuracy measures are also derived and illustrated in this section.

2.2   Theoretical background

2.2.1   Notation and definitions

The following symbols are used throughout the text:

N - number of pixels in the reference and assessed datasets,

K - number of categories or classes,

n - pixel index, where $n = 1, \ldots, N$,

k, l - class indices, where $k, l = 1, \ldots, K$,

s_{nk} - grade of membership of pixel n to class k assigned by the assessed dataset,

r_{nl} - grade of membership of pixel n to class l assigned by the reference dataset,

s_{+k} - total grade of class k from the assessed dataset, $s_{+k} = \sum_n s_{nk}$,

r_{+l} - total grade of class l from the reference dataset, $r_{+l} = \sum_n r_{nl}$,

s'_{nk} - overestimation error of class k at pixel n, $s'_{nk} = \max(s_{nk} - r_{nk}, 0)$,

r'_{nl} - underestimation error of class l at pixel n, $r'_{nl} = \max(r_{nl} - s_{nl}, 0)$,

p_{nkl} - agreement-disagreement between membership grades from assessed class k and reference class l at pixel n; it is called *agreement* when $k = l$ and *disagreement* (or confusion) when $k \neq l$,

P_{kl} - overall agreement-disagreement between assessed class k and reference class l, $P_{kl} = \sum_n p_{nkl}$,

P_{k+} - marginal row sum of P_{kl} for class k, $P_{k+} = \sum_l P_{kl}$,

P_{+l} - marginal column sum of P_{kl} for class l, $P_{+l} = \sum_k P_{kl}$,

P_{++} - total sum of P_{kl}, $P_{++} = \sum_k \sum_l P_{kl}$,

The grade of membership have various interpretations throughout the text, including possibility, probability and sub-pixel fractions of land-cover. In any case, they are constrained so that $0 \leq r_{nk} \leq 1$, $0 \leq s_{nk} \leq 1$ and $\sum_k r_{nk} = \sum_k s_{nk} = 1$ hold for all the pixels. The agreement-disagreement at pixel n, p_{nkl}, is computed using a comparison operator of the form $C(s_{nk}, r_{nl})$. The notations p_{nkl}^C and P_{kl}^C may be used to specify the comparison operator, C, employed for computing the per-pixel and overall agreement-disagreement, respectively. A confusion matrix is a cross-tabulation (see Table 2.1(a)) formed by the overall agreement-disagreement, P_{kl}, where row and column labels of the matrix represent assessed categories and reference categories, respectively. Thus, the agreement values correspond to the diagonal cells, whereas the disagreement values correspond to the off-diagonal cells.

2.2.2 A generalized cross-comparison framework

Hard classifications are commonly assessed through the so-called confusion matrix (also known as error matrix) and a series of derived indices (Congalton, 1991; Congalton and Green, 1999; Stehman and Czaplewski, 1998). Once generated, the confusion matrix can be used for a series of descriptive and

analytical techniques, such as those based on accuracy indices. Table 2.1(a) shows the general structure of the confusion matrix and Table 2.1(b) lists the most common accuracy indices derived from the confusion matrix. Details on the definitions and uses of these accuracy indices for hard classifications can be found in (Congalton, 1991; Congalton and Green, 1999; Stehman and Czaplewski, 1998), to list just a couple. Naturally, many researchers have tried to generalize the confusion matrix for soft classifications (Binaghi *et al.*, 1999; Latifovic and Olthof, 2004; Lewis and Brown, 2001; Pontius Jr and Cheuk, 2006; Townsend, 2000; Woodcock and Gopal, 2000). While all these efforts have some value for various remote sensing applications, the theoretical background behind each of them does not generally consider a set of desirable characteristics inherited from the confusion matrix, and thus are difficult to interpret (at least in the sense of a traditional confusion matrix).

In the search for the fundamental characteristics of a generalized confusion matrix for soft classifications, it is sometimes suggested that the matrix should fulfill two characteristics:

  i. *Diagonalization*. The matrix should be diagonal if, and only if, the assessed data match perfectly the reference data.

 ii. *Marginal sums*. Marginal sums should match the total grades from the reference and assessed data.

The first characteristic is desirable for the matrix to be useful in identifying a perfect matching case; nevertheless, it does not constrain the matrix characteristic

Table 2.1: Traditional error analysis for crisp classifications. Cross-tabulation (a) and accuracy indices (b). K is the number of classes.

		Reference			
Class	class 1	class 2	...	class K	Row Tot.
class 1	P_{11}	P_{12}	...	P_{1K}	P_{1+}
class 2	P_{21}	P_{22}	...	P_{2K}	P_{2+}
$\vdots$	$\vdots$	$\vdots$	$\ddots$	$\vdots$	$\vdots$
class K	P_{K1}	P_{K2}	...	P_{KK}	P_{K+}
Col. Tot.	P_{+1}	P_{+2}	...	P_{+K}	P_{++}

(a)

Accuracy Index	Formula[a]
Overall accuracy, OA	$\frac{\sum_k P_{kk}}{P_{++}}$
k-th User accuracy, $UA(k)$	$\frac{P_{kk}}{P_{k+}}$
k-th Producer accuracy, $PA(k)$	$\frac{P_{kk}}{P_{+k}}$
Expected proportion of agreement, P_e	$\frac{\sum_k P_{k+}P_{+k}}{P_{++}^2}$
Kappa coefficient of agreement, κ	$\frac{(P_o-P_e)}{(1-P_e)}$

[a] P_o is the observed proportion of agreement $= OA$

(b)

under slight deviation from the perfect match. Therefore, many alternatives could be envisaged that lead to a unique diagonal matrix for the perfect matching case, but to rather different matrices when non-perfect match occurs. The second characteristic is desirable (although it may not be necessary) for the matrix to be useful in deriving accuracy indices such as those listed in Table 2.1(b). For hard classifications, accuracy indices are customarily written in terms of row and column totals, provided that these marginal sums correspond to the class proportions in the assessed and reference datasets, respectively (i.e., $P_{+l} = r_{+l}$, $P_{k+} = s_{+k}$, and $P_{++} = N$). For soft classifications, however, marginal sums not matching the class proportions are often ignored, and class proportions are used instead for the computation of accuracy indices (e.g., Binaghi *et al.*, 1999; Okeke and Karnieli, 2006; Shabanov *et al.*, 2005).

Instead of looking at the properties of a generalized confusion matrix, this research seeks to establish a number of fundamental properties on the agreement-disagreement measures that can lead to meaningful matrix entries. These properties are loosely described below and then formalized in mathematical terms. First, a meaningful agreement measure does not consider whether the assessed pixel membership is above or below the reference pixel membership, i.e., does not depend on the over- or underestimation errors. In contrast, the sense and amount of discrepancy are important for defining a disagreement measure. An overestimation of the reference pixel membership by the assessed pixel membership leads to errors of commission type. These commission errors appear in the off-diagonal cells along the row of the class. Conversely, an underestimation of the

reference value by the assessed value leads to errors of omission type. These omission errors appear in the off-diagonal cells along the column of the class. Second, agreement and disagreement are, in some sense, complimentary yet non-negative measures. This is also stated by the constrained marginal sums characteristic. Consequently, when the agreement for a given class achieve its maximum (e.g., in the case of a perfect match), the overall disagreement (sum of off-diagonal cells) for that class must be minimum (zero). Conversely, if the overall disagreement is maximum, then the agreement is minimum.

In formal grounds, one requires the agreement-disagreement measure to conform to Equation (2.1), where A and D denote agreement and disagreement operators, respectively, which satisfy the properties outlined in Table 2.2, and s'_{nk} and r'_{nl} denote the over- and underestimation errors at pixel n. Notice that the expressions given in Equations (2.2) and (2.3) for the over- and underestimation errors, respectively, are mathematically equivalent to those given in Section 2.2.1.

$$C(s_{nk}, r_{nl}) = \begin{cases} A(s_{nk}, r_{nl}) & \text{if } k = l \\ D(s'_{nk}, r'_{nl}) & \text{if } k \neq l \end{cases} \tag{2.1}$$

$$s'_{nk} = s_{nk} - \min(s_{nk}, r_{nk}) \tag{2.2}$$

$$r'_{nl} = r_{nl} - \min(s_{nl}, r_{nl}) \tag{2.3}$$

The *Commutativity* property expresses a symmetric characteristic of agreement-disagreement measures respect to its arguments. It ensures that under- and overestimation of a membership grade are equally considered. The *Positivity* ensures closure over the positive space of membership values and, together with the *Nullity* property, constrains non-null comparison values to pixels with non-null

Table 2.2: Basic properties for general agreement and disagreement measures. $C(s,r)$ denotes a comparison (agreement or disagreement) measure between grades s and r, and a is a positive number.

Property	Definition	Agreement	Disagreement
i. Commutativity	$C(s,r) = C(r,s)$	Yes	Yes
ii. Positivity	$s > 0 \wedge r > 0 \Rightarrow C(s,r) > 0$	Yes	Yes
iii. Nullity	$s = 0 \vee r = 0 \Rightarrow C(s,r) = 0$	Yes	Yes
iv. Upper bound	$C(s,r) \leq C(r,r)$	Yes	No
v. Homogeneity	$C(as,ar) = aC(s,r)$	Yes	Yes

membership values. The *Upper bound* property implies that the comparison operator measures essentially the degree of similarity, as contrasted to dissimilarity or distance measures, between two membership values. The *Homogeneity* property states that the agreement-disagreement values can be denormalized in proportion to denormalized grade values. This property is desirable when the accuracy assessment is inserted in a multi-resolution framework (see Pontius Jr, 2002; Pontius Jr and Cheuk, 2006; Silván-Cárdenas and Wang, 2008b, for further details). In sum, two notable differences between agreement and disagreement measures are established: 1) an agreement value depends on the original assessed and reference values, whereas a disagreement value depends on the over- and under estimation errors, and 2) an agreement value has an upper bound at perfect match, whereas disagreement values do not share an upper bound at null agreement.

2.2.3 Operators for assessing sub-pixel classifications

2.2.3.1 The sub-pixel ontology

According to Pontius Jr and Cheuk (2006), each cross-comparison operator is rooted on a specific ontology of the pixel. More specifically, a cross-comparison

depends on how the pixel-class relationship is defined and quantified. Two major definitions for the pixel-class relationship that admit multiple memberships have been broadly used in the land-cover classification research. The first definition conceives this relationship as uncertain and formalizes it through the probability theory. The second definition conceives this relationship as vague or ambiguous and formalizes it through the fuzzy set theory. In both cases, the hard classification is covered as a special case, that is when no uncertainty nor ambiguity exists. A third pixel-class relationship, that has received less attention (at least from the accuracy assessment point of view, with exception of Latifovic and Olthof, 2004), relates pixel to class through a fractional land cover. This pixel-class relationship definition implies the existence of unknown crisp boundaries among the classes at sub-pixel level. It should be noted that the kind of uncertainty a sub-pixel classification represents can be related only to the positional accuracy resolved by the sensor (pixel resolution). Soft classifications emphasizing the thematic uncertainty, which are linked to the impossibility of uniquely identifying a land cover category regardless of the sensor resolution, are not being considered here. If the uncertainty represented by a soft classification describes vague concepts, which are characteristic of the human reasoning, then other alternatives may be pursued (see for instance Gopal and Woodcock, 1994).

For the sub-pixel ontology the following definitions are considered here:

1. The pixel-class relationship is defined through the sub-pixel fraction of class coverage, and

Table 2.3: Four basic operators.

Operator ID	Operator of the form[a] $C(s_{nk}, r_{nl})$	Traditional interpretation	Sub-pixel interpretation
MIN	$\min(s_{nk}, r_{nl})$	fuzzy set intersect.	maximum overlap
SI	$1 - \frac{\|s_{nk} - r_{nl}\|}{s_{nk} + r_{nl}}$	similarity index	normalize max.
PROD	$s_{nk} \times r_{nl}$	joint probability	expected overlap
LEAST	$\max(s_{nk} + r_{nl} - 1, 0)$	minimum overlap	minimum overlap

[a] s_{nk} and r_{nk} denote assessed and reference grades of class k at pixel n

2. The agreement-disagreement is quantified as the proportion of area overlap among the classes at sub-pixel level.

2.2.3.2 Basic operators

Various operators have been developed under rather distinct pixel ontology, some of which are listed in Table 2.3. Some have been considered previously within a multi-resolution framework (Kuzera and Pontius Jr, 2004; Pontius Jr and Cheuk, 2006), and their sub-pixel interpretation has been also discussed (Pontius Jr and Connors, 2006). However, the major focus has been so far on the accuracy indices at multiple resolutions. The present review investigates their suitability for assessing sub-pixel classifications within the context of the generalized cross-comparison framework introduced above.

The *minimum* operator (MIN) is the classic fuzzy set *intersection* operator. This operator has been suggested as the natural choice for producing cross-comparison matrices for fuzzy classifications (Binaghi *et al.*, 1999). In the traditional ontology of fuzzy classifications, the pixel-class relationship describes the admission of the possibility (given by a so-called membership function) that

the pixel is a member of a class. This pixel-class relationship definition is useful for handling the imprecision of meaning of concepts that are characteristic of much of the human reasoning (Gopal and Woodcock, 1994). Unfortunately, the area estimation by map users is generally difficult under this ontology (Woodcock and Gopal, 2000). In the sub-pixel fraction ontology, the MIN operator measures the maximum sub-pixel overlap among the classes. Therefore, if membership values are (linearly) related to sub-pixel land cover areas (see e.g., Shabanov *et al.*, 2005), the fuzzy set intersection operator corresponds to the maximum sub-pixel overlap between the classes. The minimum operator satisfies all the properties outlined in Table 2.2. However, the MIN matrix can overestimate the actual sub-pixel agreement-disagreement and, consequently, the marginal sums can be greater than the sub-pixel fractions. Also, even in the case of a perfect match, non-null degrees of mismatch are obtained for the off-diagonal cells. These characteristics generally limit the matrix's utility for drawing a conclusion about the confusion among the classes.

A variant of the MIN operator is sometimes used as a *similarity index* (SI) for comparing soft classifications (see e.g., Townsend, 2000). This variant results after normalizing the MIN operator by the sum of the grade values, and can be expressed as shown in Table 2.3. The SI operator is also meaningful for sub-pixel comparison, as it corresponds to a normalized maximum sub-pixel overlap. Nevertheless, it does not satisfy the homogeneity property, as it is invariant under scaling of the grade values. A cross-comparison matrix based on the SI operator does not satisfy the diagonalization and marginal sums characteristics outlined

above.

The *product* operator (PROD) arises from a pure probabilistic view of the pixel-class relationship. In the traditional probabilistic ontology, the pixel-class relationship represents the probability that a pixel (entirely) belongs to a class, and the PROD operator gives the *joint probability* that the reference and assessed pixels belong to two given classes, provided that the pixels have been independently classified. In the sub-pixel fraction ontology, the PROD operator measures the expected class overlap by chance between the reference and assessed sub-pixels partitions. More specifically, consider a randomly drawn point from the space spanned by pixel n. Since all the points within the pixel have the same probability to come out, then the joint probability that the point belongs to class k in the assessed partition and to class l in the reference partition is given by the product $s_{nk} \times r_{nl}$, provided that the land-cover fractions s_{nk} and r_{nl} have been generated by independent processes. A cross-comparison matrix based on the PROD operator has marginal sums that agree with the per-class areas. However, non-null disagreement values can result from the perfect matching case. In fact, it does not satisfy the upper-bound and homogeneity properties of Table 2.2. The latter, however, could be fulfilled if the operator is properly normalized (see the MIN-PROD composite operator below). The use of this operator for the assessment of soft classifications has been demonstrated in (Lewis and Brown, 2001), and its counterintuitive characteristics have been illustrated in (Pontius Jr and Cheuk, 2006).

The LEAST operator was recently introduced in the discussion of sub-pixel

comparison of maps (Pontius Jr and Connors, 2006). The expression for the LEAST operator is given in Table 2.3. This operator measures the *minimum possible sub-pixel overlap* between two classes. Even though this operator is meaningful for sub-pixel accuracy assessment, it may be of little use for other contexts, as it has even more counterintuitive characteristics than the PROD operator. Specifically, this operator fails to fulfill all but the commutativity and nullity properties from Table 2.2. As with the PROD operator, the homogeneity property could be met by a modified LEAST operator that relaxes the sum-to-unit constraint (see the MIN-LEAST composite operator below).

2.2.3.3   Composite operators

None of the basic operators above satisfy the diagonalization characteristic discussed in Section 2.2.2. Indeed, in order for an operator to exhibit the diagonalization characteristic, it must conform to Equation (2.1). This type of operator is referred to as *composite*. The formalism in Table 2.2 is then useful for guiding the selection of potential composite operators for general soft classifications. For example, the only operator from Table 2.3 that satisfies all the basic properties in Table 2.2 for an agreement measure is the MIN operator. The uniqueness of the MIN operator as an agreement measure is also evidenced in Equations (2.2) and (2.3), where over- and underestimation errors are given in terms of the MIN operator. Here, I consider only three composite operators that use the MIN operator as agreement measure. They are referred to as MIN-PROD, MIN-MIN and MIN-LEAST, respectively. These are defined in Table 2.4.

Table 2.4: Three composite operators.

Operator ID	Agreement[a]	Disagreement[b] $(k \neq l)$	Sub-pixel confusion
MIN-PROD	$\min(s_{nk}, r_{nk})$	$s'_{nk} \times r'_{nl} / \sum_i r'_{ni}$	constr. expected
MIN-MIN	$\min(s_{nk}, r_{nk})$	$\min(s'_{nk}, r'_{nl})$	constr. maximum
MIN-LEAST	$\min(s_{nk}, r_{nk})$	$\max(s'_{nk} + r'_{nl} - \sum_i r'_{ni}, 0)$	constr. minimum

[a] s_{nk} and r_{nk} denote the assessed and reference grades for class k at pixel n

[b] s'_{ni} and r'_{ni} denote the over- and underestimation errors of class i at pixel n

The MIN-PROD composite operator was recently proposed by Pontius Jr and Cheuk (2006). It uses the minimum operator for the diagonal cells and a normalized product operator for the off-diagonal cells, thus combining the fuzzy set view with the probabilistic view. Expressions for the agreement and disagreement from this composite operator are presented in Table 2.4. This operator satisfies the basic properties of Table 2.2. In addition, the MIN-PROD matrix satisfies the diagonalization and marginal sums characteristics. The interpretation of the composite operator in the context of sub-pixel agreement-disagreement is aligned with an assumption of maximum overlap between corresponding categories (diagonal cells), followed by the allocation of the residual sub-pixel fractions onto the other categories (off-diagonal cells). The disagreement measure corresponds to the expected overlap by chance constrained to the unmatched sub-pixel fraction. Specifically, the disagreement between two membership values, s_{nk} and r_{nl}, corresponds to the joint probability that a randomly drawn point within the space spanned by the unmatched fraction, $1 - \sum_i \min(s_{ni}, r_{ni})$, of pixel n, belongs to classes k and l in the residual class fractions $s_{nk} - \min(s_{nk}, r_{nk})$ and $r_{nl} - \min(s_{nl}, r_{nl})$ of the assessed and reference pixels, respectively.

The MIN-MIN composite operator uses the minimum operator for both

agreement and disagreement. However, it differs from the MIN operator in that it assigns agreement in a first step and then, in a second step, it computes the disagreement based on the over- and underestimation errors. Table 2.4 shows the expressions for agreement and disagreement from this composite operator. The MIN-MIN composite operator satisfies all the properties outlined in Table 2.2. In addition, it leads to a cross-comparison matrix that satisfies the diagonalization property. However, it does not warrant the marginal sum characteristic. Marginal totals of a MIN-MIN matrix will, generally, overestimate the class proportions from the reference and assessed datasets because the MIN operator, used for computing the off-diagonals cells, accounts for the maximum possible overlapping area among the residual fractions at sub-pixel level. In this sense, the disagreement measure from the MIN-MIN operator provides an upper bound for the possible sub-pixel overlap constrained to the unmatched sub-pixel fraction.

The MIN-LEAST composite operator uses the MIN operator for the diagonal cells and a re-normalized LEAST operator for the off-diagonal cells. Table 2.4 shows the expressions for agreement and disagreement from this composite operator. While the agreement measure satisfies all the properties of Table 2.2, the disagreement measure does not satisfy the required positivity property: Non-null over- and underestimation errors can lead to null disagreement values. The MIN-LEAST operator produces a diagonal matrix for a perfect matching case. However, sub-pixel areas from the reference and assessed datasets are generally underestimated by marginal totals. This is because the disagreement measure corresponds to the minimum possible sub-pixel overlap constrained to the

unmatched sub-pixel fraction. Specifically, the re-normalized LEAST operator determines the excess of the sum of two residual class fractions, $s_{nk} - \min(s_{nk}, r_{nk})$ and $r_{nl} - \min(s_{nl}, r_{nl})$, respect to the unmatched pixel fraction, $1 - \sum_i \min(s_{ni}, r_{ni})$.

2.3 The sub-pixel confusion-uncertainty matrix

2.3.1 Sub-pixel confusion intervals

The preceding review of potential cross-comparison matrices for assessing sub-pixel classifications has shown that: 1) a composite operator is necessary to warrant the diagonalization characteristic, and 2) the MIN operator is the most appropriate candidate for agreement measure. It is worth noting that the use of a MIN operator for allocating sub-pixel proportions along the diagonal cells accounts only for the agreement at pixel level, i.e., the possible spatial distribution of classes within the pixel is not taken into account, but only the sub-pixel area proportions are matched. In contrast, the sub-pixel disagreement can take into account the possible spatial distribution of classes within the pixel. Nevertheless, there is no unique way to exactly allocate the remaining sub-pixel proportion into the off-diagonal cells. Specifically, the sub-pixel area allocation problem remains underspecified, as there are more unknowns ($K^2 - K$ off-diagonals elements) than equations ($2K$ constraints from column and row totals). Some exceptions occur, for example, if $K = 2$ or $K = 3$. One possibility is to use the statistical center of possible confusions, as given by the MIN-PROD composite operator. However, the sub-pixel distribution uncertainty could not be accounted in this way. An

alternate solution is proposed here that uses the *confusion intervals*,

$[P_{kl}^{\text{MIN-LEAST}}, P_{kl}^{\text{MIN-MIN}}]$, formed by the MIN-LEAST and MIN-MIN operators.

These intervals express the possible confusions among the classes. As

demonstrated below, if there is a unique solution to the area allocation problem,

then these intervals are tight (i.e., the lower and upper bounds of each confusion

interval have the same value). In this case, the three composite operators of

Table 2.4 lead essentially to the same confusion matrix.

2.3.1.1 A simple example

In order to illustrate the use of the confusion intervals, consider a reference

pixel belonging to classes 1, 2, 3, and 4 with membership values $r_1 = 0.4$, $r_2 = 0.3$,

$r_3 = 0.2$ and $r_4 = 0.1$, respectively. Consider also the following three cases of

assessed pixels:

(a) *Perfect matching*: $s_1 = 0.4$, $s_2 = 0.3$, $s_3 = 0.2$, $s_4 = 0.1$

(b) *Non-perfect matching 1*: $s_1 = 0.3$, $s_2 = 0.2$, $s_3 = 0.4$, $s_4 = 0.1$

(c) *Non-perfect matching 2*: $s_1 = 0.3$, $s_2 = 0.1$, $s_3 = 0.4$, $s_4 = 0.2$

The fundamental difference between the cases (b) and (c) is in the number of

overestimated classes (one and two overestimated classes, respectively). The

sub-pixel confusion intervals for cases (a)-(c) are shown in Tables 2.5(a)-(c),

respectively. Notice that the sub-pixel area allocation problem is uniquely

determined for cases (a) and (b), as the maximum and minimum confusions are

the same. However, it cannot be uniquely resolved for case (c), where the

minimum and maximum confusions of class 1 and class 2 with class 3 are not the same. What this matrix says is, for instance, that class 2 is confounded with class 3 in at least 0.1 ([0.1,0.2]), whereas class 1 might not be confounded at all with class 3 ([0,0.1]). Table 2.6 shows the MIN-PROD matrix for case (c). As pointed out before, the confusion values provided by the MIN-PROD operator must be considered as the expected confusion by chance, i.e., it represents a statistical center for all possible confusions; whereas the confusion interval defines the uncertainty associated to the sub-pixel confusion.

Since a confusion interval involves the notion of uncertainty on the confusion, it is natural to inquire under which circumstances the confusion intervals would be tight for an arbitrary number of classes. In Appendix I it is shown that if no more than one class is either over- or underestimated at each single pixel, then the sub-pixel area allocation problem can be uniquely resolved. Not surprisingly, this unique-solution scenario includes any of the following cases: 1) there is a perfect match, 2) there are no more than three classes, 3) at least one of the datasets is crisp.

2.3.2   Sub-pixel confusion-uncertainty matrix

In practice, it is convenient to express each confusion interval in the form $P_{kl} \pm U_{kl}$, where P_{kl} and U_{kl} are the interval center and the interval half-width, respectively. These are computed as indicated by Equations (2.4) and (2.5), respectively.

$$P_{kl} = \frac{P_{kl}^{\text{MIN-MIN}} + P_{kl}^{\text{MIN-LEAST}}}{2} \qquad (2.4)$$

Table 2.5: Sub-pixel confusion interval matrices for three cases: Perfect matching (a), underestimation with unique solution (b), and underestimation without unique solution (c). CPR and CPA are class proportion from reference and assessed pixels, respectively.

	Reference				
Class	1	2	3	4	CPA
1	[0.4,0.4]	[0,0]	[0,0]	[0,0]	0.4
2	[0,0]	[0.3,0.3]	[0,0]	[0,0]	0.3
3	[0,0]	[0,0]	[0.2,0.2]	[0,0]	0.2
4	[0,0]	[0,0]	[0,0]	[0.1,0.1]	0.1
CPR	0.4	0.3	0.2	0.1	1.0

(a)

	Reference				
Class	1	2	3	4	CPA
1	[0.3,0.3]	[0,0]	[0,0]	[0,0]	0.3
2	[0,0]	[0.2,0.2]	[0,0]	[0,0]	0.2
3	[0.1,0.1]	[0.1,0.1]	[0.2,0.2]	[0,0]	0.4
4	[0,0]	[0,0]	[0,0]	[0.1,0.1]	0.1
CPR	0.4	0.3	0.2	0.1	1.0

(b)

	Reference				
Class	1	2	3	4	CPA
1	[0.3,0.3]	[0,0]	[0,0]	[0,0]	0.3
2	[0,0]	[0.1,0.1]	[0,0]	[0,0]	0.1
3	[0,0.1]	[0.1,0.2]	[0.2,0.2]	[0,0]	0.4
4	[0,0.1]	[0,0.1]	[0,0]	[0.1,0.1]	0.2
CPR	0.4	0.3	0.2	0.1	1.0

(c)

Table 2.6: MIN-PROD matrix for case (c) of Table 2.5. Values are rounded to two decimals.

	Reference				
Class	1	2	3	4	Row Tot.
1	0.30	0.00	0.00	0.00	0.30
2	0.00	0.10	0.00	0.00	0.10
3	0.07	0.13	0.20	0.00	0.40
4	0.03	0.07	0.00	0.10	0.20
Col. Tot.	0.40	0.3	0.2	0.10	1.00

$$U_{kl} = \frac{P_{kl}^{\text{MIN-MIN}} - P_{kl}^{\text{MIN-LEAST}}}{2} \qquad (2.5)$$

This notation is preferred, as it provides a *center value* and allows documenting explicitly its associated *uncertainty*[1], which in turn is necessary for further error propagation analysis. By extension to our definitions, row marginal sum, column marginal sum, and total sum from uncertainty values are defined as $U_{k+} = \sum_l U_{kl}$, $U_{+l} = \sum_k U_{kl}$, $U_{++} = \sum_k \sum_l U_{kl}$, respectively.

Equation (2.4) defines an operator that satisfies all the basic properties in Table 2.2. This operator leads to a matrix that exhibits the diagonalization characteristic. However, it does not warrant the marginal sum characteristic. A typical way to circumvent this inconvenience has been the use of area proportions from the reference and assessed datasets in place marginal totals (Binaghi *et al.*, 1999). Examples of this kind of cross-tabulations are shown in Tables 2.5(a)-(c) and, more formally, in Table 2.7. In this way, the accuracy indices of Table 2.1(b) are readily generalized, where row and column totals are simply replaced by the

---

[1]The half-width of the confusion interval is termed the uncertainty, as it reflects the uncertain nature of the sub-pixel distribution of classes.

Table 2.7: Sub-pixel confusion-uncertainty matrix, where marginal totals have been replaced by the class proportions from the reference (CPR) and assessed (CPA) datasets.

	Reference				
Class	class 1	class 2	...	class K	CPA
class 1	P_{11}	$P_{12} \pm U_{12}$	...	$P_{1K} \pm U_{1K}$	s_{+1}
class 2	$P_{21} \pm U_{21}$	P_{22}	...	$P_{2K} \pm U_{2K}$	s_{+2}
$\vdots$	$\vdots$	$\vdots$	$\ddots$	$\vdots$	$\vdots$
class K	$P_{K1} \pm U_{K1}$	$P_{K2} \pm U_{K2}$	...	P_{KK}	s_{+K}
CPR	r_{+1}	r_{+2}	...	r_{+K}	N

corresponding area proportions. Unfortunately, the accuracy indices so-derived cannot reflect the uncertainty of the confusion as they do not depend on the off-diagonal cells. Notice that diagonal cells in Table 2.7 does not provide U-values. Since the U-values reflect the sub-pixel distribution uncertainty, which is not considered for the agreement, these are zeros for the diagonal cells.

Another possibility, which is pursued here, is to consider column and row totals as intervals (Table 2.8(a)). These intervals can be used to derive intervals of accuracy indices that reflect the uncertain nature of the sub-pixel distribution of classes. Table 2.8(a) shows the general structure of the proposed sub-pixel confusion-uncertainty matrix (SCM).

2.3.3 Derived accuracy-uncertainty indices

Table 2.8(b) shows the expressions of derived accuracy-uncertainty indices based exclusively on values from Table 2.8(a). These expressions represent generalizations from traditional single-valued accuracy indices to intervals, which are expressed in the form of a center value plus-minus maximum deviation (or

Table 2.8: General structure of the SCM (a) and derived sub-pixel accuracy-uncertainty indices (b). Row and column totals of the SCM are determined as sum of center values (P_{kl}) plus-minus sum of uncertainty values (U_{kl}). The observed proportion of agreement ($P_o \pm U_o$) corresponds to the overall accuracy (OA_s), whereas the expected proportion of agreement ($P_e \pm U_e$) is given by Equations (2.6-2.7).

	Reference				
Class	class 1	class 2	...	class K	Row Tot.
class 1	P_{11}	$P_{12} \pm U_{12}$	...	$P_{1K} \pm U_{1K}$	$P_{1+} \pm U_{1+}$
class 2	$P_{21} \pm U_{21}$	P_{22}	...	$P_{2K} \pm U_{2K}$	$P_{2+} \pm U_{2+}$
⋮	⋮	⋮	⋱	⋮	⋮
class K	$P_{K1} \pm U_{K1}$	$P_{K2} \pm U_{K2}$	...	P_{KK}	$P_{K+} \pm U_{K+}$
Col. Tot.	$P_{+1} \pm U_{+1}$	$P_{+2} \pm U_{+2}$	...	$P_{+K} \pm U_{+K}$	$P_{++} \pm U_{++}$

(a)

Sub-pixel Accuracy Index	Center	Uncertainty
Overall accuracy, OA_s	$\dfrac{P_{++}\sum_k P_{kk}}{P_{++}^2 - U_{++}^2}$	$\dfrac{U_{++}\sum_k P_{kk}}{P_{++}^2 - U_{++}^2}$
k-th User Accuracy, $UA_s(k)$	$\dfrac{P_{kk}P_{k+}}{P_{k+}^2 - U_{k+}^2}$	$\dfrac{P_{kk}U_{k+}}{P_{k+}^2 - U_{k+}^2}$
k-th Producer Accuracy, $PA_s(k)$	$\dfrac{P_{kk}P_{+k}}{P_{+k}^2 - U_{+k}^2}$	$\dfrac{P_{kk}U_{+k}}{P_{+k}^2 - U_{+k}^2}$
Kappa coefficient, κ_s	$\dfrac{(P_o-P_e)(1-P_e)-(*U_o+U_e)U_e}{(1-P_e)^2 - U_e^2}$	$\dfrac{*(1-P_o)U e+(1-P_e)U_o}{(1-P_e)^2 - U_e^2}$

$* = $ sign of $(1 - P_o - U_o)(1 - P_e - U_e)$

(b)

uncertainty). For instance, the definition of the kappa coefficient interval (κ_s) is based on the definition of the traditional kappa coefficient of agreement (Cohen, 1960, see Table 2.1(b)), where the overall accuracy interval (OA_s) was considered as the observed proportion of agreement; this is specified in the form $P_o \pm U_o$. Likewise, the expected proportion of agrement was determined in terms of marginal totals and overall total from the SCM and specified in the form $P_e \pm U_e$. The explicit expressions for the expected proportion's center value and uncertainty are given in Equations (2.6) and (2.7), respectively. The uncertainties from both the observed and expected proportions of agreement are propagated onto the kappa coefficient, which results in an interval of kappa coefficients specified through a center value and its associated uncertainty, as given in Table 2.8(b).

$$P_e = \sum_k \frac{(P_{++}^2 + U_{++}^2)(P_{+k}P_{k+} + U_{+k}U_{k+}) - 2P_{++}U_{++}(U_{+k}P_{k+} + P_{+k}U_{k+})}{(P_{++}^2 - U_{++}^2)^2}$$

(2.6)

$$U_e = \sum_k \frac{2P_{++}U_{++}(P_{+k}P_{k+} + U_{+k}U_{k+}) - (P_{++}^2 + U_{++}^2)(U_{+k}P_{k+} + P_{+k}U_{k+})}{(P_{++}^2 - U_{++}^2)^2}$$

(2.7)

The new accuracy-uncertainty indices must be interpreted as approximations to the traditional ones. Such approximations are in the order of the associated uncertainties. As a matter of fact, in the absence of uncertainty, the expressions for their center values are similar to those of Table 2.1(b). Interestingly, in the limit when uncertainty tends to zero, the overall accuracy (OA_s) can be interpreted as a complimented distance between membership values,

as stated by Equation (2.8).[2]

$$OA_s = 1 - \frac{1}{2N} \sum_k \sum_n |r_{nk} - s_{nk}| \qquad (2.8)$$

2.3.3.1 A simple example

The following example illustrates the utility of the accuracy-uncertainty indices. As before, consider a reference pixel belonging to classes 1, 2, 3, and 4 with membership values $r_1 = 0.4$, $r_2 = 0.3$, $r_3 = 0.2$ and $r_4 = 0.1$, respectively. Let us now compare the accuracy of the following two classified pixels:

(a) *No uncertainty*: $s_1 = 0.2$, $s_2 = 0.3$, $s_3 = 0.4$, $s_4 = 0.1$

(b) *Uncertainty*: $s_1 = 0.3$, $s_2 = 0.4$, $s_3 = 0.1$, $s_4 = 0.2$

Notice that the maximum classification error committed in case (b) is lower than in case (a). Therefore, one should expect higher accuracy for case (b) than for case (a). Furthermore, in case (a) the errors are concentrated in two classes (class 1 and class 3), whereas in case (b) the errors are evenly distributed among the four classes. Since the source of errors can be attributed to a larger number of sub-pixel confusions, one should expect the error uncertainty (and thus the accuracy uncertainty) to be higher for case (b) than for case (a). However, these observations could not be revealed through the traditional indices. Specifically, if the assessment is based on the MIN-PROD operator[3], an overall accuracy of 80%

---

[2]This expression can be derived by applying the identity $\min(a, b) = (a + b - |a - b|)/2$.

[3]The same result is obtained if the assessment is based on Table 2.7.

is obtained for both case (a) and case (b). Indeed, the kappa values obtained for case (a) (0.7297) and case (b) (0.7222) are even counter-intuitive. In contrast, if the SCM is applied, an overall sub-pixel accuracy of $80\% \pm 0\%$ ($\kappa_s = 0.7297 \pm 0$) results for case (a) and $83.33\% \pm 16.67\%$ ($\kappa_s = 0.7778 \pm 0.2222$) for case (b), thus agreeing with the reasoning above. In sum, the accuracy-uncertainty indices from the SCM are able to differentiate between sub-pixel classifications having distinct error distributions, even in the case they have the same overall accuracy. Evidently, the larger the uncertainty of an index is, the less useful the center value will be.

2.4   Conclusions

This research has shown that when membership values correspond to land cover fractions and the agreement and disagreement are defined in terms of the amount of sub-pixel overlap among the reference and assessed pixels there may not be a confusion matrix that can uniquely quantify the interclass confusion and the underlaying sub-pixel accuracy. For a cross-comparison report to be useful for identifying a perfect match between the reference and assessed data, it is necessary to constrain the agreement measure at the pixel level. Even though, there is no analytical way to determine uniquely the actual confusion based solely on the information of land cover fractions. This problem was termed the sub-pixel area allocation problem.

A previously proposed operator, termed the MIN-PROD composite operator (Pontius Jr and Cheuk, 2006), seemed meaningful for assessing sub-pixel classifications. However, it was shown how this operator provides one of a

(possibly) infinite number of solutions to the sub-pixel area allocation problem. That solution corresponds to the expected sub-pixel class overlap constrained to the unmatched sub-pixel fraction. Two new composite operators (MIN-LEAST and MIN-MIN) were introduced to provide the minimum and maximum possible sub-pixel class overlap constrained to the unmatched sub-pixel fraction. The intervals defined by these operators are arranged within a matrix, in the form of a center value plus-minus its uncertainty, termed the sub-pixel confusion-uncertainty matrix (SCM). It was shown that all the confusion intervals are tight (i.e., no confusion uncertainty exists) when at most one class is either under- or overestimated at each pixel. Only in these circumstances, the SCM results in the MIN-PROD composite operator-based cross-comparison matrix. This is certainly the case when at least one of the compared sets is crisp, or when the number of classes is less than four. Therefore, uncertainty-free matrices can result often provided that there are many remote sensing methods for producing soft classifications, based on spectral mixing models, in which only three classes may suffice for describing a wide variety of land cover characteristics (Carpenter *et al.*, 1999; Milton, 1999; Roberts *et al.*, 1993; Small, 2004). This result is also convenient for the common practice of assessing continental and global products through moderated resolution images. In this case, crisp classification from coarse resolution images are assessed using fractions derived from moderate resolution images (Latifovic and Olthof, 2004). It is also relevant for applications where reference data cannot be acquired, as in the case of historical data. In such cases, the hardened version of a fuzzy classification can be assessed using the fuzzy values

(Okeke and Karnieli, 2006). Indeed, the SCM results in the traditional confusion matrix if both datasets are crisp.

Chapter 3

RETRIEVAL OF SALTCEDAR SUB-PIXEL CANOPY COVERAGE FROM LANDSAT*

3.1 Introduction

Saltcedar is among the three most frequently occurring woody riparian plants in the Western United States (Friedman *et al.*, 2005) and its control has significant economic implications (US Department of Interior, 2005; Zavaleta, 2000). It has brought several critical problems to invaded ecosystems, among which depletion of stream/river flow is the most worrying (Di Tomaso, 1998; Smith *et al.*, 1998). A repeatable approach for accurate mapping of saltcedar over large spatial extents, yet with the ability to detect low density stands, is urgently needed for both assessing invasion severity and measuring its rate of spread, as well as for assisting in the implementation of, and monitoring the impacts from, effective control programs (Carruthers *et al.*, 2006; DeLoach *et al.*, 2004).

Prior studies have shown the relationship between remotely-sensed spectral response and nonnative saltcedar habitat (Carruthers *et al.*, 2006; Everitt, 1996; Everitt and DeLoach, 1990; Everitt *et al.*, 1992; Hamada *et al.*, 2007). By using high-spatial resolution data, and hyperspatial resolution in some cases, coupled with traditional hard pixel-level classification, these approaches can achieve high

detection accuracies, but are impractical for large-scale monitoring. The application of moderate resolution satellite images could be advantageous in this respect. For example, NASA's MODerate resolution Imaging Spectroradiometer (MODIS) has been successfully used to map saltcedar habitat suitability at country level (Morisette *et al.*, 2006). Nevertheless, the width of saltcedar bands along the river typically varies from a few meters to hundreds of meters making it difficult for this type of sensors to accurately detect saltcedar. Furthermore, it is crucial for an effective management to have the ability to detect saltcedar in the early stages of an invasion episode when its spatial extent is small (Shafroth *et al.*, 2005). Therefore, it is hypothesized that Landsat-like measurements represents the best compromise between spatial resolution and spatial extent.

Recent advancements in sub-pixel mapping from remote sensors have improved over traditional hard classification techniques by allowing quantifying sub-pixel fraction of species coverage. The rationale of this approach is that mixed pixels from remote sensing result from a systematic combination of component spectra (end-members) present in the sensor's instantaneous field of view (IFOV) (Adams *et al.*, 1993; Gillespie, 1992; Milton, 1999). The relative contribution of component spectra is then determined by the inversion of mixture models (Chang and Heinz, 2000; Heinz and Chang, 2001; Hu *et al.*, 1999; Keshava and Mustard, 2002). While horizontal mixing of vegetation types across the landscape due to an increase in the IFOV respect to plant canopy is primarily a linear process (Roberts *et al.*, 1993), the interaction of light with vegetation components in the three-dimensional space is known to be highly nonlinear (Borel and Gerstl, 1994;

Smolander and Stenberg, 2005). Although the general consensus is that linear spectral unmixing (LSU) methods represent the simplest way to estimate the relative cover of plant canopies and bare soil patches with reasonable accuracy (Adams *et al.*, 1995), the question of whether linear or non-linear processes such as multiple-scattering from vegetated land surfaces (Borel and Gerstl, 1994; Smolander and Stenberg, 2005) can dominate the spectral signatures of mixed pixels over scrubland-type ecosystems is still an unresolved matter. The objective of this study was to assess linear and non-linear mixture models for repeatable mapping of sub-pixel canopy cover of saltcedar and associated native species, and at the same time, identify the advantages and practical implication of incorporating non-linear relationships for sub-pixel retrieval of saltcedar canopy cover from Landsat data.

3.2 Data Used

3.2.1 Study site and field measurements

A test bed site was selected on the Forgotten River reach of the Rio Grande River near the town of Candelaria, Texas (Figure 3.1). The vegetation on both banks of the river is composed mostly of saltcedar (*Tamarix chinensis* L.) with some mixes of willow (*Salix* spp). The spatial distribution of saltcedar along the river is typically variable, due in part to changes in the local hydrologic system. As one moves into the uplands, the honey mesquite (*Prosopis* spp.) is found, although it is generally mixed with other bushes, weeds and saltcedar itself. A giant saltcedar species (*Tamarix aphylla* L. Karst or athel tamarisk) can be also
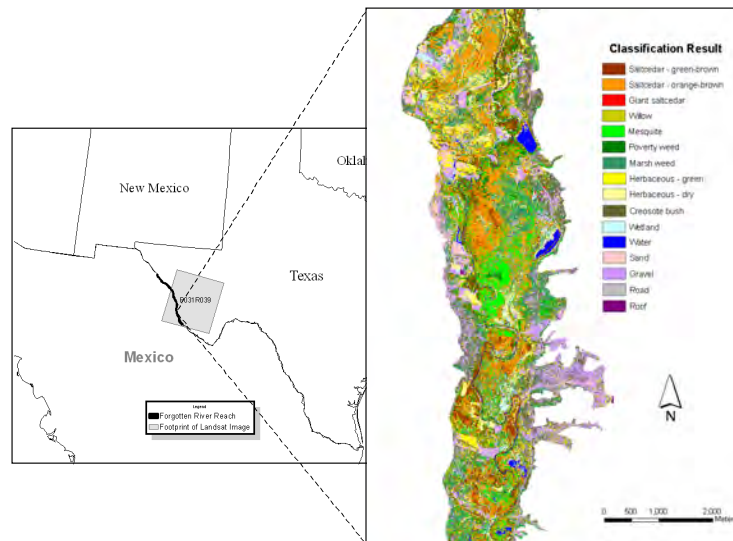
Figure 3.1: Geographic location of the study site (left) and species-level classification map at 1-meter resolution (right).

found in this study site, although in very sparse occurrences along the uplands. The giant saltcedar is an evergreen tree of up to 12 meters in height when mature. It is widely cultivated in the Southwest and rarely weedy (Di Tomaso, 1998).

Prior to its dormant phenological stage, saltcedar's foliage turns a yellow-orange to orange-brown color before leaf drop (Everitt and DeLoach, 1990). This phenological change starts in late fall or early winter seasons, although some isolated small populations generally do not change foliage until mid-January to early February (Everitt and DeLoach, 1990). Around the same time, the dominant mesquite is already leaf-off, and the willow leaf is dominated by brown, green and gray tones.

A field campaign was conducted on December 18-19 of 2005 along a foot

trail located just above Candelaria, Texas. Spectral measurements were taken

using a portable hand-held spectro-radiometer (ASD VNIR Field Spectrometer).

The sensor has a field of view of 25° and a spectral resolution of 1nm. The sky was

nearly cloud-free at the time of data acquisition, which was from 11 a.m. to 2 p.m.

(local time). Measurements were made on well illuminated foliage of various

species, including saltcedar, willow and mesquite, at various phenological

conditions. Locations of sample species and features were also recorded with a

hand-held GPS unit with sub-meter accuracy. A two level classification system

was defined in order to link field observations to image observations. Table 3.1

summarizes the two level classification system used in this study. While the focus

was on testing remote sensing observations at the landscape level, field samples

were available at the species level.

3.2.2   Image acquisition and preprocessing

The Airborne Imaging Spectroradiometer for Applications (AISA) sensor

system (Spectral Imaging LTD) was flown over the study site on 21 December

2005. The AISA imagery acquired has 61 bands with bandwidths of around 10

nanometers and spatial resolution of 1 meter. Five image strips of 10-km length

and 1-km swath were mosaiced and a subset of 2.3-by-10 km extracted for

accuracy assessment purposes. A Landsat 7 ETM+ (path 31, row 39) acquired on

19 December 2005 was tested in this study. Since the image was acquired in the

Scan Line Corrector (SLC)-off mode, a processing level 1G was required

(http://landsat.usgs.gov). Although data gaps were nearly absent in the subset of

Table 3.1: Two-level classification system used in the study.

Landscape level	Species level	Description
Invasive species	Saltcedar–Green	*Tamarix chinensis* L. with predominantly green leaves (brown-to-green tone)
	Saltcedar–Dry	*Tamarix chinensis* L. with predominantly dry leaves (orange-to-brown tone)
	Giant saltcedar	*Tamarix aphylla* (L.) Karst (evergreen)
Native riparian species	Willow	*Salix gooddingii* B. among others
	Mesquite	*Prosopis glandulosa* (honey mesquite)
	Poverty weed	*Iva* spp.
	Marsh weed	*Limnophila* spp.
Clear space/other land cover types	Herbaceous–Green	Green herbaceous plants and grasses
	Herbaceous–Dry	Dry herbaceous plants and grasses
	Creosote bush	*Larrea tridentata*, sparsely distributed
	Wetland	Emergent herbaceous wetlands
	Water	River, pond or lake
	Sand	Sandy bare ground
	Gravel	Barren gravel, gravel road
	Road	Asphalt paved road
	Roof	Any kind of house roof

the study site, thin cirrus clouds were present on the central part (Figure 3.2(a)), so an atmospheric correction process was necessary (FLAASH, Research System Inc.). Only bands 1-4 were used, as their wavelength ranges overlap with reference data from AISA and field spectra. These wavelengths are also the most useful for saltcedar discrimination (Everitt and DeLoach, 1990). The four bands were co-registered and re-calibrated to match the reflectance values from a synthesized Landsat image from AISA data (Figure 3.2(b)).

3.2.3   Reference data

Because of the intrinsic difficulties of collecting ground-truth fractional coverage in the field, reference data were derived from AISA imagery and field spectra. As suggested by prior work (e.g., Glenn *et al.*, 2005), a band reduction method based on the minimum noise fraction transform (MNF) was first applied on the AISA imagery to obtain 10 MNF-bands, which represented nearly 90 percent of the total variance. Detailed extensions of sixteen land cover classes (Figure 3.1-right), including two saltcedar classes (Table 3.1, species level), were determined through applying a maximum likelihood classifier (MLC, Richards and Jia, 1999) on the MNF-bands. Field spectra, coupled with the spectral angle mapper method (Kruse *et al.*, 1993), were used to produce potentially pure pixels for training the MLC. The classification result was then aggregated in three broad categories (Table 3.1, landscape level) and reference fractions produced by spatial aggregation to a 30-meter resolution. Uncertainties associated with reference fractions were also accounted by determining the entropy of MLC posterior

probabilities (Richards and Jia, 1999). Averages of 1-m resolution entropies within a 30-meter resolution pixel were used as uncertainty measures of the reference fractions. Two sample sets of 300 points each were randomly drawn for training and testing purposes. At each sampled site, four reflectance values from Landsat bands and associate sub-pixel fractions for Invasive, Native, and Clear categories were recorded. In addition, uncertainty values from the entropy band were attached to each fraction in the test data.

Figure 3.2(c) shows a map of reference sub-pixel fractions, where full sub-pixel coverage of saltcedar is shown in an intense red tone, full sub-pixel coverage of native riparian species is shown in an intense cyan tone, and full sub-pixel coverage of other land cover types are shown in white. Combinations of the three land cover types yield intermediate tones. In this figure, large red patches represent established stands of saltcedar that have monopolized the space and replaced the native species, whereas smaller patches (pink and dark cyan tones) represent incipient saltcedar invasion or areas where saltcedar remains an inferior competitor due to environmental stress (Sher *et al.*, 2002).

3.3   Methods

3.3.1   Linear spectral unmixing

In the linear spectral mixture (LSM) model, mixed spectra from remote sensing images are assumed to represent linear combinations of signatures from spatially segregated materials (end-members) that are present in the IFOV (Adams *et al.*, 1993; Gillespie, 1992; Milton, 1999). The relative contribution of

(b) (c)
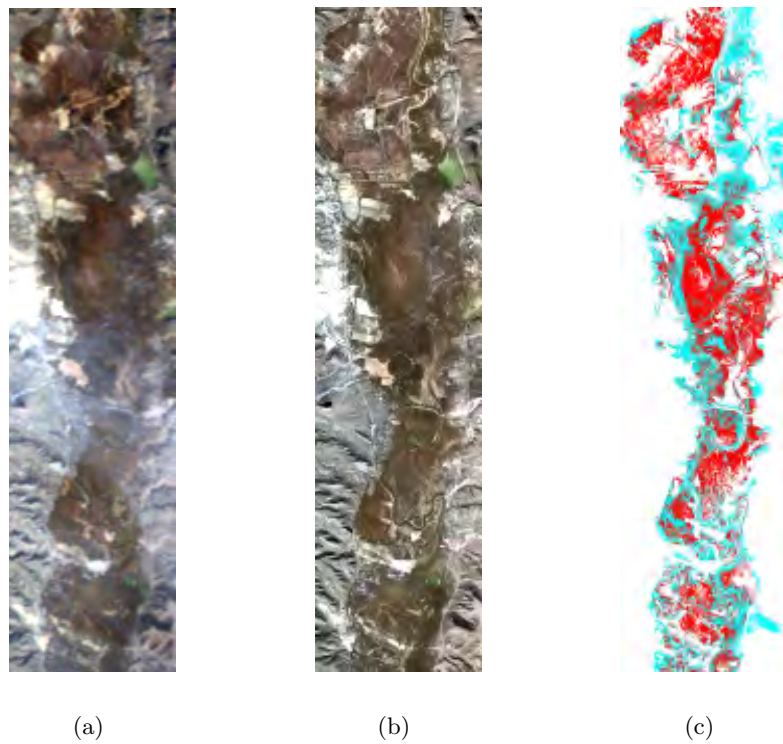
Figure 3.2: True-color composite of a subset of the Landsat ETM+ image acquired on December 19, 2005 (a), true-color composite of a synthetic Landsat image from an AISA image acquired in December 22, 2005 (b), and map of sub-pixel fractional coverage of Invasive saltcedar (Red) and Native riparian (Cyan) vegetation (c).

each end-member is, in principle, proportional to its areal coverage, and the process of inverting the linear relationships for inferring the relative cover of each material is referred to as linear spectral unmixing (LSU). LSU methods have become standard tools to determine the relative abundance of materials, land cover types, or even species composition from hyperspectral and multispectral imagery (Miao *et al.*, 2006). There are four linear methods, which differ in the way sub-pixel fractions are constrained. These are termed unconstrained LSU (UCLSU), sum-constrained LSU (SCLSU), non-negativity constrained LSU (NCLSU) and fully constrained LSU (FCLSU). Details on the formulation and solution of each LSU method have been provided in a number of references (see e.g., Chang and Heinz, 2000; Heinz and Chang, 2001; Hu *et al.*, 1999; Keshava and Mustard, 2002) and will not be reviewed here.

Image end-members for LSU methods were produced at the landscape level by averaging the spectra from training pixels having land-cover fractions above 0.95 (i.e., nearly pure pixels), whereas species-level end-members were selected from the original AISA imagery with the aid of GPS points acquired in the field. Figure 3.3 shows the location of end-members on the plane spanned by the two principal components (PC), which explain 99.6% of the total variance of the Landsat data. The two-dimensional histogram of mixed pixels is displayed as background image.
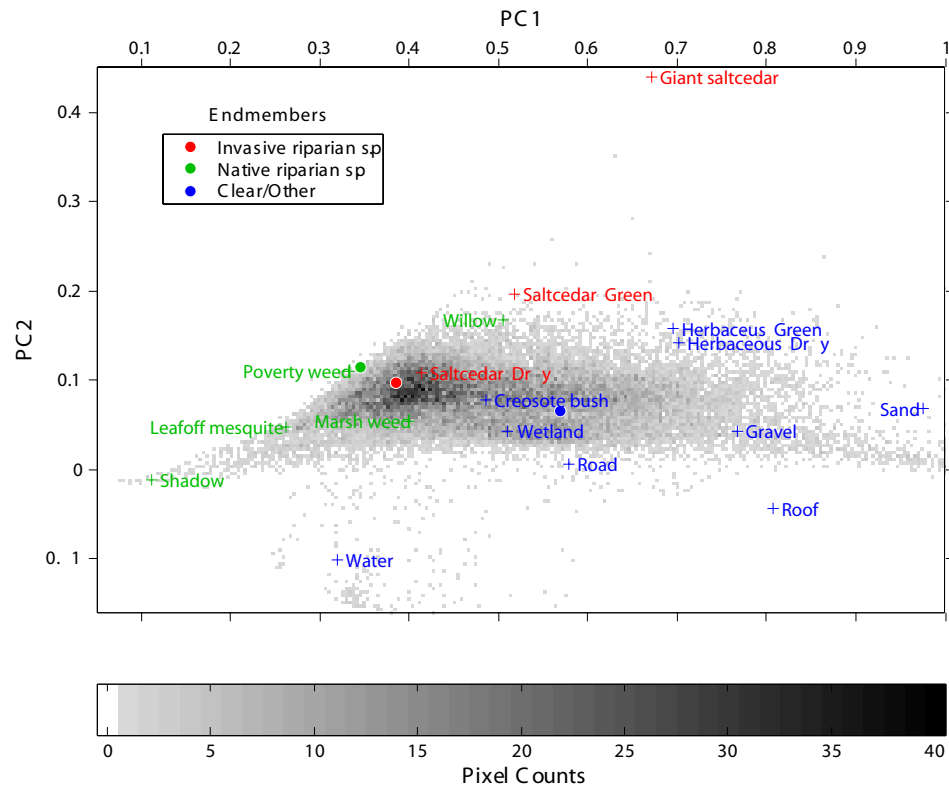
Figure 3.3: Relative location of end-members on the plane spanned by the two principal components of mixed pixels. The filled circles represent end-members defined at the landscape level, whereas the labelled crosses represent end-members at the species level. The background image represents pixel counts of Landsat pixels.

3.3.2 Non-linear spectral unmixing

In addition to the four LSU methods, three non-linear methods were tested in this study. The first method tested builds upon results from canopy scattering modelling (Huang *et al.*, 2007; Lewis and Disney, 2007; Smolander and Stenberg, 2005). These models allow for a simple relationship from leaf-level to canopy-level scattering (reflectance plus transmittance). The multiple-scattering approximation relates the canopy scattering to the leaf scattering through a nonlinear model that can be expressed as a Neumann series (Smolander and Stenberg, 2005). Considering a single end-member (e.g., leaf reflectance from one species), the model uses a single canopy structural parameter termed the re-collision probability (p), which is interpreted as the mean probability by which a photon scattered from a leaf in the canopy will interact within the canopy again. This photon-canopy interaction can be seen as a closed system with a positive feedback of gain p. Such a system can be graphically represented as shown in Figure 3.4(a), where the input corresponds to incoming radiation and the output corresponds to outgoing radiation. The outer box represents the reflectance off the canopy (mixed pixel), the inner box represents the reflectance off leaves (end-member), and the feedback link represents the multiple-scattering process. The system-like conceptualization makes it easier to extend the model for a general case with m end-members. The system diagram for the general case is shown in Figure 3.4(b). This model is hereafter referred to as multiple-scattering approximation (MSA). Noticeably, if the re-collision probabilities are forced to zero, the LSM model results. In the most general case, the total incoming radiation is split into intercepted proportions (α's)

by each end-member. A single photon that has interacted with the i-th end-member may interact with the j-th end-member with probability p_{ij} or escape re-collision with probability q_i. This system can be also expressed in mathematical terms using matrix notation (Appendix II). This is expressed in Equation (3.1) for each of n spectral bands:

$$y_i = \mathbf{q}^T (\mathbf{I} - \mathbf{X}_i \mathbf{P}^T)^{-1} \mathbf{X}_i \alpha, \quad \text{for } i = 1, \ldots, n \tag{3.1}$$

where y_i denotes the mixed pixel value for spectral band i, $\alpha = [\alpha_1 \cdots \alpha_m]^T$ is termed the abundance vector, $\mathbf{q} = \mathbf{1} - \mathbf{P1}$ is a vector of escaping probabilities, $\mathbf{X}_i$ is the diagonal matrix formed with the i-th spectral sample from each end-member, and $\mathbf{P} = [p_{jk}]$ defines a re-collision probability matrix. The inversion of these equations was implemented as a least square estimate of the abundance vector α and the structural canopy parameters, $\mathbf{P}$. Figure 3.5 exemplifies the effects of within-canopy and above-canopy end-members at the species level for linear and non-linear mixture models. While MSA and LSU methods perform similarly with above-canopy end-members, within-canopy end-members favor the MSA method. In practice, however, it is hard to acquire within-canopy end-members as they vary significantly across space. Therefore, above-canopy end-members at landscape level were used to test the MSA method (Figure 3.3).

The second non-linear method tested is a piece-wise linear method that consists of multiple runs of a FCLSU with varying end-members. The method makes use of end-members at the species level (Figure 3.3). According to the LSM paradigm, many of the spectral signatures recorded at the species level should be
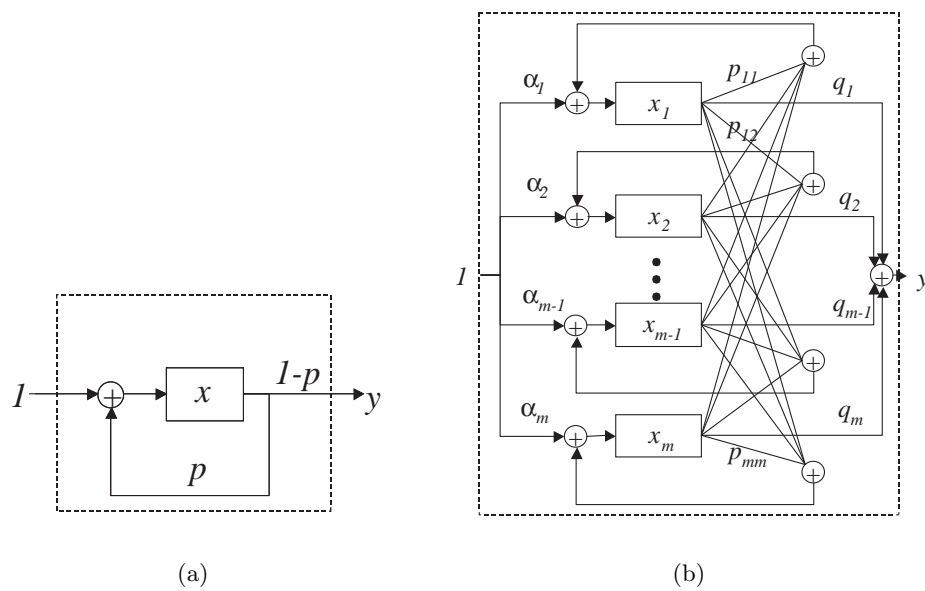
Figure 3.4: These flow diagram show the system-like representation of the multiple-scattering approximation model for single end-member (a) and multiple end-members (b).
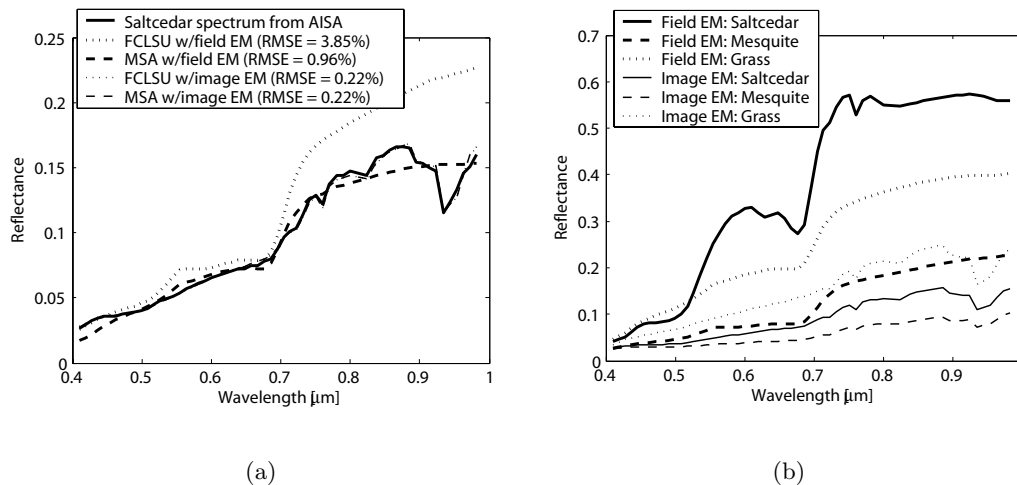
Figure 3.5: Linear and non-linear unmixing of a saltcedar spectrum from hyperspectral AISA measurement (a), and plots of within-canopy (field) and above-canopy (image) end-members (EM). The effect of multiple scattering is apparent in the attenuation of above-canopy reflectance.

considered mixed rather than pure pixels, as they are are interiorly located within a mixing space (Small, 2004). However, other studies have treated this signatures as end-members and proposed a multi-step unmixing strategy to deal with such interiorly located end-members (Carpenter *et al.*, 1999; Miao *et al.*, 2006). In that case, mixed pixels are spatially segregated at each step to ensure the end-members fall in the corner of the cloud of mixed pixels. In this study, the mixed pixels are segregated spectrally rather than spatially. The geometric interpretation of this method is depicted in Figure 3.6 for four end-members with two bands. In general terms, a subset of exactly $n + 1$ end-members is selected for each mixed pixel, where n is the number of spectral bands. The subset of end-members form a n-dimensional simplex that encloses the mixed pixel. A simplex corresponds to a
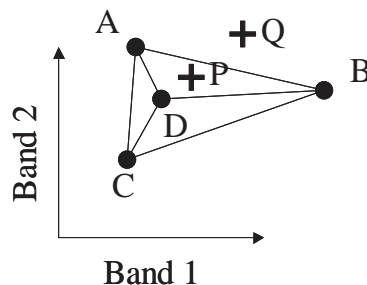
Figure 3.6: Tesselated linear spectral unmixing, in which end-members A, B and D are used to unmix an interior mixed pixel P, whereas end-members A, C and B are used to unmix the exterior mixed pixel Q.

triangle in the case of Figure 3.6. Simplices enclosing each mixed pixel are built as a Delaunay tessellation from the full set of end-members. While selected end-members can have non-null contributions to the mixed pixel, excluded end-members are forced to have a null contribution at that particular pixel. An exception occurs if the pixel is exterior to the convex hull of the full set of end-members. In this case, there is no simplex enclosing the pixel and all the end-members in the convex hull are used for the unmixing process. In the final step, abundances from the TLSU are aggregated to a landscape level according to Table 3.1.

The third method tested uses a backpropagation neural network (BPNN). A BPNN is a multi-layered, feed-forward network trained by the so-called backpropagation algorithm (Rumelhart *et al.*, 1986). For the unmixing problem, the BPNN associates mixed spectra with land-cover fractions by learning from training sets. Noticeably, the network cannot explain how mixed pixels are related to end-members within such a 'black-box' setting. The architecture of the network

consists of one input node per band, one output neuron per class and one hidden layer. The number of hidden neurons is generally selected by trial and error until a satisfactory result is achieved (Liu and Wu, 2005). Three BPNNs, each with one hidden layer of 5, 10 or 20 neurons, respectively (hereafter referred to as BPNN5, BPNN10 and BPNN20) were tested. A network with five hidden units was found to maintain the error characteristic for both internal and external data, so that no overfitting of the training data occurs, and had the additional advantage of minimal complexity.

3.3.3   Methods of accuracy assessment

The performance of each unmixing method was assessed using the root mean square error (RMSE) criterion on predicted reflectance and sub-pixel fractional coverage. In addition, the overall accuracy measure was derived by means of the sub-pixel confusion-uncertainty matrix (SCM) introduced in chapter 2. The SCM provided detailed information on the source and type of errors, in analogy to the traditional confusion matrix for crisp classifications (Congalton and Green, 1999). In the most general case, the SCM is formed by confusion intervals that reflect the uncertain nature of sub-pixel distributions. However, if the classification system consists of two or three classes, interclass confusions can be uniquely determined through Equation (3.2):

$$
C_{ij} = \begin{cases} \sum_n \min(\tilde{\alpha}_{in}, \alpha_{jn}) & \text{for } i = j \\ \sum_n \Delta \tilde{\alpha}_{in} \times \frac{\Delta \alpha_{jn}}{\sum_k \Delta \alpha_{kn}} & \text{for } i \neq j \end{cases} \tag{3.2}
$$

where $\tilde{\alpha}_{in}$ and α_{jn} denote the estimated and actual sub-pixel fractions for classes i and j at pixel n, respectively, and $\Delta \tilde{\alpha}_{in} = \tilde{\alpha}_{in} - \min(\tilde{\alpha}_{in}, \alpha_{in})$ and

$\Delta\alpha_{jn} = \alpha_{jn} - \min(\tilde{\alpha}_{jn}, \alpha_{jn})$ denote the over- and underestimation errors of classes i and j at pixel n, respectively.

3.4 Results

Table 3.2 summarizes the RMSE of sub-pixel retrieval from each method. In general, non-linear methods performed better than linear methods, with exception of the physically-based non-linear method (MSA) which was outperformed by a fully constrained linear spectral unmixing method (FCLSU). Neural networks achieved the best estimation in terms of sub-pixel class coverage estimation, but do not provide estimation of mixed reflectance nor explain the mixing mechanisms. While all linear unmixing methods can accurately predict the reflectance of mixed pixels, limitations exist for accurate sub-pixel area estimation from these methods, and specially through unconstrained and partially constrained linear methods. Even the best performed methods (BPNN, TLSU and FCLSU) led to errors of above 20% the pixel size, implying a limitation for small coverage detection. Figure 3.7(a) shows the degree to which estimated fractions conform to physically realizable fractional cover in terms of 1) how well they sum to unit, 2) how well they are non-negative, and 3) how well they are under unit. Figure 3.7(b) depicts the methods' performance in terms of overall accuracy and reliability in sub-pixel coverage retrieval from test samples. Comparison of errors from testing data and errors from training data indicated that both unconstrained and partially constrained linear spectral unmixing methods had lower error for the training dataset and much higher error for the test data (low reliability), indicating a

Table 3.2: Performance comparison of linear and non-linear spectral unmixing methods. See the text for further details.

Method		RMSE		Overall
		Reflectance [%]	Area [%]	Acc. (%)
Linear Mixing Model	UCLSU	0.1	75.8	14.0
	SCLSU	0.3	77.0	20.4
	NCLSU	0.5	39.7	55.9
	FCLSU	0.9	34.9	61.2
Non-linear Mixing Model	MSA	0.6	36.7	58.6
	TLSU	0.1	28.2	67.5
	BPNN5	N/A	23.9	71.5

tendency to over-fit the training data. The more reliable method was the TSLU.

Displays of retrieved sub-pixel fractions from the top-five methods are shown in

Figure 3.8. It can be seen that NCLSU and MSA overestimate the Invasive and

underestimated the Native class. Although similar in distributions, canopy covers

from BPNN5 and TLSU appear smoother than those from FCLSU. Moreover, pure

saltcedar stands seems to be better retrieved through TLSU than through BPNN5.

The best linear and non-linear methods, namely FCLSU and BPNN, were

subject to further analysis. Figure 3.9 shows box plots of estimation errors split

across various fraction ranges. In general, both methods tend to overestimate

canopy cover for low-density patches and to underestimate species canopy cover

for large-density patches. Errors from BPNN have less variability (height of boxes)

than errors from FCLSU, indicating better consistency in estimated fractions

within the same fraction range. However, median errors (center line of boxes) from

BPNN deviate more from zero than those from FCLSU, indicating larger bias in

estimations. The moderate to poor performance of each method could have been
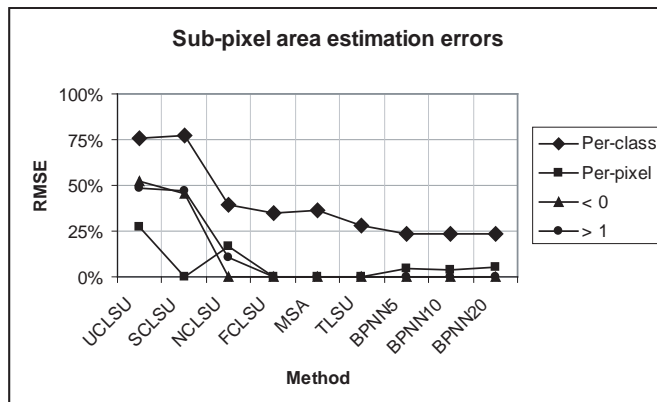
(a)
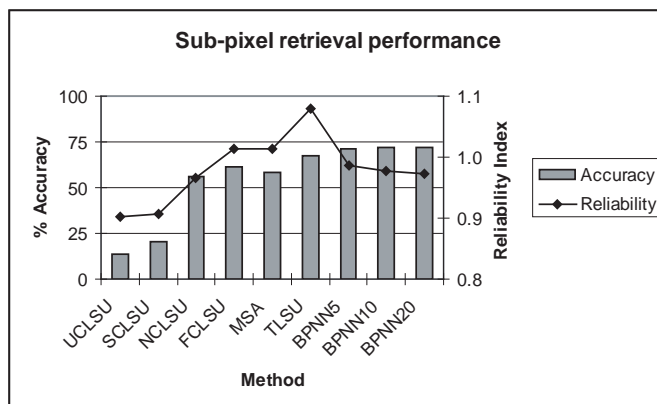
(b)

Figure 3.7: Estimation errors (a) and overall accuracy (b) for each method. Per-class errors represent standard errors on predicted fractions, per-pixel errors measure deviations from a sum-to-one condition, and below zero (< 0) and above one (> 1) errors represent average percent of estimated area below or above acceptable sub-pixel fraction values for any class. The reliability index correspond to the ratio of per-class training errors to per-class testing errors.
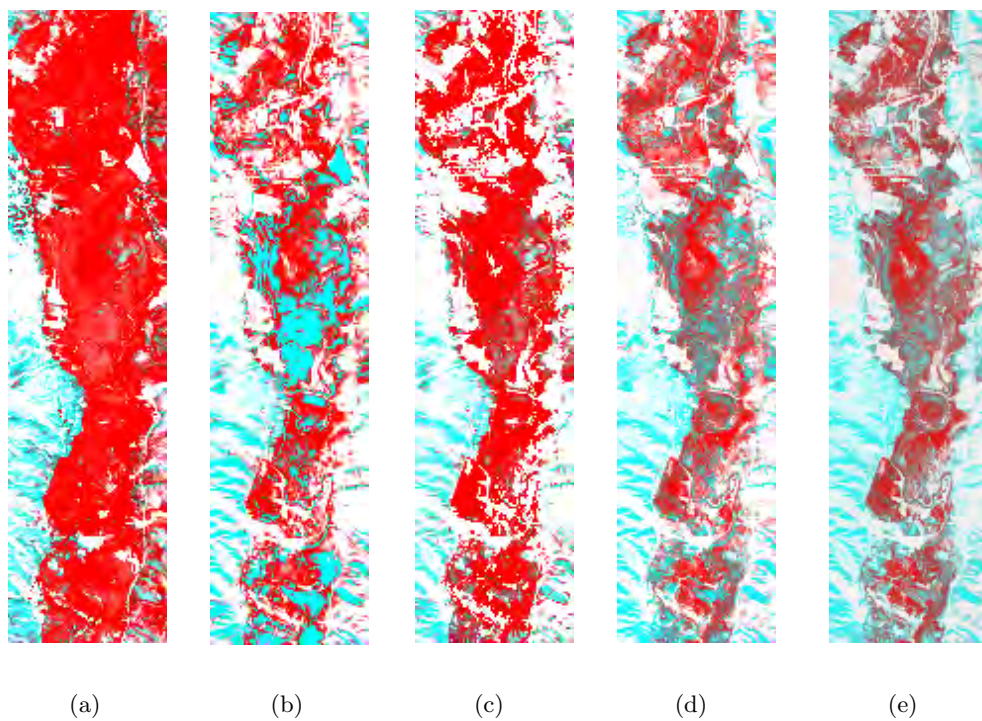
Figure 3.8: Sub-pixel canopy cover retrieved from several method. From left to right: NCLSU, FCLSU, MSA, TLSU and BPNN5 (see the text).

influenced by the ground-truth data used. An evaluation of the degree of association between prediction errors and fraction uncertainties revealed a significant linear correlation for FCLSU ($r = 0.1199$, $p < 0.05$) but not significant correlation for BPNN5 ($r = 0.0631$, $p = 0.2760$). Nevertheless, a nonparametric test based on the spearman rank correlation coefficient, which accounts for nonlinear association (Daniel, 1990), revealed that there is indeed a significant nonlinear correlation for BPNN5 ($r = 0.2434$, $p < 0.05$). Tables 3.3(a)-(b) show the sub-pixel confusion matrix for these methods. The most significant difference between these matrices is noted at the intersection of the first and second rows with the first column. BPNN5 presents higher agreement for Invasive class (69.2%) than FCLSU (46.8%), mainly due to the fact that FCLSU tends to confound more Invasive with Native (36.5%) than BPNN5 does (13.6%). This is also portrayed in the user and producer accuracies shown in Table 3.3(c). Note the highest difference in producer accuracy from FCLSU with respect to that from BPNN5. A significant higher overall accuracy (OA) was obtained from the non-linear method. In addition, the CPU time required for training and testing were measured on a conventional desktop computer. The training time for FCLSU consists of the computation time of the end-members, which was negligible since training data were available, whereas the training time for the BPNN5 was around 8 seconds. In contrast, FCLSU required nearly 3 seconds to unmix one thousand pixels, where BPNN5 took only 0.05 seconds.
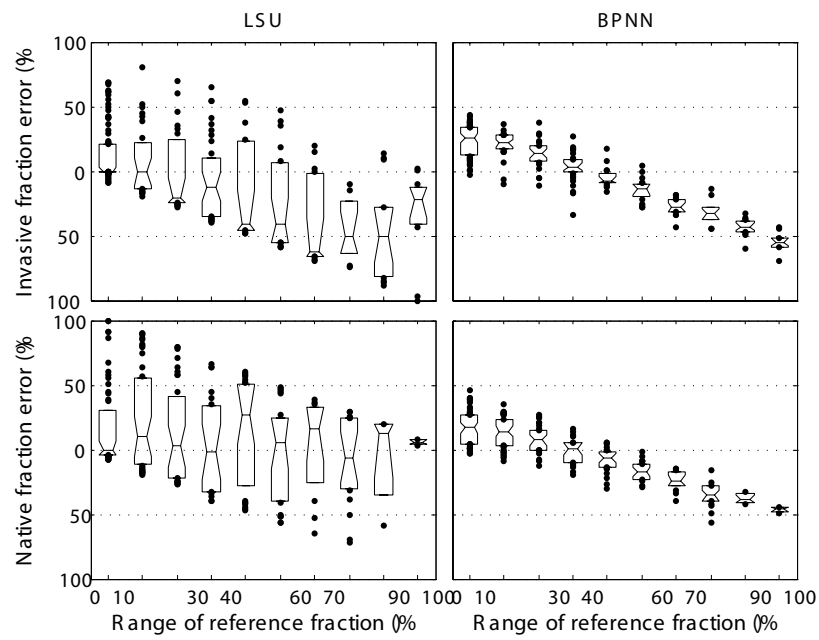
Figure 3.9: Notched-box plot of estimated-fraction errors. Fractions were estimated by FCLSU (left) and BPNN5 (right) for Invasive (top) and Native (bottom) categories. Each box has lines at the lower quartile, median, and upper quartile values. Data with values below or above the box limits represent outliers (dots). Notches represent uncertainty about the medians for box to box comparison.

Table 3.3: Results from best linear and non-linear sub-pixel mapping methods. Sub-pixel confusion matrix from FCLSU (a), sub-pixel confusion matrix from BPNN5 (b), and accuracy indices for each method (c).

	Reference (%)					Reference (%)			
Class	Inva	Nati	Clear	Total	Class	Inva	Nati	Clear	Total
Inva	46.8	17.8	11.7	24.9	Inva	69.2	16.1	18.2	34.0
Nati	36.5	71.2	23.1	42.5	Nati	13.6	72.8	9.6	30.9
Clear	16.7	11.0	65.2	32.6	Clear	17.2	11.0	72.3	35.5
Total	100.0	100.0	100.0	100.0	Total	100.0	100.0	100.0	100.0

(a)   (b)

	FCLSU		BPNN5	
Class	Prod. Acc.	User Acc.	Prod. Acc.	User Acc.
Invasive	46.8	60.3	69.2	65.4
Native	71.2	52.7	72.8	74.5
Clear	65.2	73.0	72.3	74.6
	$OA = 61.20$ $(\kappa = 0.4187)$		$OA = 71.45$ $(\kappa = 0.5711)$	

(c)

3.5   Conclusions

Sub-pixel classification of moderate resolution remote sensing, such as Landsat TM/ETM+, represents a cost-effective repeatable method for mapping the canopy cover of saltcedar and native species over wide extents, which is crucial to face the invasion problem on a continental scale. In this study, a number of linear and non-linear methods for spectral unmixing were tested for retrieval of saltcedar canopy cover. Image-based end-members were preferred over field-based (or spectral library) end-members, as they are guaranteed to represent measurements under nearly the same conditions of the image acquisition (Plaza *et al.*, 2004). The accuracy assessment was based on high-spatial resolution hyperspectral data through RMSE measurements and sub-pixel cross-comparison techniques (Silván-Cárdenas and Wang, 2008b).

Accuracy assessment results indicated that linear models can achieve low to moderate accuracy if properly constrained. Although the linear model can afford good predictions of mixed reflectance from Landsat, the relative contribution of end-members to the mixed reflectance does not accurately represent its areal coverage. It was shown that despite its physical basis and simple parameterization, a method that incorporates multiple-scattering processes (Huang *et al.*, 2007; Lewis and Disney, 2007; Smolander and Stenberg, 2005) has high requirements that cannot be met by multi-spectral Landsat data. Furthermore, while within-canopy end-members are essentially non-linearly mixed due to multiple scattering, MSA can only achieve moderate to low performance if used with above-canopy end-members, which are mostly linearly mixed (Roberts *et al.*,

1993). A piecewise linear unmixing method termed TLSU was implemented as a means of assessing to what extent the broadly defined end-members were a factor affecting the predicted species canopy cover from linear mixture models. The superior performance of TLSU over FCLSU demonstrated that the number and relative location of end-members within the cloud of mixed pixels might have been a major factor affecting the linear spectral unmixing results. Although lacking a physical basis, the TLSU method can be useful when the feature of interest cannot be described in terms of extreme points of the mixed pixel cloud, such as green vegetation, soil/rock substrate, and dark surface/shadow (Small, 2004). Results also confirmed prior findings showing that backpropagation neural networks can outperform linear and other nonlinear methods (Atkinson *et al.*, 1997; Carpenter *et al.*, 1999; Liu and Wu, 2005), yet they require numerous training samples that are hard to collect in the field. Less obvious is the fact that a significant higher efficiency, in nearly a factor of 60, can be achieved with a well-sized BPNN over the best linear spectral unmixing method. This means that, for example, if one were to process an entire Landsat scene ($\sim$50M pixels), once the end-members have been determined and the network has been trained, BPNN5 would take around 42 minutes, whereas FCLSU would take around 41 hours to run on a conventional personal computer. Therefore, the simplicity of the LSM model, largely responsible for its popularity in the remote sensing community, is not necessarily translated into a more efficient method for repeatable sub-pixel mapping tasks. Further research should also consider time complexity analysis of unmixing methods for tackling regional and global environmental problems by means of remote sensing.

Chapter 4

SUB-PIXEL CHANGE DETECTION: ANALYSIS OF SALTCEDAR SPREADING DYNAMICS

4.1 Introduction

Since its introduction in the mid-1800s as an ornamental, windbreak and agent of erosion control (Baum, 1967), saltcedar (*Tamarix* spp.) has expanded over 600,000 hectares along riparian corridors, from sea level to 2200 m, at a rate of 18,000 hectares per year (Di Tomaso, 1998; Everitt, 1980; Zavaleta and Royval, 2001). The most significant impacts of this drought-deciduous tree on invaded ecosystems are the increase of soil salinity, increase of wildfire hazards, and depletion of stream/river flow (Di Tomaso, 1998). Because of this, saltcedar has been subject to many control and environmental restoration efforts since the 1960s with varied success (Shafroth *et al.*, 2005). This study hypothesizes that remote sensing observations can provide new insights toward understanding its dynamics and assessing its impact on native ecosystems, that are crucial to support ongoing control efforts.

Being able to quantify extents and changes of invasive species represents a departure point toward disentangling relationships between an invasion process and underlying environmental fluctuations. For this matter, remote sensing change detection analysis techniques can play a crucial role (Hamada *et al.*, 2007; Joshi *et al.*, 2004; Lass *et al.*, 2005). A variety of change detection analysis techniques

have been developed for a number of applications (see reviews by Lu *et al.*, 2004, and Rogan *et al.*, 2002) and new applications are being constantly developed. However, the application of change detection techniques for saltcedar studies is still very limited. Change detection techniques through moderate resolution satellite observations can play an important role both in assessing effectiveness of ongoing biological control programmes (Carruthers *et al.*, 2006; DeLoach *et al.*, 2004) and in forecasting its potential spread by examining links between global climate change, species invasion, and the welfare of native ecosystems (Friedman *et al.*, 2005; Morisette *et al.*, 2006; Zavaleta and Royval, 2001).

Change detection analysis in the context of natural resources deals not only with detecting if a change has occurred or not, but also with identifying its nature and quantifying its aerial extents. Several change detection analysis techniques such as image differencing and image transformation techniques can only provide change/non-change information, whereas other techniques such as post-classification comparison techniques can provide a complete matrix of change directions (Lu *et al.*, 2004). In recent years, spectral mixing models (SMM) have been increasingly applied for land use/land cover change analysis (Adams *et al.*, 1995; Roberts *et al.*, 1998; Rogan *et al.*, 2002). As a classification approach, SMM is appealing because it can provide information on the relative abundance of land cover types at sub-pixel level, which is crucial for early detection of an invasion episode (Lass *et al.*, 2005; Silván-Cárdenas and Wang, 2008a). As a change analysis tool, however, it presents difficulties when it comes to determining change directions. The problem can be reduced to sub-pixel area allocation in a

cross-comparison of categorical sub-pixel maps, for which several alternatives have been devised (see Silván-Cárdenas and Wang, 2008b, and literature cited therein). This paper builds upon these ideas to demonstrate a post-classification change detection method based on sub-pixel classifications that can provide full information on change directions. The proposed method can be summarized in two steps. In the first step, sub-pixel classifications of multitemporal images are derived using the tesselated linear spectral unmixing method (TLSU) proposed by Silván-Cárdenas and Wang (2008a). In the second step, estimates of sub-pixel fractional changes are quantified by means of a cross-tabulation matrix termed the sub-pixel change matrix (SChM). The SChM is useful to estimate transition probabilities which can be further used for land cover change analysis and modeling.

The proposed approach is demonstrated on a segment of the Rio Grande river between the towns of Candelaria, Texas, and Presidio, Texas, using multitemporal Landsat TM/ETM+ data acquired at five dates within the period 1993-2005. Observed extents and changes were correlated with a number of environmental factors known to influence saltcedar spread (Cleverly *et al.*, 2002; Di Tomaso, 1998; Friedman *et al.*, 2005; Sher *et al.*, 2002; Stromberg, 1998; Tickner *et al.*, 2001; Warren and Turner, 1975; Zavaleta and Royval, 2001) in order to:

1. Determine the dynamics of saltcedar and associate native riparian species along the stretch of the river,

2. Test the role of several environmental factors in driving observed

distributions and changes, and

3. Determine whether or not a relationship between reductions in river flow and saltcedar coverage exists in statistically significant manner.

The organization of the paper is as follows. Section 4.2 provides a brief description of major environmental relationships as involved in saltcear invasion. Section 4.3 describes the study site and data used. Section 4.4 provides details on the image classification and sub-pixel change detection methods, and shows how the change matrix is applied in a Markov chain model. Section 4.5 presents results obtained with a discussion pertaining to the posed research questions above, and Section 4.7 provides conclusions drawn from the study.

4.2   Environmental interactions and saltcedar invasion

Saltcedar is a prolific, self-compatible plant that can produce over a half million seeds, which require prolonged moisture for germination and subsequent establishment (Di Tomaso, 1998; Warren and Turner, 1975). Because viability of seeds is relatively short, one major determinant of the successful establishment of saltcedar are the fluctuations in river flow during the peak flowering season (Warren and Turner, 1975). Although it can bloom almost the entire growing season (Everitt, 1980), saltcedar has one major peak of seed production in June to July and one minor peak in August to September (Warren and Turner, 1975). Its establishment occurs mainly along exposed areas of gently sloping river banks (Di Tomaso, 1998); however its growth during the first few years of establishment has been observed to be negatively correlated with neighbor density, suggesting a

limited ability to spread in presence of competition (Sher *et al.*, 2002). Once established, saltcedar is remarkably tolerant to a number of environmental stress conditions including droughts, inundations and high soil salinity (Cleverly *et al.*, 1997; Di Tomaso, 1998; Warren and Turner, 1975). The deep root system of saltcedar (up to 50 m) is the main trait responsible for its survival under stress (Di Tomaso, 1998). Observations in the San Pedro River, Arizona, has suggested that fluctuations in groundwater depth influence differently age structure of saltcedar and cottonwood stands (Stromberg, 1998). Moreover, saltcedar tends to increase in relative abundance at sites that show evidence of ground-water decline.

Despite the complex relationship of hydrogeomorphic factors that seem to affect saltcedar dynamics (Tickner *et al.*, 2001), empirical investigations have found that mean annual precipitation and mean annual minimum temperature are strong predictors of saltcedar occurrence on a continental scale (Friedman *et al.*, 2005; Zavaleta and Royval, 2001). Zavaleta and Royval (2001) reported that occurrence of saltcedar peaks at lowest mean annual precipitation in the US (47 mm/yr) and lowers to zero by 1150 mm/yr supporting the existing hypothesis that saltcedar is limited in distribution to relatively dry areas. Nevertheless, the same study reported a higher saltcedar occurrence within the precipitation range of 350 to 650mm/yr, occurring mostly in warm regions. Friedman *et al.* (2005) reported a positive correlation between saltcedar occurrence on 475 stream gaging stations in 17 states of the Western US and the mean annual minimum temperature, which supports the existing hypothesis of frost sensitivity of saltcedar. It is also well known by its researchers (see Zavaleta and Royval, 2001, and literature cited

therein), that saltcedar range and expansion rates are also limited by local elevation. Although it has been reported to occur as high as 3350 m above see level, it spreads very slowly after 1220 m.

The impact that saltcedar invasion has on the river flow is also an important and controversial issue. Estimates on water consumption by saltcedar vary greatly depending on location, maturity, density and depth to groundwater. Evapotranspiration estimates for saltcedar range from 0.7 to 3.4 m/yr depending on the measuring technique, site conditions, and duration of measurements (Shafroth *et al.*, 2005). Based on peer-reviewed scientific literature for the last 40 years, sap flux rates and sap wood area, and potential evaporation rates, Owens and Moore (2007) determined an upper bound of saltcedar water composition at tree-level on a daily basis as 122 L/d, (which is converted to 1.78 m/yr considering an average canopy area of 25 m^2, or to a larger value if the stand density is considered as well). Studies along the middle Rio Grande River in New Mexico have reported significant saltcedar evapotranspiration between May and October, with estimated maximum (around 6 mm/d or 2.19 m/yr) occurring in mid August (Cleverly *et al.*, 2002). In contrast, the water used by the native mesquite within May and September has been measured from 1 to 2.4 mm/d (0.36-0.88 m/yr) and around 1.2 yr/d for willow (see Scott *et al.*, 2000, and literature cited therein). The timing is relevant for testing the hypothesis that saltcedar consumes more water on an areal basis. If saltcedar has significant impact on the water flow, then the correlation between the loss of discharge within the segment of the river during peak evapotranspiration months and vegetation extent should be stronger for

saltcedar than for native plants. A conservative estimate of the overuse of water by saltcedar is over 0.3 m/yr respect to the water used by associated native species (Tamarisk Coalition, 2003).

4.3   Study site and data used

The study area is located in Presidio Valley, between the sister towns of Candelaria, TX-San Antonio del Bravo, Chihuahua, and Presidio, TX-Ojinaga, Chihuahua, from 1993 to 2005. At this site, the river banks have been taken up by saltcedar, and the native cottonwood (*Populus* spp.), that once dominated the area, is completely absent. The successful establishment of saltcedar in Presidio Valley has been attributed to two consecutive floods in 1941 and 1942 followed by a prolonged drought during the second half of the century and the subsequent abandonment of irrigation fields (Everitt, 1998), thus portraying saltcedar as an opportunistic rather than an aggressive colonizer.

The boundary of the study site was selected to match the Forgotten River Management project carried out by the University of Texas at Austin (UT Austin)'s Center for Space Research (CSR, 2007) for the US Army Corps of Engineers, and clipped at the top 6 km (3.7 mi) above Candelaria town and at the bottom 1.6 km (1 mi) above Presidio town in West Texas (Figure 3.1). The boundary of the Forgotten River Management project was produced by intersecting a 3-kilometer buffer surrounding the main channel centerline of the Forgotten River reach and a mask of areas with elevation above the river channel base elevation of 100 m or less (CSR, 2007). The total study area is

17,700.3 hectares. The average annual precipitation in the study period was less than 254 mm (10 inches), most of which falls during the summer growing season, and the average temperature was around 21°C (70°F) (Figure 4.2).

4.3.1   Image acquisition and preprocessing

Four Landsat TM images acquired in years 1993, 1996, 2000 and 2003 and one Landsat ETM+ image acquired in 2005 in the Scan Line Corrector (SLC) off mode (path/row = 31/39) were used in this study. All the images were acquired in December when senescent saltcedar is best discriminated from native willows (*Salix* spp.) and mesquites (*Prosopis* spp.) (Everitt and DeLoach, 1990). Table 4.1 summarizes the characteristics of the five Landsat images used. Image TM96 had minor striping noise that becomes apparent only after processing. Image ETM05 had cloud cover of 35%, but only 22% located in the lower-left quadrant, and even less in the subset of the study site, where clouds were nearly transparent and localized in the northern end. In addition to these images, one hyperspectral image acquired with the Airborne Imaging Spectroradiometer for Applications (AISA) sensor at 1-m resolution on Dec-21-2005 was used for radiometric calibration, and one ETM+ image registered in the UTM NAD27 coordinate system was acquired from the CSR. This image, hereafter referred to as ETM02, was acquired on Nov-11-2002 and was used only as spatial reference for co-registration.

Of the various requirements of preprocessing for change detection, multi-temporal image registration and radiometric and atmospheric correction are the most important (Lu *et al.*, 2004). All the Landsat images were clipped,
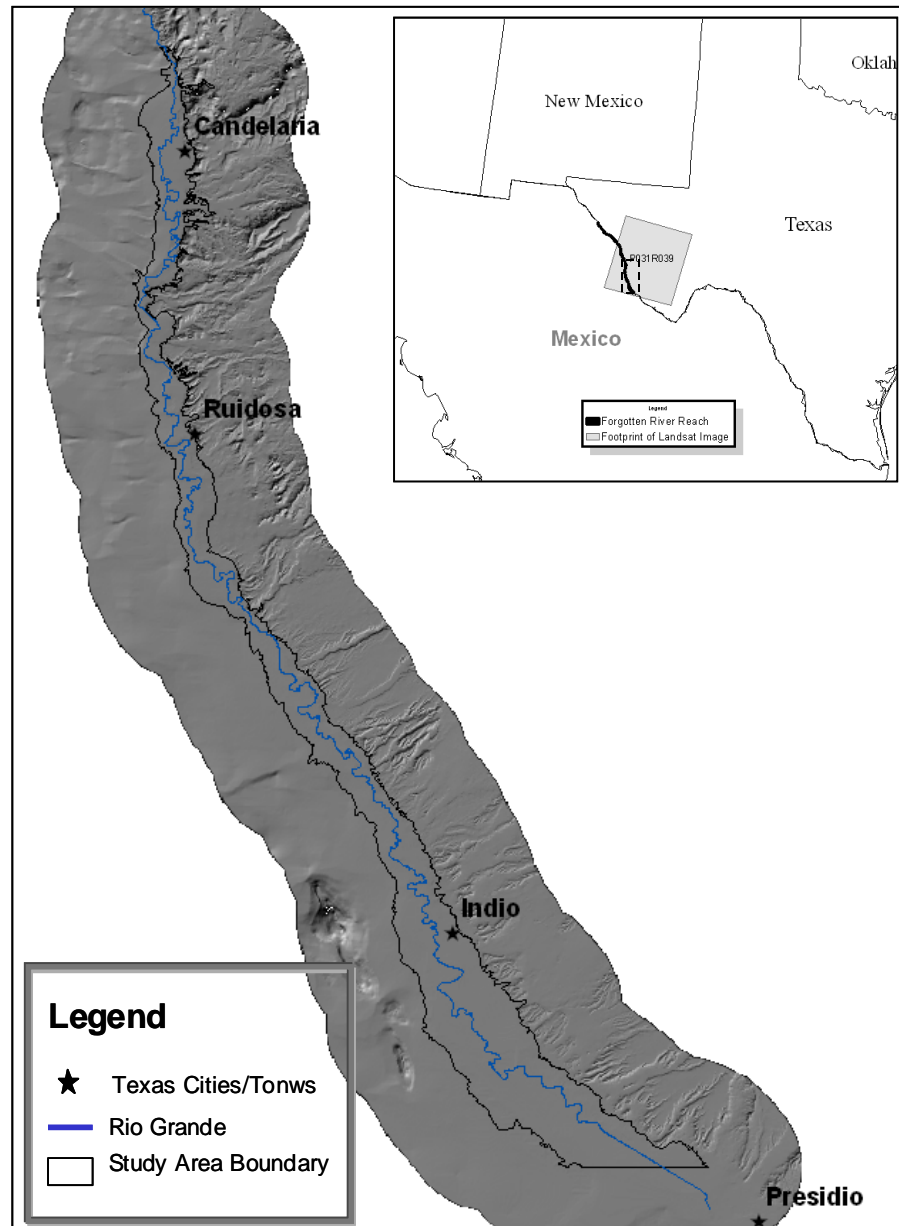
Figure 4.1: Geographic location and boundary of the study site.

Table 4.1: Characteristics of Landsat images used in the study.

Image ID	Sensor	Acq. Date	Acq. Time (GMT)	Sun Elev/ Az [deg]	Comments
TM93	TM5	Dec-26-1993	4:49 p.m.	28/147	Excellent quality
TM96	TM5	Dec-18-1996	4:49 p.m.	29/148	Minor striping
TM00	TM5	Dec-29-2000	5:07 p.m.	30/150	Excellent quality
TM03	TM5	Dec-22-2003	5:06 p.m.	30/151	Excellent quality
ETM05	ETM+	Dec-19-2005	5:17 p.m.	32/154	SLC-off, cloudy

co-registered, and normalized onto a common basis. The co-registration was performed using the image ETM02 as base. Ground control points between the base and the target images were manually paired. The number of control points varied from image to image (from least to most recent acquisition dates these were 12, 13, 17, 15 and 13, respectively), but the root mean square error was assured under one half the pixel size in most of the cases (0.57, 0.36, 0.64, 0.40 and 0.36, respectively). The warping function was a 1st order polynomial and the resampling method was the cubic convolution method. During the registration process the images were re-projected from WGS84 to UTM NAD27 coordinate system to match the base image.

The radiometric normalization was based on the iteratively re-weighted multivariate alternation detection (IR-MAD) transformation method (Canty and Nielsen, 2008; Nielsen, 2007). The IR-MAD method automatically detects pseudo invariant features by applying iteratively a spectral invariant transformation (the MAD transformation) on a pair of images. The normalization of the TM images was carried out sequentially starting with the latest image (TM03) and ending with the oldest (TM93). The AISA image was used as reference for the first image. Then the normalized TM03 was used as reference to normalize TM00, and so on.

By using the closest date as reference rather than a fixed date, the influence of changes in the normalization with the IR-MAD method is minimized for all the images. The ETM05 image was normalized using the AISA image as a base image and was subject to a further cloud removal processing. The cloud removal method used relies in the ability to sample the difference between the clean image (TM03) and the cloudy image (ETM05) at known sites of invariant features. This was possible by using the pseudo-invariant features detected with the IR-MAD transformation between the TM03 and the AISA images. Samples were then interpolated using geostatstical tools to create a cloud distribution map that can be subtracted from the cloudy image.

All image processing was performed with the ENVI image analysis environment (ITT Visual Information Solutions) and ArcGIS (Environmental Systems Research Institute). Extension to ENVI for the IR-MAD was acquired from Canty (2006).

4.3.2   Environmental data

This research used several datasets in order to investigate the role of some environmental factors known to influence saltcedar dynamics. Table 4.2 summarizes the characteristics and how each dataset was used in the study. Details on these datasets are provided below.

Monthly climate records maintained by the National Oceanic and Atmospheric Administration (NOAA)'s National Climatic Data Center (NCDC) were acquired from climatological stations at Candelaria, Texas (station number

Table 4.2: Characteristics and purpose of environmental data used in the study.

Environmental data	Characteristics	How used
1. Precipitation 2. Temperature 3. Discharge 4. Groundwater	Non-spatial, dynamical	Role in driving overall change
5. Loss of discharge		Impact on water availability
6. Elevation 7. Slope 8. Distance to river	Spatial, non-dynamical	Role in determining local capacity

411416/99999), and Presidio, Texas (station number 417262/99999). Figure 4.2 shows the climograph based on these datasets.

Daily discharge records maintained by the International Boundary and Water Commission (IBWC) were acquired for gauge stations at "Rio Grande Near Candelaria, Texas, and San Antonio del Bravo, Chih", and at "Rio Grande above Rio Conchos near Presidio, Texas, and Ojinaga, Chih." The total discharge for the growing season was computed from data recorded between 1-May and 31-October. The lowest discharge record (Figure 4.3) occurred in 2003. The loss of flow for each month was also determined by subtracting downstream flows from upstream flows. Since local storms and irrigation surplus may increase the river flow downstream, only positive differences (losses) of monthly totals between May and October were accumulated for each year. Figure 4.3 shows plots from these datasets.

As stated in Section 4.2, the level of groundwater is a major controlling factor of saltcedar dynamics. Groundwater depth measurements were provided by the Texas Water Development Board (TWDB) at both Candelaria and Presidio.
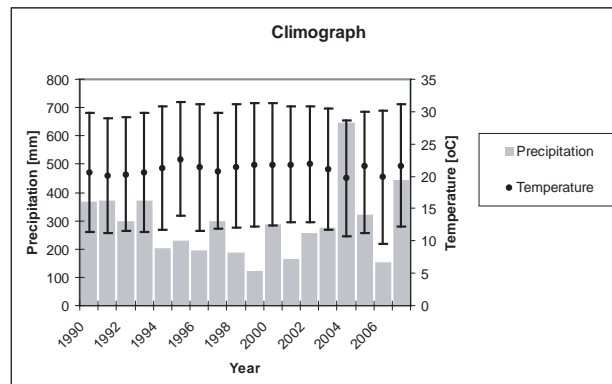
Figure 4.2: Climograph of the study area. Error bars indicate temperature ranges between mean minimum and mean maximum. Plots are based on the Annual Climatological Summary provided by NOOA National Climatic Data Center for Candelaria, TX (station 411416/99999) and Presidio, TX (station 417262/99999).

Of 75 wells located within the boundaries of the study area only 16 had measurements during the study period, most of which were made in 2000. The more or less continuous record throughout the period was generated by two co-located wells near Candelaria (state well numbers 5151807 and 5151808). Existing data gaps for years 1997, 1999 and 2003 were linearly interpolated. In order to obtain a better estimate of the average groundwater depth in the region, measurements from another well (state well number 7430706), not falling within the boundaries, though located near Presidio, was considered. Again, there were data gaps for the years 1997, 1998, 2001 and 2003 which were filled through interpolation. The average of groundwater depth measurements at the two extreme ends of the study area should be representative of values along the river length, yet it may not be representative of the groundwater depth of an across-section of the riparian zone. Nonetheless, this study did not consider spatial
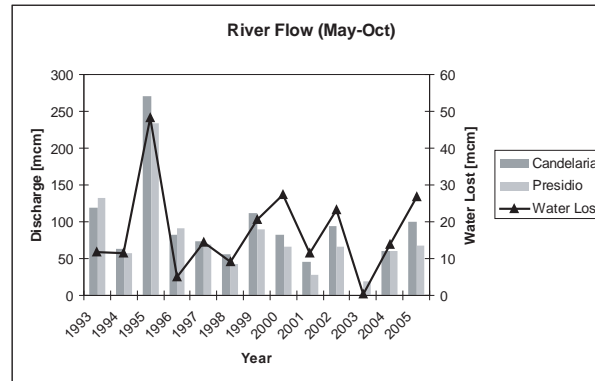
(a)
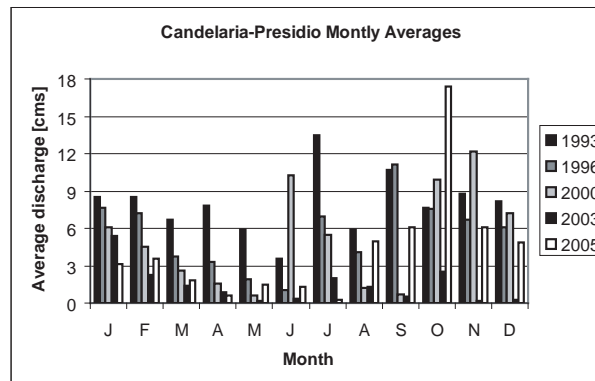
(b)

Figure 4.3: River discharge data. Total discharge for the growing season (May-Oct) at Candelaria and Presidio with estimated water lost in millions of cubic meter (mcm) (a) and monthly averages from the two stations during image acquisition years (b). The data were provided by the International Boundary and Water Commission (IBWC) with data for 2004 through 2007 provisional and subject to revision. Flow data for Candelaria during most of 2003 was missing.

Depth to Groundwater
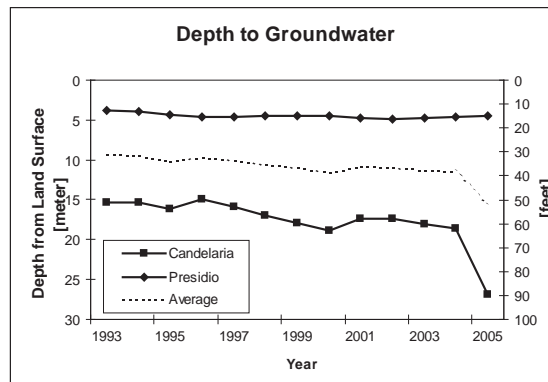
Figure 4.4: Variation of groundwater level from measurements near Candelaria and Presidio, Texas. Plots are based on the Water Level Table for Presidio county as provided by the Texas Water Development Board (TWDB). The time series for Candelaria is based on two wells identified by the state well numbers 5151807 and 5151808 and the time series for Presidio corresponds to the state well number 7430706.

or intra-annual variations of groundwater depth measurements. Figure 4.4 shows plots of these data, and the average over the two sites.

A digital elevation model (DEM) was provided by the CSR and was produced at 15-meter resolution by mosaicing the best available data from both the Mexico and the US sides of the river (CSR, 2007). The data were resampled at 30 meters to match Landsat resolution and because some artifacts became evident after processing at its original resolution, especially on the Mexican side. A slope layer was derived from the resampled DEM. The main river channel was extracted from the National Hydrography Dataset (NHD) and the distance to the main channel was produced through a minimum distance function available in ArcGIS.

4.4 Methods

4.4.1 Sub-pixel classification method

The multi-temporal normalized Landsat images were classified using the tesselated linear spectral unmixing method described in Chapter 3. The TLSU method is based on a two-level classification system. The level 1 defines the classes of interest at landscape level. The level 2 defines the classes down to species level, which are considered end-members within multiple spectral mixture models. The end-members are used to partition the entire cloud of mixed pixels based on their relative location within the radiometric space. Each subset of pixels is unmixed by inverting a mixture model that considers only the closest end-members in the radiometric space. In the last step, fractions are aggregated at the level 1. In this study, we considered three classes at level 1: Invasive, Native, and Clear. These classes were further split into 16 classes at level 2. The land cover class Invasive consists of two classes at level 2: Saltcedar-Green and Saltcedar-Dry, which are intended to capture the radiometric variability of saltcedar canopy at the time of image acquisition. Likewise, the land cover class Native is composed of the main woody riparian vegetation types in the area. This category is represented by four classes at level 2: Willow, Mesquite, Poverty weed, and Marsh weed. The class Clear included any other land cover type, but it is primarily dominated by open areas such as grasslands and wetlands. This category is represented by 10 classes at level 2: Creosote bush, Herbaceous-Green, Herbaceous-Dry, Row Crops, Wetland, Water, Sand, Gravel, Paved Road and House Roof. The use of only three broad categories in place of more detailed ones allows keeping the problem

manageable while retaining the most important information from a standpoint of invasive species. The above method was implemented in MATLAB programming system (The Mathworks Inc.) using a unique set of end-members for all the images. The end-members were extracted from the AISA image with the help of GPS points collected in the field two days prior to the acquisition of the image (Silván-Cárdenas and Wang, 2008a). Because the AISA image measures the electromagnetic spectrum only in the visible and near infrared regions, Landsat bands 5 and 7, which fall in the mid-infrared region, could not be used. Fortunately, the VNIR spectral region has proved effective in discriminating saltcedar from native species around the acquisition date (Everitt and DeLoach, 1990).

4.4.2   Sub-pixel change matrix

A cross-tabulation matrix, termed the sub-pixel change matrix (SChM), is introduced for the analysis of multi-temporal sub-pixel classifications. The definition of the SChM is based on a fundamental assumption of *minimal change* at sub-pixel level, an approach that is similar to that of the MIN-PROD operator proposed previously for map comparisons and accuracy assessment (Pontius Jr and Cheuk, 2006; Silván-Cárdenas and Wang, 2008b). The minimal change assumption acknowledges that not all changes occurring within the pixel are reflected as changes in the fractional cover. Undetected changes are primarily due to changes in location of classes within the pixel (sub-pixel location change) rather than to changes of areal extent (quantity change). The quantity change is given by the

absolute difference between co-registered fractions of two consecutive dates,

whereas the unchanged fraction (which may include the sub-pixel location change)

is given by the minimum between the two dates' fractions.

More formally stated, let α_i and β_i denote the sub-pixel fractions of class i

at initial and ending dates, respectively. Then, $u_i = \min(\alpha_i, \beta_i)$ defines the

unchanged fraction of class i, and $g_i = \beta_i - u_i$ and $l_i = \alpha_i - u_i$ define the gained

and lost fractions of class i, respectively. Since the total gained fraction must equal

the total lost fraction, they can be further split on pair-wise changes using the

expected sub-pixel change given by the probability p_{ij} that a random point from

the total change fraction had changed from class i to class j, i.e., $p_{ij} = l_i g_j / \sum_k g_k$.

Therefore, the change fraction from class i into class j can be expressed in

mathematical terms as in Equation (4.1):

$$C_{ij} = \begin{cases} u_i & \text{for } i = j \\ l_i \frac{g_j}{\sum_k g_k} & \text{for } i \neq j \end{cases} \tag{4.1}$$

The entries of SChM correspond to the sum of change fractions given by

Equation 4.1 over all pixels of the study site. Change fractions can be also

multiplied by the pixel area to reflect change areas rather than fractions. A

convention is used here when reporting the SChM that the diagonal cells

correspond to the persistent area for each class indicated by the row (or column)

labels, whereas off-diagonal cells correspond to the area changed from the class

indicated by the row label to the class indicated by the column label (see e.g.,

Table 4.4).

Change fractions defined by Equation 4.1 comply with the important

properties of diagonalization and marginal sum (Silván-Cárdenas and Wang, 2008b), which can be re-stated as follows:

i. *Diagonalization.* Sub-pixel changes are null if, and only if, the fractions at initial and ending dates are the same.

ii. *Marginal sums.* Marginal sums of sub-pixel changes match total fractions. More specifically, $\sum_j C_{ij} = \alpha_i$ and $\sum_i C_{ij} = \beta_j$.

4.4.3 Markovian transition dynamics

Because of the properties above, the SChM can be used to estimate the transition probabilities of a random finite-state time-homogeneous Markov chain model (Meyn and Tweedie, 2008). This idea is not new at all. Land research scientists have exploited this idea in empirical investigations of urban dynamics using traditional land cover change matrices from crisp classifications (see e.g., de Almeida *et al.*, 2003). What is novel in this study is the use of sub-pixel classifications in place of crisp classifications. Sub-pixel classification makes it possible to add the spatial component to the analysis as the transition probabilities can be estimated on a per-pixel basis. This is possible provided that land cover fractions can be treated as probabilities, i.e., the probability that a random point within the pixel belongs to a class.

In a Markov chain model, land cover changes occur randomly and stationarily. The process is entirely described by a transition probability matrix (TPM) $\mathbf{P}$, formed by the probabilities P_{ij} of change from class i onto class j

within one single period (e.g., one year). According to the Markovian principle, the TPM for n periods is obtained by multiplying $\mathbf{P}$ n times, i.e., $\mathbf{P} \cdot \mathbf{P} \cdots \mathbf{P} = \mathbf{P}^n$ is the n-period TPM. Elements of the n-period TPM can be estimated through the normalized changes C_{ij}/α_i. Furthermore, as long as the eigenvalues of $\mathbf{P}^n$ are strictly positive, $\mathbf{P}$ can be determined as the nth root of matrix $\mathbf{P}^n$ (Bini *et al.*, 2005). Once estimated, the transition probabilities can be applied for predicting land cover fractions. Specifically, if α_0 denotes the column vector of land cover fractions for a given pixel at initial time, then the land cover fractions after n periods can be determined as $\alpha_n = \mathbf{P}^n \alpha_0$. Noticeably, as n increases, α_n approaches the steady state of the system. The long-term equilibrium of a Markovian model does not generally match the dynamics of real systems, yet the stationary transition probabilities can be used as an approximation for the first few periods, after which conditions may change and new data is necessary to recompute the transition probabilities.

Two estimates of TPMs are independently considered in this study. The first estimation assumes space-invariance and consists of one TPM per n-period, each derived from the average change over all pixels of the study site. The second estimation assumes time-invariance and consists of one TPM per pixel, each derived from a weighted average change over all the periods, with weights corresponding to the number of years within each period.

4.5   Results

4.6   Validation of sub-pixel classifications

Figure 4.5 shows distributions of sub-pixel cover derived from the TLSU method. With the purpose of showing the continuum of mixture proportions and density of mixtures, these maps represent the values of native and invasive land cover fractions by means of a two dimensional color ramp (red-cyan-white). The two dimensional color ramp is simulated by setting the display channels as follows: $R = 1 - N$, $G = B = 1 - I$, where R, G, and B represent the display channels for red, green and blue, respectively, and N and I represent the fractional land cover of native and invasive species, respectively. According to this color scale, the pure red color corresponds to a pure, dense saltcedar stands, whereas pure cyan color corresponds to pure native stands. Combinations of the red and cyan tones represent mixed stands with various densities.

Given the difficulties to measure the actual vegetation cover in the ground and the lack of historic maps showing actual extends of the riparian vegetation, direct quantitative assessment of classification accuracy was only possible for the 2005 data using the AISA image as reference. In a related study, Silván-Cárdenas and Wang (2008a) performed a comprehensive accuracy assessment of sub-pixel classifications from a number of classification methods including TLSU. A similar approach was adopted here to assess the accuracy of the 2005 map. Groundtruth fractional cover were derived by the maximum likelihood classification of the AISA image into 16 classes (level 2) followed by spatial and thematic aggregation to match the Landsat resolution and the classification level 1. The overall accuracy,
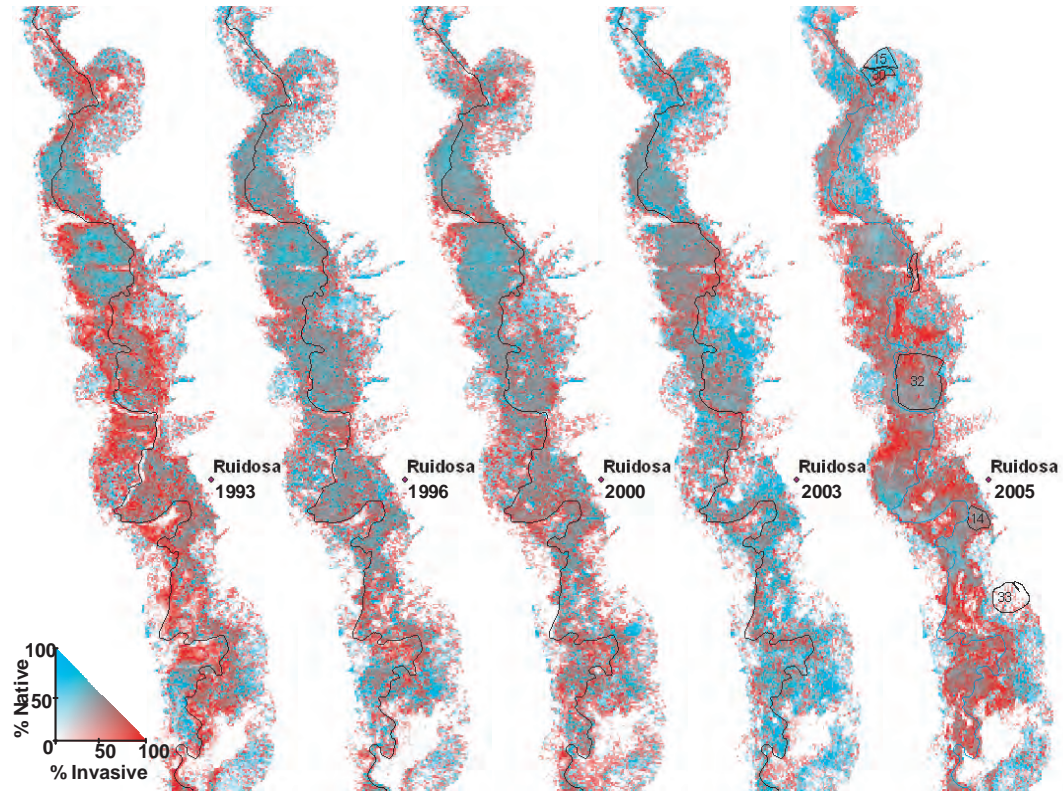
Figure 4.5: Multi-temporal sub-pixel classifications for a subset of the study site located in Ruidosa, TX. GPS polygons recorded in October, 2006 are overlaid on the classification map of 2005.

Table 4.3: Comparison between vegetation composition from remote sensing and field observations for the polygons shown in Figure 4.5.

Poly ID	Area [Ha]	Classification Saltc	Nati	Field observations
14	10.35	54%	39%	mostly saltcedar, apparently submerged
15	11.43	13%	49%	mixed mesquite/poverty weed/creosote bush
30	10.08	39%	46%	saltcedar, hard to see NAIP
31	6.39	58%	12%	mixed saltcedar/mesquite/willow/grasses
32	64.26	56%	36%	thick saltcedar near road/mixed mesquite
33	24.93	13%	5%	mixed creosote bush/mesquite/50% bare soil

based on random samples along the 10-km stretch covered by the AISA data, was $74\%(\kappa = 0.58)$. Because the segment corresponds to the cloudy part of the ETM05, the above accuracy provides a rather conservative estimation of the classification accuracy from other images, which had superior radiometric quality. In addition, inspection of 36 polygons recorded by the CSR crew in 2006 showed an acceptable match with computed fractional coverage from ETM05. Table 4.3 presents some examples of estimated areas for polygons shown in Figure 4.5 (right).

In order to perform a validation for the other datasets, the total coverage was assessed using the river flow data. It is widely recognized that vegetation fluctuation along riparian corridors are largely a resemblance of the fluctuations in river flow regimes (Auble *et al.*, 1994; Merritt and Cooper, 2000). In this study, total hectares covered by each species were correlated with peak winter and peak summer river discharge during the image acquisition years. Although non-statistical significant at 0.05-level, saltcedar land cover was better correlated with the winter peak discharge ($R^2 = 0.69, p = 0.08, n = 5$) than with the summer peak discharge ($R^2 = 0.32, p = 0.32, n = 5$), whereas the native species land cover
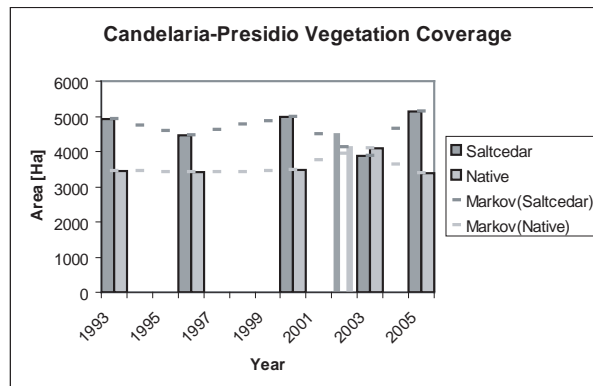
Figure 4.6: Estimate coverage of woody riparian vegetation along the segment of the Rio Grande River from Candelaria to Presidio, TX. Yearly estimations (discontinue lines) are based on a Markov model. Thinner bars correspond to estimated areas for 2002 from an external source (see the text).

was better correlated with the summer peak discharge ($R^2 = 0.60, p = 0.14, n = 5$) than with the winter peak discharge ($R^2 = 0.40, p = 0.26, n = 5$). In addition, an external estimate of the species coverage was derived from a land cover classification produced by the CSR (2007), which was based on the ETM02 image. Areas from CSR categories Saltcedar, Saltcedar (submerged), Saltcedar (mowed/new growth/sparse) plus 50% from Saltcedar/mesquite mix correspond to Saltcedar area here, whereas areas from categories Vegetation in water/shadow, Other dense shrub/scrub, plus 50% from Saltcedar/mesquite mix correspond to Native area here. Figure 4.6 shows a plot of the total hectares covered by each species together with yearly estimates yielded by the transition probability matrices and estimates from classification maps produced by the CSR.

4.6.1   Land cover changes

In order to provide an answer to the first research question, change areas were determined through the SChM for each time period. Table 4.4 shows the results. Total hectares covered by each species are given in the column and row totals, which correspond to the wide vertical bars plotted in Figure 4.6.

Contrary to expectations, the results support that there has not been a expansion of saltcedar range nor a continuous reduction of native species. The greatest change into saltcedar land cover type (+2606 hectares) occurred between 2003 and 2005 and was preceded by the greatest saltcedar reduction (-2437 hectares) between 2000 and 2003. These extreme changes of saltcedar concur with the extreme changes of native land cover type species but in the reverse direction (-1782 and +1713 hectares, respectively). These changes could have been influenced by the combination of two extreme events. The record low flow during most of 2003, under 1 milion m^3 and with only 15 days of precipitation above 2.5 cm, suggests that the water table was indeed significantly lower than the interpolated value shown in Figure 4.4. Therefore, as a drought-deciduous, saltcedar could have shed off leaves well before the acquisition date, which resulted in less saltcedar being detected while more native species from the under story became apparent. The following year, when precipitation peaked (averaging 650 mm), saltcedar appear to have recovered vigorously.

Table 4.4: Sub-pixel change matrix results. Tables are based on the time periods 1993-1996 (a), 1996-2000 (b), 2000-2003 (c), and 2003-2005 (d). Entries are in hectares and rounded to the nearest integer.

	Class	1996 Saltc	1996 Native	1996 Clear	Total	Change from
1993 Saltc	Saltc	2868	885	1159	4911	2043
Native	Native	741	2008	694	3443	1435
Clear	Clear	862	511	7974	9346	1372
	Total	4470	3403	9827	17700	4851
	Change to	1602	1395	1853	4851	
	Image diff.	441	40	-481		

(a)

	Class	2000 Saltc	2000 Native	2000 Clear	Total	Change from
1996 Saltc	Saltc	2898	744	829	4470	1572
Native	Native	816	2074	513	3403	1329
Clear	Clear	1261	653	7914	9827	1913
	Total	4974	3471	9256	17700	4814
	Change to	2076	1396	1342	4814	
	Image diff.	-504	-68	572		

(b)

	Class	2003 Saltc	2003 Native	2003 Clear	Total	Change from
2000 Saltc	Saltc	2537	1211	1226	4974	2437
Native	Native	549	2366	555	3471	1104
Clear	Clear	783	503	7970	9256	1285
	Total	3869	4080	9752	17700	4826
	Change to	1332	1713	1781	4826	
	Image diff.	1105	-609	-496		

(c)

Continued on next page.

Table 4.4: *Continued.*

| | Class | **2005** | | | Total | Change from |
		Saltc	Native	Clear		
2003 Saltc		2526	479	864	3869	1343
Native		1205	2298	577	4080	1782
Clear		1402	593	7757	9752	1995
Total		5132	3370	9199	17700	5120
Change to		2606	1072	1442	5120	
Image diff.		-1263	710	553		

(d)

4.6.2 Role of environmental factors

While a complex suite of environmental relationships appear to be involved in saltcedar invasion, simple correlations between land cover change types and environmental measurements can help to disclose the relative merit of each environmental factor in driving the overall land cover change dynamics. A number of environmental factors known to influence saltcedar dynamics were correlated with estimated yearly, space-independent transition probabilities for each period. The most significant factors in terms of correlation were the average annual precipitation (PRECIP1), the average mean minimum temperature (TEMP1), the peak winter discharge (DISCH1), the growing season discharge for the first year (DISCH2) and the maximum groundwater depth in the period (DEPTH1). The R-square values for these factors are summarized in Table 4.5. Although the analysis is based on only four time periods, some results were statistically significant at 0.05-level. With exception of DISCH2, all these factors influence, either positively or negatively, the changes from native vegetation and clear space

into saltcedar (P_{21},P_{31}). While an increase in precipitation favors these types of change, increase in temperature or groundwater depth seems to affect them negatively. These factors also correlate well with the probabilities of colonization of clear space by native species (P_{32}) and of persistence of the clear space throughout the period (P_{33}). Interestingly, these factors did not correlate well with the probability of change from saltcedar to native species on a yearly basis, perhaps due to a mismatch in the temporal scale between the environmental factors and the type of change. Indeed, when using a two-year transition probability, the change from saltcedar into native was also strongly correlated with precipitation (rightmost column of Table 4.5). Furthermore, this type of change was negatively correlated with growing season discharge during the first year of the period, suggesting that the replacement of saltcedar occurs mainly during the early stages of its establishment when its survival depends on the river flow. This is also in agreement with observations on competitive inferiority of saltcedar during its early stage (Sher *et al.*, 2002). That change probabilities P_{13} and P_{23} were not significantly correlated with any of the factors tested suggests that clearing process in the area may not be dominated by environmental interactions, but rather by human-induced disturbances.

In order to test the role of local elevation, slope and distance to main channel of the river, the temporal maximum of sub-pixel fractions were computed and grouped by percentiles for each dataset. The maximum fraction so-computed provides an indication of the cell carrying capacity assuming a proportional relationship between over story area covered and the number of individuals within

Table 4.5: R^2 values from yearly transition probabilities and environmental data. P_{ij} denotes the yearly transition probability from class i to class j, where i, j can take a values 1 for Saltcedar, 2 for Native, and 3 for Clear. Values in boldface were statistical significant on an F-test ($p = 0.05$), and values in cursive indicate a negative correlation. $P_{12}^{(2)}$ is a two-year transition probability.

Explanatory	P_{11}	P_{21}	P_{31}	P_{12}	P_{22}	P_{32}	P_{13}	P_{23}	P_{33}	$P_{12}^{(2)}$
PRECIP1	*0.2*	**0.9**	**1.0**	*0.3*	0.8	**1.0**	0.6	0.2	***1.0***	**0.9**
TEMP1	0.0	***1.0***	***0.9***	0.2	0.9	***1.0***	*0.4*	*0.2*	**1.0**	*0.8*
DISCH1	*0.0*	**1.0**	0.9	*0.2*	*0.9*	**0.9**	0.4	0.3	***0.9***	0.8
DISCH2	0.8	0.0	0.0	***1.0***	*0.0*	0.0	*0.3*	*0.1*	0.0	*0.0*
DEPTH1	0.1	*0.8*	***1.0***	0.1	0.7	*0.9*	*0.4*	*0.1*	**0.9**	*0.8*

the 30-by-30 meter plot defined by each cell. In addition, the sum of time-invariant

transition probabilities from each vegetation type into other land cover type, i.e.,

$P_{12} + P_{13}$ for saltcedar and $P_{21} + P_{23}$ for native species, were computed and

grouped by percentiles as well. These probabilities are referred to as extinction

probabilities because they provide indication on the extinction rates for each

species at each site. Means of maximum fractions and extinction probabilities were

estimated for each group, grouping variable, and vegetation type. Plots of

estimated means with confidence intervals are provided in Figure 4.7. In terms of

apparent local capacity, saltcedar was superior under varying topographic

conditions. The variation of local capacity along elevation gradients was the most

erratic, although with an overall positive trend. Slope variations showed little or

no influence in variability of local capacity, whereas distance to main channel had

the most structured covariation among the three. Local capacity of native species

seems nearly constant within a 300-meter buffer along the river channel, where

saltcedar's decays linearly. Beyond that point, both capacities would decay at

similar rates but saltcedar's remain greater than native's. In terms of extinction probabilities, the overall trends are reversed from those observed for local capacity. Saltcedar extinction was not significantly different from native species under varying topographic conditions; however, saltcedar mortality seems to increase slower than native's as one moves away from the channel. The apparent larger capacity or lower mortality for saltcedar at sites farther away from the the river channel may be explained by its deep roots which enable it to reach lowering water tables at these sites (Di Tomaso, 1998).

4.6.3   Relation of water lost with vegetation extents

Yearly Markovian estimates of vegetation coverage (Figure 4.6) were correlated with the loss of river flow during the growing season, i.e., the water lost (Figure 4.3). Figure 4.8 illustrates these relations. Although the estimated water lost within the segment of the river does not take into account contributions from local storms or losses from surface evaporation and local irrigation, there is no reason to think these fluctuations should favor one species in particular. However, the influence from extremely large fluctuations of river flow, especially during the winter season (Figure 4.3(b)), and/or the fact the Markov model may not capture the variations in vegetation coverage due to such fluctuations, was considered with care. Specifically, the points for the years 1995 and 2002, which showed relatively high values of water lost and for which the vegetation extent did not come directly from remote sensing observations, were not taken into account. Figure 4.8(a) shows that the water lost in the segment of the river is positively correlated with
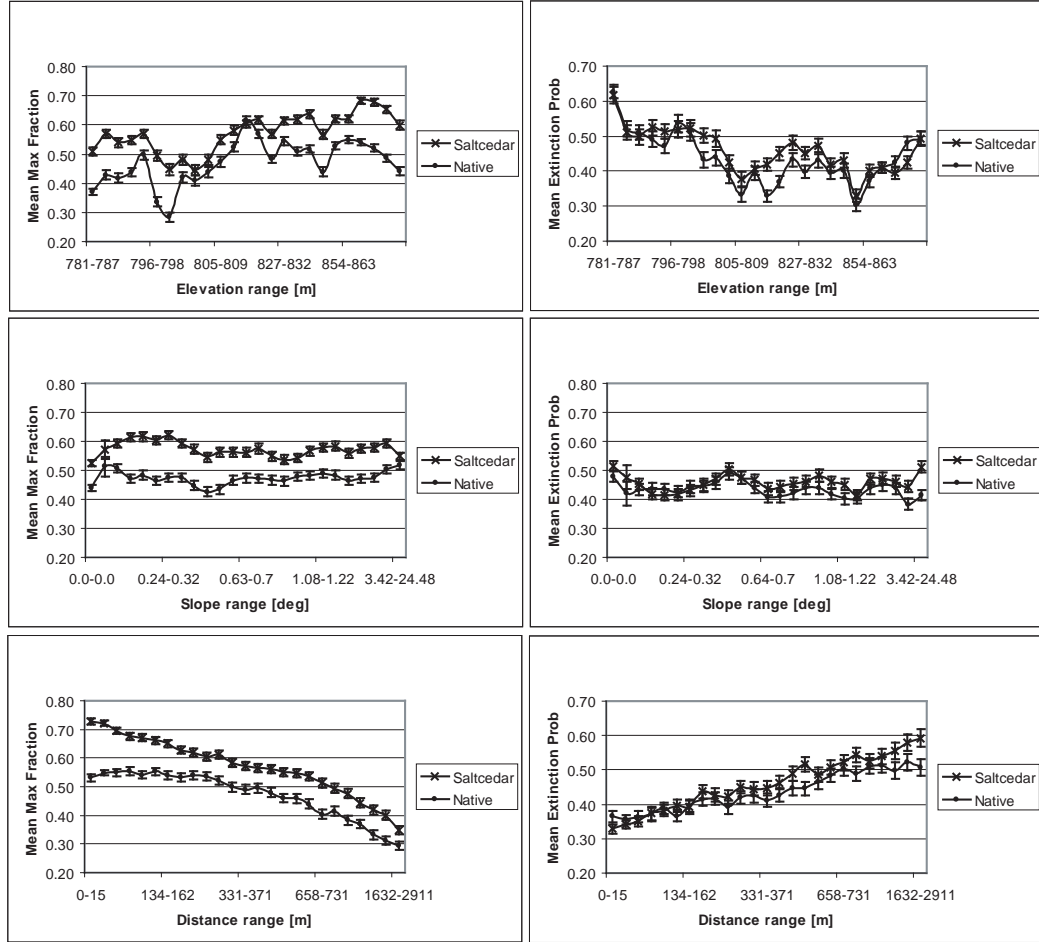
Figure 4.7: Estimate mean of maximum sub-pixel fractions (left column) and time-invariant extinction probabilities grouped by percentiles of terrain elevation (top), terrain slope (middle), and distance to main channel (bottom). Error bars indicate the confidence intervals of estimated mean at 0.05-level.

saltcedar extent ($R^2 = 0.69$, $p = 0.002$, $n = 11$). Furthermore, the slope of the regression line yields an estimated increment of water lost per hectare of saltcedar around 2 m/yr, which is in agreement with the average evapotranspiration regime of saltcedar (Shafroth *et al.*, 2005). In contrast, Figure 4.8(b) shows that the correlation of native species coverage with water lost was negative, yet not statistically significant at 0.05 level ($R^2 = 0.28$, $p = 0.094$, $n = 11$, $n = 11$).

4.7 Conclusions

This research demonstrated the application of a sub-pixel change detection technique for vegetation change analysis. Saltcedar invasion along the Rio Grande was taken as case study. A cross-tabulation matrix termed the sub-pixel change matrix (SChM) was adopted as the main change analysis tool because it provides full information on change directions. Furthermore, because the SChM fulfills the diagonalization and marginal sum characteristics (Silván-Cárdenas and Wang, 2008b), it is useful for estimating transition probabilities, which can be further correlated with change drivers or used as model for land cover change.

Contrary to suspicions, sub-pixel classifications of multi-temporal Landsat data acquired at five dates within the period 1993-2005 showed no continuous expansion of areas covered by saltcedar nor continuous reduction of areas covered by native species. Nonetheless, results from the change detection analysis suggests that saltcedar dynamics is more sensitive to environmental fluctuations, and confirms its ability to recover from droughts and periods of groundwater drop (Smith *et al.*, 1998). Simple correlations between estimated yearly transition
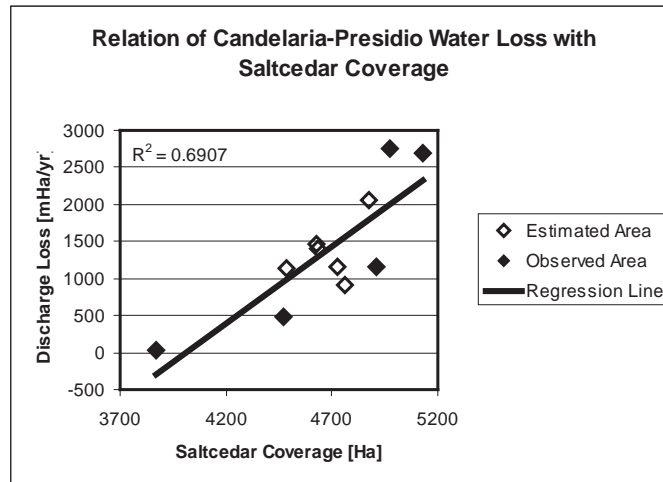
(a)
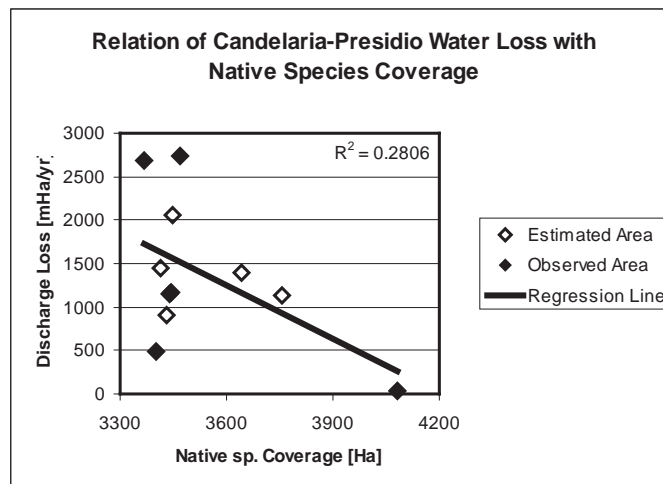
(b)

Figure 4.8: Relationship between vegetation extent and monthly averages of discharge loss of the Rio Grande between Candelaria and Presidio, TX.

probabilities with environmental data suggests that the most significant correlates of changes occurred in the study area were the average annual precipitation, the average minimum temperature, the peak winter discharge and the maximum groundwater depth in the period. The interdependency of these factors was evidenced by the fact that they correlated similarly (except for a sign) with the same types of changes (Table 4.5).

Although saltcedar occurrence has been shown to be negatively correlated with annual precipitation when considering a wide range of precipitation regimes, it is also true that such relation is reversed within the precipitation range from 350 to 650 mm/yr, which occurs mostly in warm regions (Zavaleta and Royval, 2001). Since this much narrower precipitation range matches the precipitation regime of the study site, it is then expected that the increase of precipitation stimulates the displacement of native vegetation by saltcedar and, at the same time, promotes the colonization of bare exposed soil by either native or invasive species. The issue is not simply that an increment of precipitation leads to an increment of change from native into saltcedar. As a matter of fact, the reverse change direction is also stimulated by increments in precipitation, but this type of change would occur slower. Therefore, the associated traits that enable saltcedar to grow faster under favorable conditions is what may be causing the displacement of the native vegetation. Closely related to the annual precipitation was the peak winter discharge (October-March). The extreme discharge during this season (especially during October-December, see Figure 4.3(b)) can promote more channel movement, vegetation scour, sediment reworking, and thus provides prolonged

moisture essential to sustain seedlings and exposes competition-free seed beds for both the native and non-native species (Stromberg, 1998). Although the mean minimum temperature has been shown to correlate positively with saltcedar occurrence on a large scale (Friedman *et al.*, 2005), on a local scale it correlates negatively with the displacement of native species by saltcedar. The mechanism is related to the maximum groundwater depth because at higher temperatures the water table drops due to high evapotranspiration rates. Under these stress condition, the population dynamics (or the rate of change in areas covered by such population) for both native and non-native species tend to slowdown.

Not surprisingly, the discharge during the first year of the period was the only factor that correlated well with estimated transition probabilities from saltcedar land cover into native species land cover, thus confirming that hydrologic regimes represent an important equilibrating force that may aid both to maintain native species and to control the proliferation of saltcedar (Busch and Smith, 1995; Stromberg, 1998). The comparison between mean maximum sub-pixel fractions suggested that the local capacity (within a 30-by-30m plot) is superior for saltcedar than for native species under varying topographic conditions (defined in terms of elevation, slope, distance to main channel). Likewise, the comparison between extinction probabilities (transition probabilities from each vegetation type into other land cover type) confirmed the lower extinction rate of saltcedar at increasing distances from the river channel. This result is consistent with the physiological traits that enable saltcedar to survive in the upland habitats where the native species cannot survive (Di Tomaso, 1998).

Although not consistently increasing throughout the period, saltcedar extent was positively correlated with the loss of discharge in the river reach, confirming a long suspected significant impact in water availability of the region. In contrast, a relationship between the extent of native species and the loss of discharge could not be established. Although estimated water lost within the segment of the river does not take into account contributions from local storms or losses from surface evaporation and local irrigation, estimated consumption by saltcedar was consistent with field measurements (Cleverly *et al.*, 2002; Shafroth *et al.*, 2005). This is by no means a recommendation on how to estimate water consumption by saltcedar, but rather a demonstration where remote sensing observations coupled with a modeling approach are able to confirm suspected impacts on water availability.

Chapter 5

LINKING LAND COVER CHANGE TO POPULATION DYNAMICS: A STUDY OF SALTCEDAR INVASION

5.1 Introduction

When a species colonizes a new area, it spreads across that area in the form of an invasion wave. The speed of this wave is determined by the vital rates of the population such as births and deaths as well as the dispersal capabilities of each species (Alpert *et al.*, 2000; Higgins *et al.*, 1996; Higgins and Richarson, 1996; Shea and Chesson, 2002). Means to measure consistently such vital rates are of great importance to invasive species research and to many ecological studies (Marco *et al.*, 2002; Rees and Paynter, 1997; Scanlon *et al.*, 2007). Among other things, this requires the acquisition of information related to population density and distribution, which is generally unavailable and prohibitively expensive to collect by direct means (Joshi *et al.*, 2004; Turner *et al.*, 2003). Such information is particularly valuable for the calibration and/or validation of spatially explicit models of invasion (Marco *et al.*, 2002; Nehrbass *et al.*, 2007).

To date, remote sensing has served as a valuable means to derive land cover information, which can be considered as a first-order analysis of species occurrence (Turner *et al.*, 2003). Nevertheless, limitations still exist when it comes to detecting understory plants or animal species (Joshi *et al.*, 2004). While high-resolution remote sensing have made it possible to detect sparsely-distributed

individual tree crowns, scrubland-type ecosystems, where plants share virtually the same space, still represent a big challenge because occlusions prevent direct observation from afar. Even with the use of the state-of-the-art hyperspectral sensors, with which one may have access to the vertical structure of canopies by explicitly modelling the multiple scattering phenomena (see Chapter 3), the challenge of separating individual tree crowns in such a scrubby environment would remain. This study hypothesizes that only when the land cover change is properly linked to the underlying population dynamics, one can have access to certain population parameters of densely forested areas from remote sensing observations.

Instead of looking at increased resolution data (either spatial or spectral), the alternative described in this chapter exploits the temporal information embedded in bi-temporal or multi-temporal sub-pixel fractional canopy cover estimations from Landsat measurements. An inference of the proportion of hidden plants in the understory of canopy-dominant plants is enabled by formulating a spatially explicit metapopulation model of the underlying dynamics and linking it to a land cover change model. The latter is referred to as the COEXOD model for its parameterization in terms of species COlonization and EXtinction probabilities, as well as in terms of canopy Occlusion and Dominance. The model parameter estimation is carried out by matching the COEXOD model with the yearly sub-pixel change matrices introduced in Chapter 4. The spatially explicit metapopulation model presented here is largely inspired in the traditional competition principle of ecology (Vandermeer and Goldberg, 2003). Although an attempt has been made to incorporate some of the major species traits and factors

suggested by previous works as involved in plant invasion processes (Higgins and Richarson, 1996; Marco *et al.*, 2002), the model has been kept as simple as possible. Indeed, it is not the purpose of this modelling approach to accurately represent the complex interactions among the native species assemblages, the invader and the habitat itself, as envisaged by much of the invasion ecology research (Alpert *et al.*, 2000; Higgins *et al.*, 1996; Higgins and Richarson, 1996; Shea and Chesson, 2002), but rather to demonstrate how a simple population dynamics model can be matched to remote sensing observations, and how such observations can lead to inferring population parameters that may be verifiable with empirical observations. Although it is shown how the model can be specified at the level of species traits, it is at the level of extinction and colonization rates where remote sensing observations are shown to be useful. Because the parameters at the level of species traits are not accessible through remote sensing, the parameter selection at this level can only be guided by knowledge from ground observations. The metapopulation model is also proposed here as hypothesis-testing framework on the invisibility under competition.

In sum, the study presented in this chapter 1) addresses the general questions of how remote sensing can be better applied to infer population parameters by using a modelling approach, 2) investigates the spatio-temporal pattern of extinction and colonization rates of saltcedar in Western Texas, and 3) inquires about the role of the interspecific competition on the rate of advance of the invader and on the persistence of the native species in a simulated invasion. The remaining of the chapter is organized as follows. The spatially explicit

metapopulation model is described in Section 5.2, whereas the derivation of the land cover change counterpart is presented in Section 5.3. The results on population parameter estimation along Western Texas are presented in Section 5.4.1, and the results on the test of invasivenss under competition are presented in Section 5.4.2. The main conclusions are summarized in Section 5.5.

5.2   Spatially explicit metapopulation model

The spread of invasive species, like many biological processes, exhibits a high degree of complexity that makes it hard to develop analytical approaches to model the process. The analysis of such a complex process is more amenable through computational models such as cellular automata (Wolfram, 1984). This approach has been widely used to study spatiotemporal patterns of plant distribution (Keymer *et al.*, 1998; Nehrbass *et al.*, 2007) invasiveness and speed of invasion (Kawasaki *et al.*, 2006; Marco *et al.*, 2002) as well as competition interactions (Silvertown *et al.*, 1992). In its most elementary form, a cellular automaton consists of a discrete simulation of changes on cell states. Changes in cell states are dictated by a number of transition rules that are local in nature, but can incorporate external factors as well. The cellular automaton described in this chapter is an attempt to model explicitly the main factors suggested by previous works as involved in a plant invasion process. It is built upon the ideas of metapopulation models (Gotelli, 2001, Ch.4) and competition principles (Vandermeer and Goldberg, 2003).

5.2.1 The invasion system and model parameters

The woody riparian native species that are replaced by saltcedar include mesquite (*Prosopis* spp.), cottonwoods (*Populus* spp.) and willows (*Salix* spp.) (Di Tomaso, 1998). In this study, saltcedar is taken as a prototype non-native invasive species and mesquite is taken as the prototype native species for the purpose of model parameter selection. Values for the selected parameters and their meaning are provided in Table 5.1. The model parameters that relate to species invasiveness are life history traits (mean maximum longevity, mean seed dispersal distance and age of reproductive maturity), and demographic traits (annual adult survival probability, annual seed production, mean germination probability and juvenile survival probability). The reasons for selecting some of these values are explained below. The model parameters related to habitat invasibility include the carrying capacity and the interspecific competition interactions. These are explained in the following subsections.

Saltcedar spreads both vegetatively and by seeds. Invasion of saltcedar typically occurs in bare, moist, and exposed areas. A single mature saltcedar plant can produce around half million of seeds per year (annual seed production per plant of 500000, Warren and Turner, 1975). Seeds are quite small and light (0.1 mg). The seeds have a tuft of hair on the end, which enable them to travel several kilometers downwind from release sites (Warren and Turner, 1975; Young *et al.*, 2004), or can be carried and deposited along sandbars and riverbanks by water. Because the range of seed dispersion varies a lot depending on wind conditions during seed release, here I picked a conservative value of 1 km for the long distance

dispersion range. The tiny seeds of saltcedar have high initial viability, but for relatively short-time periods (5 weeks under normal conditions, Di Tomaso, 1998). Although germination occurs within 24 hours following contact with water, it requires wet soils for several weeks. Young *et al.* (2004) have observed that saltcedar seeds germinate over a large range of temperatures, ranging 0-6% for very cold seed beds and 75-100% for optimal temperature profiles. In the model described below, I considered a germination rate of 40%, which is within the fluctuating and cold regimes defined by Young *et al.* (2004). Although saltcedar seedlings tend to be more abundant than mesquite seedlings, its mortality is also much greater resulting in similar densities after the third year (Sher *et al.*, 2002). Seedling survival depends on a number of biotic and abiotic factors. Sher *et al.* (2002) have reported a mortality of around 90% for saltcedar and around 40% for mesquite during the first year. In order to to reflect the extreme situation when the survival condition for the native species at the seedling stage is optimum, I set the probability of juvenile survival to 0.1 for saltcedar and to 1 for mesquite. Saltcedar seedlings may grow up to a foot a month in early spring (3 to 4 m in one year). From germination, it takes one or two years to develops into a small flowering tree (Di Tomaso, 1998). In the model, the age of reproductive maturity of saltcedar was 2 years and for mesquite was 5. Once developed, saltcedar is remarkably tolerant to mechanical injury as well as a variety of environmental conditions including drought, floods and high soil salinity. The typical lifespan of saltcedar has been reported around 75 to 100 years (Di Tomaso, 1998). Here I picked a mean maximum longevity of 80 years. On the other hand, mesquite

reproduces only by seed and not vegetatively. Honey mesquite seeds are borne in pods which are about 8-12 inches long and contain 10-30 seeds per pod. The production of pods varies per plant and per year, but the average value is around 800 pods/plant/yr, which would yield an average seed production per plant of 16000. A much lower number was selected (10000) to reflect the fact that only a portion of this seeds become available for germination. Specifically, most pods that fall to the ground are destroyed by insects or fungi or are consumed by animals. Seeds germinate within six hours of wetting at round 34^oC and can remain viable for many years. This storage effect of long viability of mesquite seeds is not considered in the model. Germination occur principally during early spring and late fall when soil moisture is favorable. Seeds are dispersed away from the parent tree by foraging animals in the process of consuming the pod (Ansley *et al.*, 1997). The dispersion range of mesquite seeds is unknown, but it is generally much shorter than saltcedar's (here I selected 500 m). Old mesquite trees (> 3 years) can tolerate fire or other disturbances by resprouting from the bud zone if the aboveground parts are destroyed or damaged.

5.2.2 A landscape made of cells

In the cellular automata model, the landscape is considered composed of square cells. Many cellular automata models for plant dynamics use a cell size that matches the average crown size of adult individuals (Marco *et al.*, 2002; Nehrbass *et al.*, 2007; Scanlon *et al.*, 2007). That choice leads to two possible cell states: empty (0) or occupied (1). In contrast, this study focused on a larger scale, so that

Table 5.1: Values for parameters used in the metapopulation model and their meaning. Reasons for these values are provided in the text.

Symbol	Description	Saltcedar	Mesquite
K	cell carrying capacity	40	50
u	annual seed production per plant	500000	10000
r_{SD}	short-distance dispersion range [m]	20	20
r_{LD}	long-distance dispersion range [m]	1000	500
f_{LD}	fraction of long-distance dispersed seeds	0.1	0.1
p_{LD}	probability of long-distance dispersion	0.1	0.1
p_g	probability of seed germination	0.4	0.6
p_s	probability of seedling establishment	0.1	0.5
q	probability of juvenile survival	0.1	1
$a_{\max}$	mean maximum longevity [years]	80	50
a_{mat}	age of reproductive maturity [years]	2	5

many individuals can inhabit a single cell and the state of the cell at any time corresponds to the population of each species within the boundaries of the cell. The cell size used here corresponds to the spatial resolution of Landsat imagery (30 by 30 meters), which is considered an independent dataset for parameter estimation. Cells are considered homogeneous across its extent, so that no spatial preference of individuals within the cell can be attributed. Each cell has a spatial location associated, which is defined by the center of the cell. Cells' carrying capacity in absence of competition are held constant. The carrying capacity defines the maximum number of sites that can be colonized by each species within each cell. Site occupancy and individual extinction occur randomly, but no colonization is allowed to occur outside the boundaries of the cells grid. Occupied sites can either remain occupied or become empty and empty sites can either remain empty or become occupied at each time step, but no multiple change operations are allowed in a single time step. Thus, if an individual dies at one time

step, its site is not made available for colonization until the next time step. Yet, a site can be colonized by the two species simultaneously, but one may be excluded by competition at a later time.

5.2.3   Population dynamics: The transition rules

The transition rules considered here are stochastic in nature and correspond directly with the colonization and extinction rates on an annual basis (i.e., a time step is a year). For the time being, let us assume that the probabilities of colonization and extinction are known at each time step. Then, the simulation model is expressed in pseudo-code as follows:

```
for each time step t,
  for each cell j,
    for each species x,
      i. get colonization and extinction probabilities: cx, ex;
      ii. with probability ex,
          drive to extinction individuals of species x;
      iii. with probability cx,
          colonize available sites for species x;
```

The concept of species competition is incorporated at the level of site availability. More specifically, let X_t and Y_t denote the densities of native and non-native species within a given cell at time t, respectively. In absence of competition, an empty cell can support up to K_x individuals of native species, and up to K_y individuals of invasive species. However, if species compete for resources

within the cell, (e.g., nutrients, sunlight, moisture, or, simply, space) then the capacity for each species will decrease in proportion to the density of the competitor. Therefore, at each time step, the number of sites available for colonization for each species are given by $K_x - X_t - \alpha_x Y_t$ and $K_y - Y_t - \alpha_y X_t$, respectively, where α_x and α_y are termed the *interspecific competition coefficients*. The interspecific competition coefficients represent the effects that the presence of each species has on the habitat of the other[1]. Considering the available space for each species, the stochastic transition rules can be approximated by the following deterministic dynamical equations at each cell:

$$X_{t+1} = X_t + c_x(K_x - X_t - \alpha_x Y_t) - e_x X_t$$

$$Y_{t+1} = Y_t + c_y(K_y - \alpha_y X_t - Y_t) - e_y Y_t \qquad (5.1)$$

where the second and third terms in the righthand side of each equation correspond to the mean field approximations of the colonization and extinction rates, respectively. This competition model resembles the classical Lotka-Volterra competition model (Vandermeer and Goldberg, 2003), but in a discrete domain. Noticeably, the competition interactions in this model have a symmetric structure affecting directly the rate of colonization of competing species. Empirical evidence has shown that some competitive interactions also influence the death rate, but are age-dependent. Specifically, saltcedar survival during the first few years of establishment is sensitive to the density of native species, whereas the survival of the native is not directly affected by the density of saltcedar (Sher *et al.*, 2002).

---

[1]Note that the effect that each species has on itself, the intra-specific competition coefficient, is the unit.

Unfortunately, it is not clear how these competition interactions take place above and below the ground and, hence, are not considered in the model. Nonetheless, the differences in demographic and life history traits should reflect the competitive superiority of one species or another. The simulation model above is further specified through models for the colonization and extinction probabilities given in terms of species demographic and live history traits. These models yield space- and time-varying colonization and extinction rates.

5.2.3.1 Age-dependent extinction

In each year, an individual at age a dies with a probability $e(a)$ and survives with probability $s(a) = 1 - e(a)$. The annual survival probability $P_s(a)$ is related to the longevity $a_{\max}$ and the survival during the first year q through a truncated geometrical distribution for the probability of dying at age a, in such a way that $P_s(1) = q$ and $P_s(a) = 0$ for $a \geq a_{\max}$ (see Section III.3 in the Appendix III). A linearity constraint imposed on $e(a)$ allows using the average age per cell in place of individuals' ages. More specifically, each year any individual die with probability $e(\bar{a}_t)$, where $\bar{a}_t$ is the cells' average age at time t. The average age is estimated using the recursive formula (see Appendix III, Section III.3 for further details):

$$\bar{a}_t = 1 + \left(1 - \frac{C_{t-1}}{X_t}\right)(\bar{a}_{t-1} - b) - b\frac{E_{t-1}}{X_t} \tag{5.2}$$

where C_{t-1} and E_{t-1} denote the colonization and extinction rates in the previous year and $b = q\sigma^2/(a_{\max} - 1)$, where σ^2 is the variance of the truncated geometric distribution.

5.2.3.2   Colonization by seed dispersal

Colonization of a site occurs when at least one seed germinates and survives the seedling stage. If p_g denotes the mean germination probability of the species and p_s denotes the probability that a seedling survives the establishment stage, then the colonization probability can be determined, assuming statistical independence of the two events as (Marco *et al.*, 2002):

$$c_j = 1 - (1 - p_s p_g)^{S_j/K} \tag{5.3}$$

where S_j is the total number of seeds at cell j, K is the number of habitable sites per cell and hence S_j/K is the average seeds per site.

Seeds are produced by mature trees and dispersed isotropically around the parent tree. Most of seeds will settle around the parent's range (short-distance dispersal or SDD), while a minor fraction of seeds undergo long-distance dispersal (LDD) by wind (saltcedar) or animals (mesquite). To account for both SDD and LDD, the model builds upon prior formulations of a stratified diffusion model (Hengeveld, 1989; Kawasaki *et al.*, 2006). According to the stratified diffusion model, the species extents its range concentrically at a constant speed by SDD, while at the same time producing LDD of seeds to create nuclei of new colonies at distance well separated from their parents. The total number of seeds S_j received by the cell j from individuals located at cell i is given by:

$$S_j = \sum_i u M_i f(d_{ij}) \tag{5.4}$$

where u is the mean number of seeds produced per plant, M_i is the population in the reproductive maturity age at cell i, d_{ij} is the distance between cells i and j,

and f is a dispersal distribution function defined as a negative exponential function of the form $2\exp(-2d/r)/\pi r^2$, where parameters r's are selected according to the dispersion range for each species and type of dispersion (Table 5.1). While all cells can experience SDD with dispersion range r_{SD}, LDD can take place with probability p_{LD}. Sites selected for LDD are convolved with a second negative exponential term with dispersion range r_{LD}. This process simulates a fat-tail distribution typically found in seed dispersal models (Katul *et al.*, 2005). The convolution operation of Equation (5.4) is limited to a 3-by-3 neighborhood for SDD, and to a 21-by-21 neighborhood for LDD. The population in the reproductive maturity age at time t is approximately determined by applying the expected survival rate to past colonization terms. This is expressed in Equation (5.5) (see Section III.4 of Appendix III for further details).

$$M_t = X_t - \sum_{a=1}^{a_{\text{mat}}-1} P_s(a-1)C_{t-a} \tag{5.5}$$

This formula requires up to $a_{\text{mat}} - 1$ past colonization terms which are saved during the simulation, and are assumed null for the first a_{mat} iterations.

Figure 5.1 shows the progression of a simulated front of saltcedar population due to both SDD and LDD. Partial occupancy of the cell is apparent from the smooth transition between black and white tones. Note that patchy distribution appears only at distant locations ahead of the contiguous distributed range.
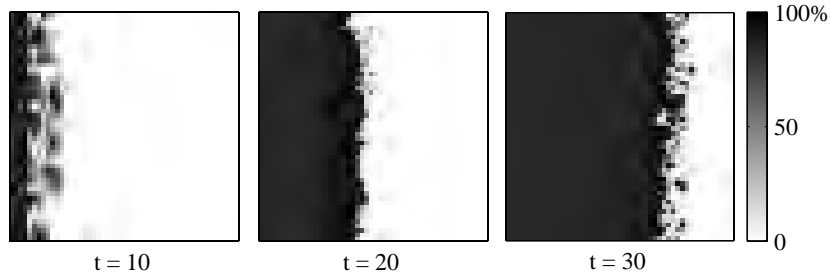
Figure 5.1: Progression of saltcedar expansion due to both short- and long-distance seed dispersal at three time points $t = 20$, $t = 25$, $t = 30$. The gray scale represents the percent of sites covered within each cell.

5.2.3.3 Verification of the extinction and colonization models

In order to assess the impact that the approximations of the average age and the population in the reproductive maturity have on the estimation of the population density, the metapopulation model was compared with a model that tracks individual ages to maintain the age structure. Since the latter demands more memory and computing time, only one single cell (with internal colonization only) was simulated in both cases. The two models were run independently, but using the same parameters as given in Table 5.1, and $\alpha_x = K_x/K_y$ and $\alpha_y = K_y/K_x$. Note that because the models are stochastic in nature, the outcomes vary between runs even with the same initial conditions. Figure 5.2.3.3 shows the outcomes of the two models from one single run in the form of scatterplots, where the horizontal axes (actual) correspond to the model with age structure, and the vertical axes (estimated) correspond to the model based on averages. Although multiple simulations showed varying deviations in estimated average ages and
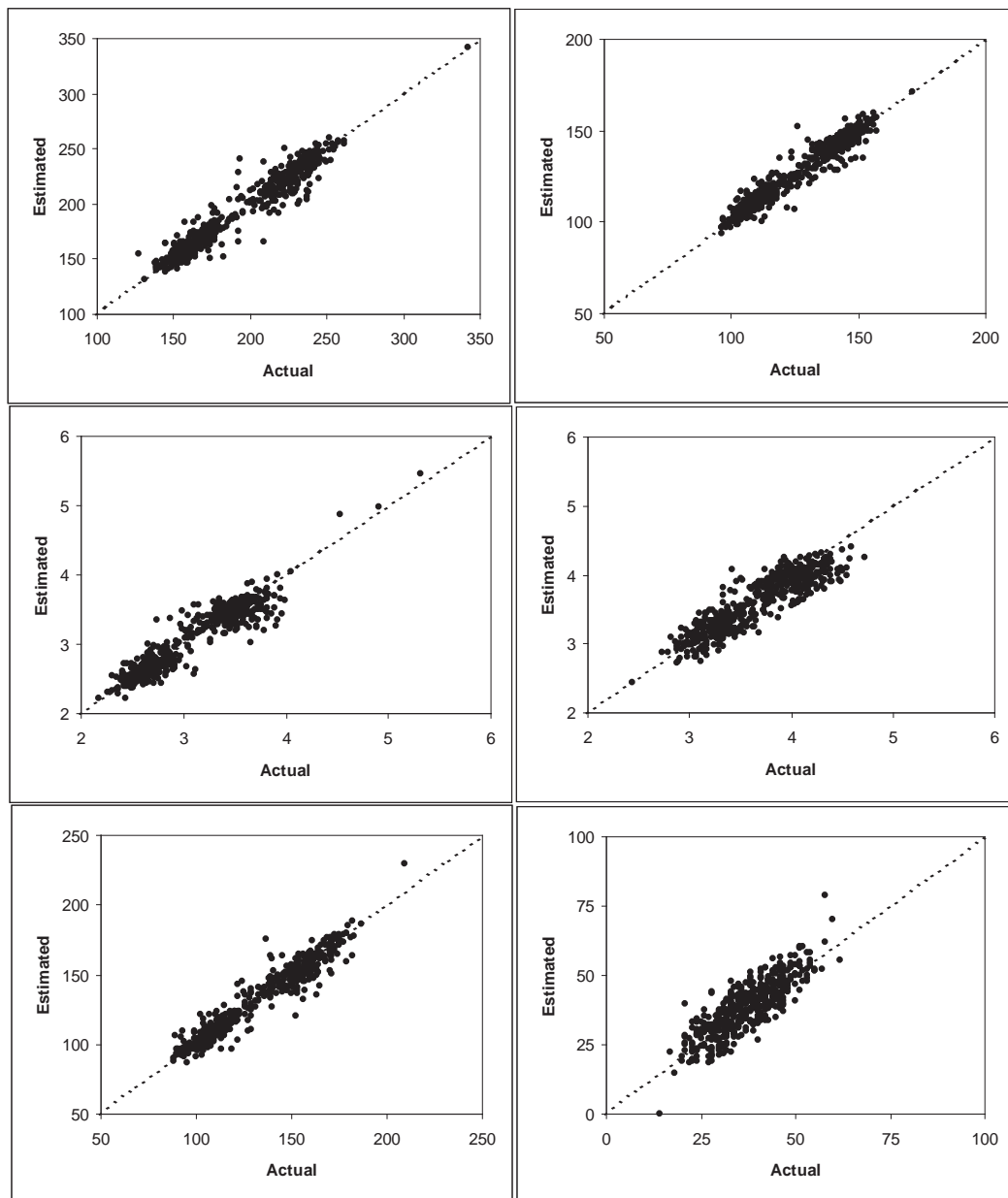
Figure 5.2: Comparison between a simulation based on the age-structure (actual) and a simulation based on average age and expected survival (estimated). Values correspond to population density (top row), average age (middle row) and population in the reproductive maturity age (bottom row) for saltcedar (left column) and mesquite (right column) populations.

mature population from actual values, they generally yielded estimated population density with high R-square values ($R^2 > 0.9$). Furthermore, observations from the multiple simulations confirmed that the estimations are unbiased for a range of parameter values.

5.3 COEXOD: A spatially explicit land cover change model

A land cover change counterpart of the above spatially explicit metapopulation model can be derived by linking the mean field approximation of Equation (5.1) to a three-state markov model of site state transitions, provided that the normalized densities can be treated as probabilities and the following conditions of the underlying dynamics are met:

1. the displacement of species occur either through clearing of sites or through competitive interactions at jointly occupied sites,

2. the persistence of jointly occupied sites is negatively impacted by competitive interactions,

3. at jointly occupied sites, only one species is visible from above, that is the canopy-dominant species,

4. the species that first colonizes an empty site becomes canopy-dominant for all its lifespan,

5. if simultaneous colonizations of a site occur, then the canopy-dominant species is determined by a *dominance probability* (δ),

6. the canopy-dominant species can affect the understory species through competitive interactions, but the latter cannot affect the former, and

7. the probabilities that one species occludes the other given that is being observed from above, i.e., the *occlusion probabilities* (λ_x and λ_y), are known.

Although these conditions may not reflect the complexity of real life, they are convenient to keep the model simple and yet capture some empirical knowledge about the competition process. This model is termed the COEXOD model because it is parameterized in terms of species COlonization and EXtinction probabilities, as well as in terms of canopy Occlusion and Dominance, and because it alludes an appropriate model description: 'species COEXistance as seen from the OverheaD'. The derivation of the transition probabilities undergoes three mayor stages each of which produces a markov model with four, five and three states, respectively (Figure 5.3). Description of each model follows.

5.3.1 Four-states markov model

Considering four states, at each time step (years) each site can be: occupied by native species alone (x), occupied by invasive species alone (y), occupied by both species simultaneously (z), or empty (w) (Figure 5.3(a)). Then, the transition among the four states is specified by a fourth-order transition probability matrix (TPM), which is derived from the following normalized version of Equation (5.1):

$$\tilde{X}_{t+1} = s_x \tilde{X}_t + c_x(1 - \tilde{X}_t - \gamma_x \tilde{Y}_t)$$

$$\tilde{Y}_{t+1} = s_y \tilde{Y}_t + c_x(1 - \tilde{Y}_t - \gamma_y \tilde{X}_t) \tag{5.6}$$
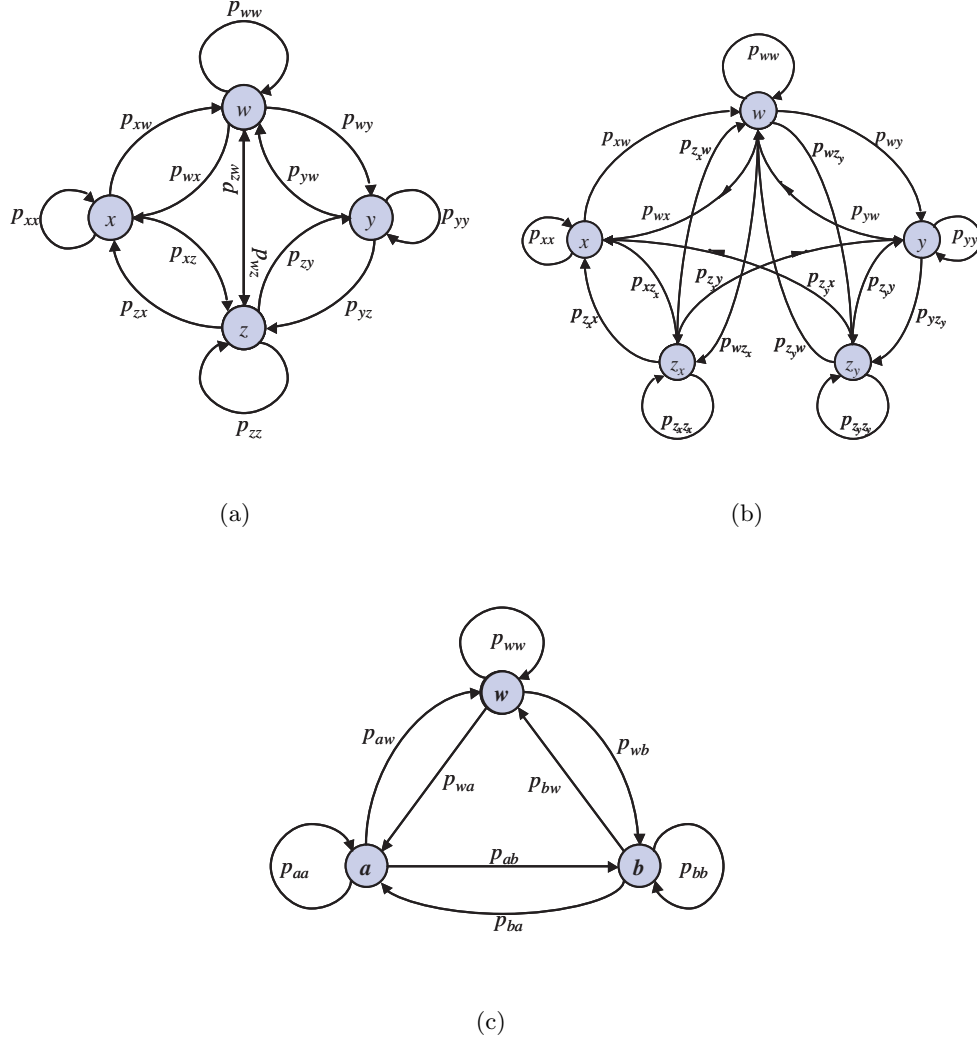
Figure 5.3: Markovian state transitions of the COEXOD model. Four-state markov model (a), five-state markov model (b) and three-state markov model (c). State labels correspond to: x = site is occupied by native species alone, y = site is occupied by invasive species alone, $z = z_x + z_y$ = site is simultaneously occupied by both species, z_x = site is jointly occupied, but the native species is canopy-dominant, z_y = site is jointly occupied, but the invasive species is canopy-dominant, w = site is not occupied at all, $a = x + z_x$ = site is covered by native species as seen from above, and $b = y + z_y$ = site is covered by invasive species as seen from above. See Table 5.2 for the transition probabilities.

Table 5.2: Transition probability matrices for the four-state markov model (a), five-state markov model (b), and three-state markov model (c). See text for explanation of parameters.

From \ To	x	y	z	w
x	$s_x - (1-\gamma_y)c_y$	0	$(1-\gamma_y)c_y$	e_x
y	0	$s_y - (1-\gamma_x)c_x$	$(1-\gamma_x)c_x$	e_y
z	$s_xe_y + \gamma_yc_y$	$e_xs_y + \gamma_xc_x$	$s_xs_y - \gamma_xc_x - \gamma_yc_y$	e_xe_y
w	$c_x(1-c_y)$	$(1-c_x)c_y$	c_xc_y	$(1-c_x)(1-c_y)$

(a)

From \ To	x	y	z_x	z_y	w
x	$s_x - (1-\gamma_y)c_y$	0	$(1-\gamma_y)c_y$	0	e_x
y	0	$(s_y - (1-\gamma_x)c_x)$	0	$(1-\gamma_x)c_x$	e_y
z_x	$s_xe_y + \gamma_yc_y/\delta$	e_xs_y	$s_xs_y - \gamma_yc_y/\delta$	0	e_xe_y
z_y	s_xe_y	$e_xs_y + \gamma_xc_x/(1-\delta)$	0	$s_xs_y - \gamma_xc_x/(1-\delta)$	e_xe_y
w	$c_x(1-c_y)$	$(1-c_x)c_y$	δc_xc_y	$(1-\delta)c_xc_y$	$(1-c_x)(1-c_y)$

(b)

From \ To	a	b	w
a	$1 - e_x$	$\lambda_xe_x(1-e_y)$	$(1-\lambda_x)e_x + \lambda_xe_xe_y$
b	$\lambda_y(1-e_x)e_y$	$1 - e_y$	$(1-\lambda_y)e_y + \lambda_ye_xe_y$
w	$c_x(1-(1-\delta)c_y)$	$c_y(1-\delta c_x)$	$(1-c_x)(1-c_y)$

(c)

where $\tilde{X}_t = X_t/K_x$ and $\tilde{Y}_t = Y_t/K_y$ are fractional abundances and $\gamma_x = \alpha_x K_y/K_x$ and $\gamma_y = \alpha_y K_x/K_y$ are the normalized interspecific competition coefficients. The idea here is to express the normalized densities in terms of the fraction of sites occupied by native species alone, sites occupied by invasive species alone, sites occupied by both species simultaneously, and the fraction of empty sites. The algebraic manipulation of these equations is guided by the two first conditions listed above. The condition 1 implies that a site occupied by one species alone at one time cannot be occupied by the other species alone the next time step, and thus the probabilities defining these transitions equal zero. The condition 2 requires that the transition probability defining the persistence of jointly occupied sites have the interspecific competition coefficients as a negative term. The TPM for the four-state markov model is expressed in terms of extinction probabilities (e_x, e_y), colonization probabilities (c_x, c_y) and normalized interspecific competition coefficients (γ_x, γ_y), as given in Table 5.2(a). Details on the derivation of the four-state markov model are provided in Section III.5 of Appendix III.

5.3.2 Five-states markov model

In a second stage, the proportion of jointly occupied sites (z) is split in two proportions $(z_x + z_y)$ yielding a five-state markov model (Figure 5.3(b)). The splitting assumes that only one species can be visible from above (condition 3). That species is termed the *canopy-dominant species*. Furthermore, the splitting applies the conditions 4-6 above. The condition 4 implies that the probabilities of change from canopy-dominant native species into canopy-dominant invasive

species, and the reverse change direction, are zero. The condition 5 states that, if the two species arrive to the site at the same time, then the probability that the native species dominates the canopy is $\delta_x = \delta$, whereas the probability that the invasive species dominates the canopy is $\delta_y = 1 - \delta$. The condition 6 states that the canopy-dominant species has a direct effect on the abundance of the understory specie, but the latter has no directs effect on the abundance of the canopy-dominant species. Thus, for example, the change from canopy-dominant native species into invasive species alone is not attributable to the presence of the understory species, but rather to the intrinsic extinction rate of the native species. Therefore, the interspecific competition coefficients do not appear in these type of changes (see Table 5.2(b)). Details on the derivation of the five-state model are available in the Section III.5 of Appendix III.

To further make sense of the role of the interspecific competition in jointly colonized sites, consider the third and fourth columns of Table 5.2(b). The colonization rate of a colonizing species in presence of the other already established is given by the non-zero entries at (row,column)=(x, z_x) and (y, z_y). These terms become negligible if the effect of the established species on the colonizing species is significant (i.e., the γ parameter approaches one). Likewise, the joint survival rate of simultaneously occupied sites is given by the entries at (z_x, z_x) and (z_y, z_y). These correspond to the intrinsic joint survival, but decreased in proportion to the effect that the canopy-dominating species has on the understory. The last row at the intersection with the third and fourth column correspond to the colonization rates for each species assemblage.

5.3.3 Three-states markov model

In the last step, the five-states model above is reduced to a three-states model (Figure 5.3c) by merging the states with similar above-canopy coverage, i.e., the fraction of sites with canopy-dominant native species (z_x) is added to the fraction of sites with native species alone (x), and the fraction of sites with canopy-dominant invasive species (z_y) is added to the fraction of sites with invasive species alone (y). Then, sites can be at one of three states: covered by native species (a), covered by invasive species (b) or not covered at all (w). As with the previous model, this model assumes that only the canopy-dominant species is visible from above. The merging is carried out by evaluating the conditional probabilities of observing a land cover at a given time step given the observed land cover at previous time step and considering the condition 7, that requires knowing the occlusion probabilities. The occlusion probabilities represent the ratio between jointly occupied sites for each canopy-dominant species relative to the proportion of sites with same above-canopy cover. The TPM associated with this model is given in Table 5.2(c) and the details of its derivation are provided in Section III.5 of Appendix III.

Note that since the effect of the interspecific competition has been isolated within changes between merged states, they do not seem to play a role in driving the dynamics as observed from above. Nonetheless, the occlusion probabilities are not independent from the interspecific competition, as the latter are somehow absorbed in the definition of the former. Both occlusion and dominance probabilities have been expressed as ratios between pairs of fractional densities,

which are in turn defined in terms of the interspecific competition coefficients. Although the time-dependency has been obviated in the notation, it is important to keep in mind that both dominance and occlusion probabilities are time-dependent. Moreover, these parameters are related through:

$$\delta = \frac{a\lambda_x}{a\lambda_x + b\lambda_y} \tag{5.7}$$

where a and b are the prior fractional densities of native and invasive species, respectively, as seen from above.

5.3.4 Estimating population parameters from remote sensing

If a linear relationship exists between species density and land cover area, then the fractional densities delivered by the COEXOD model correspond to the proportion of canopy coverage within each cell. Such information matches perfectly with the sub-pixel canopy cover as derived from remote sensing (where cells are matched to image pixel). Fortunately, the number of independent matrix entries in the model equals the number of parameters, thus allowing a stable inversion of the model. That is because each row of the TPM sums to exactly one, letting only six independent equations. This number of independent equations equals the number of independent parameters ($c_x, c_y, e_x, e_y, \lambda_x$ and λ_y, while δ can be determined through Equation 5.7). Nonetheless, the analytic inversion of the model is somewhat complex. Because of this, a numeric solution based on the least square estimation was implemented here. The entire process can be summarized as follows:

1. Produce sub-pixel classifications from images acquired at two dates (ideally, one year apart) using the TLSU classification method described in Chapter 3,

2. Define homogeneous regions, i.e., connected cells with similar dynamics, across the entire study area,

3. For each homogeneous patch, estimate a TPM using the sub-pixel change matrix described in Chapter 4,

4. For each pixel, estimate the parameters of the 3-state markov model by minimizing the euclidian norm between land cover fractions predicted from the estimated TPM and from the model TPM.

Once the COEXOD model parameters have been determined, the various population terms can be computed as indicated in Table 5.3. The formulas given in Table 5.3 correspond to expected values and should be treated as mere estimations of species population (up to a proportionality constant, namely the carrying capacity) under the premise that the land cover dynamics matches with the COEXOD model. What these formula say is that the key parameters for relating land cover to abundance are the occlusion probabilities. This result agrees with the intuitive reasoning that if occlusion is low, then land cover is a good estimator of abundance, but if occlusion is high, then land cover will generally underestimate the abundance.

Although the interspecific competition cannot be directly estimated using the COEXOD model, one can use the time series of estimated colonization, extinction, and species densities, to determine these parameters. Specifically, since

Table 5.3: Population density from land cover. a and b denote land cover fractions of native species and invasive species, respectively; and λ_x and λ_y denote the occlusion probabilities for native and invasive species, respectively. The time-dependency of fractional abundance and probabilities have been eliminated to simplify notation.

Cell fractional abundance	Formula
Native species alone	$(1 - \lambda_x)a$
Invasive species alone	$(1 - \lambda_y)b$
Canopy-dominant native sp.	$\lambda_x a$
Canopy-dominant invasive sp.	$\lambda_y b$
Jointly occupied sites	$\lambda_x a + \lambda_y b$
Native sp.	$a + \lambda_y b$
Invasive sp.	$b + \lambda_x a$

the time series should follow a dynamics as described by the system of

Equations (5.6), it suffices to apply a regressive approach to determine the two

constants γ_x and γ_y.

5.4   Results

5.4.1   Population parameters for the invasion in West Texas

The study site and data used in this test has been introduced in a

Chapter 4 and will not be further described here. The total fractional abundance

was estimated for the study site within the period from 1993 to 2005. As described

in Section 5.3.4, the parameters were estimated on a per-pixel basis and the

fractional abundance was based on estimated occlusion probabilities. The

homogeneous regions were produced by applying an unsupervised clustering

method on three stacked layers consisting of terrain slope, terrain elevation and

distance to the main channel of the river, and then connected segments were

labelled as unique homogeneous regions. One TPM was then estimated for each

homogenous region. Because the estimation of the TPM required a relatively large sample, regions with less than 10 pixels were clumped to one contiguous region. Also, since the images used here were acquired more than one year apart (1993, 1996, 2000, 2003 and 2005), the k-th power of the model TPM, with k equal to the number of years between two consecutively acquisition years, was fitted to estimated multiple year TPM. This assumes that the model parameters did not change between the initial and final years. Because the later assumption cannot be warranted, the estimated parameters should be considered as affective values within a time period.

The total fractional abundance (summed over all pixels of the study area) is plotted as a time series in Figure 5.4(a) and its relation with the area covered is shown as a scatterplot in Figure 5.4(b). Both area and abundance are computed from estimated transition probability matrices, the difference being in that the former is based on a parameterized model and the latter is not (see Figure 4.6 in Chapter 4 for the time series of land cover areas). Note that the relationship between abundance and area is strongly linear for both species. The extremely higher abundance noted as a big jump in year 2004 in the time series and as outliers in the scatterplots of Figure 5.4 called for special attention. At this year, extreme precipitation occurred (see Figure 4.2 in Chapter 4) which may explain the extremely higher species abundance. Indeed, the correlation between average precipitation and species abundance was statistically significant ($R^2 = 0.75$ for saltcedar and $R^2 = 0.67$ for native species), whereas the correlation between area covered with precipitation was not ($R^2 = 0.009$ for saltcedar and $R^2 = 0.005$ for

native species). Although it is reasonable to think that the incipient vegetation during this rainy year might have been mostly present under the canopy of existing vegetation, the time series for the occluded population (see lower lines shown in Figure 5.4(a)) tells us a slightly different story. These curves reveal that while a great portion of the increase in native population during 2004 was located under the canopy of saltcedar (note the increase of the occluded native population), the significant increase of saltcedar population was not found under the canopy of native species (note that there is no increase in the occluded saltcedar population). This is reasonable, considering that unlike native willow or mesquite species, saltcedar seedling have more chance to survive without competition (Sher *et al.*, 2002). Then, why is this conspicuous change during 2004 not apparent in the covered area? The explanation to this is because the model used to generate the fractional cover considered a spatially-aggregated TPM, which does captures the spatial variability that may be driven by precipitation patterns, and which is capture by the COEXOD model.

That species abundance increases with precipitation is not surprising, specially knowing that both species relay on water availability for successful establishment and survival. However, there are worth noting differences between the two species. The differences between species is better visualized in terms the probability parameters. Figure 5.5 shows a subset of the spatial distribution of estimated probabilities for the time period 2003-2005. As revealed in this figure, there are not notable difference in terms of canopy dominance and occlusion probabilities, but there are notable differences in terms of colonization and
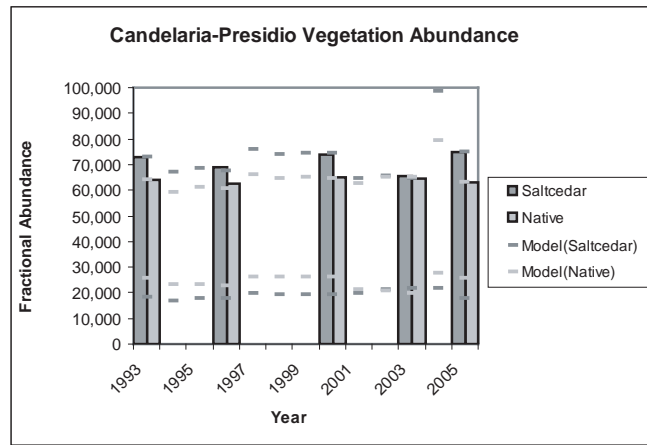
(a)
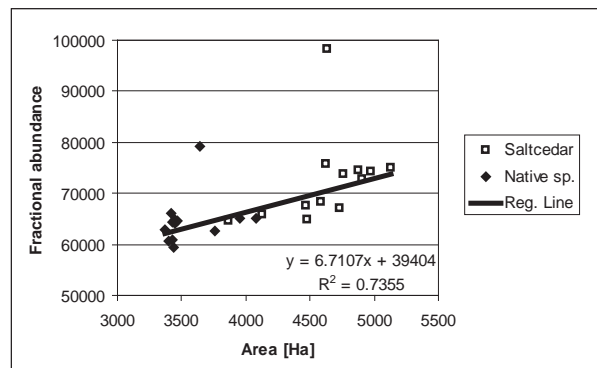
(b)

Figure 5.4: Fractional abundance time series (a) and area-abundance scatterplot. Abundance estimations were based on the COEXOD model whereas area estimations were based on a space-invariant transition probability matrix (see Chapter 4). The lower lines in (a) correspond to the occluded portions for each species, and the vertical bars corresponds to estimations coming from the sub-pixel classifications rather than from the model. The the regression line in (b) corresponds to the pooled data of both species, but without the outlier points of 2004.

extinction probabilities. These maps demonstrate the superiority of saltcedar in terms of colonization and extinction rates, specially along the river floodplain. The apparent higher colonization probability and lower extinction probability of saltcedar was also observed for all other time periods confirming that its superiority was not attributable to the availability of more water, but rather to the traits that enable it to reproduce profusely and to tolerate the environmental stress (Di Tomaso, 1998).

In order to provide an overall quantitative comparison of the two species, time-averaged probabilities were sampled at 1000 randomly selected points across the entire study site. Samples were then grouped in 25 classes according to percentiles of distance to main channel and averages computed for each group. Figure 5.6 shows the average probabilities as function of average distance to the river. As expected, saltcedar had the highest colonization probability and the lowest extinction probabilities for the entire distance range. Both species had indistinguishable occlusion probabilities, which suggests that saltcedar has similar chances to occlude the native in the understory than the native itself to occlude the understory saltcedar. Nonetheless, the probability that saltcedar dominates the canopy seems to be higher within the 150-meter bands along the river. This have been personally observed during several field trips to Candelaria during 2005-2006 (unpublished data) and by some studies showing that saltcedar typically outgrows the native species willows and mesquite trees along the riverbanks. The patterns of extinction and colonization shown in Figure 5.6 are also intuitive. Since nearer sites to the riverbanks are more likely to be flooded than farther sites,
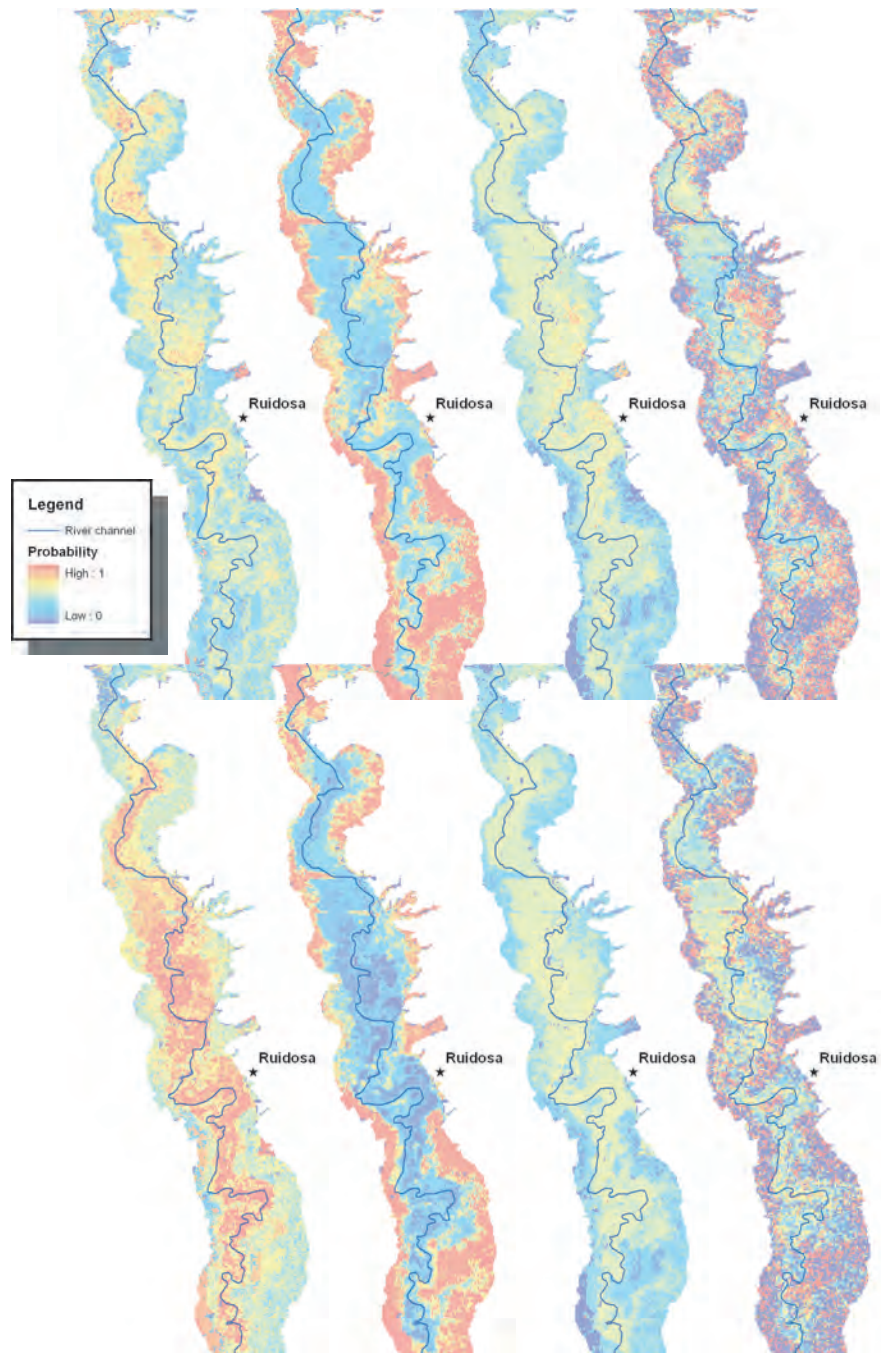
Figure 5.5: Color-stretched images of estimated probabilities of COEXOD model. The images correspond (from left to right) to colonization, extinction, occlusion and dominance probabilities for native species (top) and saltcedar (bottom). The subset of the study site is located around Ruidosa, Texas and the time period was 2003-2005.

it is reasonable to think that the colonization and extinctions rates will follow a similar pattern: increasing extinctions/decreasing colonization rates at farther distances from the river channel. Furthermore, the replication of the extinction pattern shown in Figure 5.6 through the metapopulation model would require increasing average age for increasing distance to the river channel. This requirement is in agreement with observed age structure of saltcedar and cottonwood in the San Pedro River in Arizona (Stromberg, 1998), where the increasing stand age corresponds to increasing groundwater depths, and thus to increasing distance from the river channel.

5.4.2 Test of invasion under competition

There is an active and ongoing debate as to when saltcedar can replace native plants and if it is actively displacing native plants or it is just taking advantage of disturbance by removal of natives by humans and changes in flood regimes (Everitt, 1998; Pratt and Black, 2006; Sher *et al.*, 2002). Research on competition between saltcedar seedlings and co-occurring native trees has found that the seedlings are not competitive over a range of environments (Sher *et al.*, 2002; Young *et al.*, 2004). However, once established, saltcedar monopolizes the space and displaces the native species. This issue was investigated here by means of the metapopulation model. The objective was to determine if saltcedar invades by virtue of its competitive effect on the established native species or by the lack of an effect on it by the native species.

More specifically, an experiment was designed to test the effect of
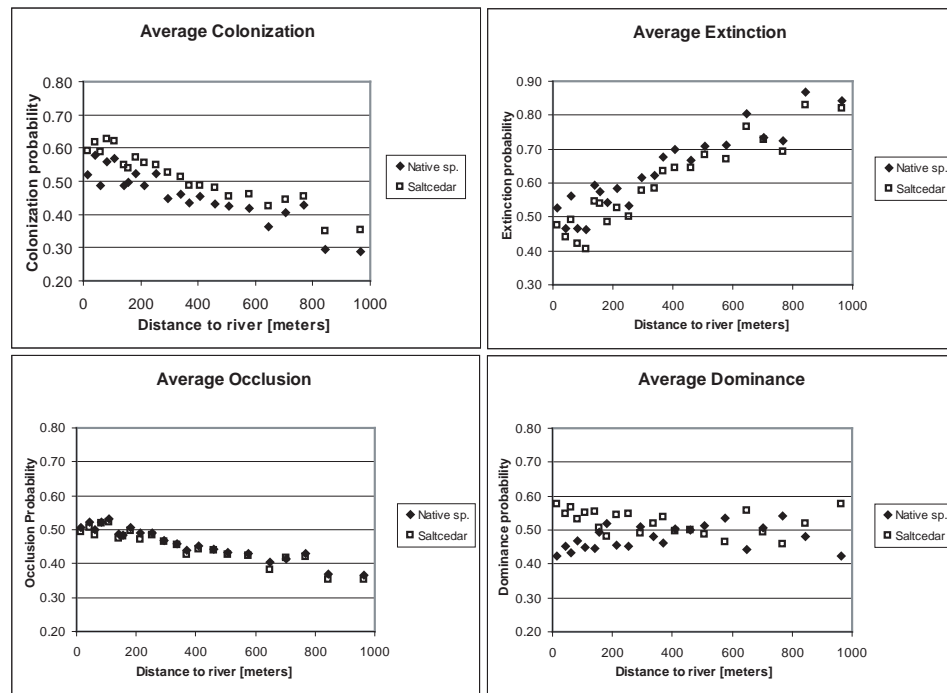
Figure 5.6: Time-averaged colonization, extinction, occlusion and dominance probabilities for the period 1993-2005 along a gradient of distance to the main channel of the river. Averages are based on 1000 points randomly selected across the entire study site, and grouped within 25 distance classes. The horizontal axis corresponds to the average distance in meters for each distance class.

competition levels of both saltcedar and mesquite on the invasion speed and steady average density. In all the tests, the invasion started from the leftmost column and expanded toward the rightmost column of the simulation grid. The invasion speed was estimated as the rate of change of an average front position (Marco *et al.*, 2002). The front position for each row of cells was determined as the position of the rightmost-cell that has been colonized by saltcedar, where cell's are considered colonized if the species's abundance is at least ten percent of its carrying capacity. The average front position is then determined by averaging over all rows (and over five simulations to reduce the effect of randomness).

The simulated invasion process considered the native species already established in the habitat. For this matter, a randomly distributed population of mesquite was evolved for 100 years in the absence of the invader. In that simulation the initial condition for the native species was randomly set to density values uniformly distributed between zero and one half the carrying capacity. The final distribution had an average abundance of 45.26 (std. = 2.08). The average age of the population was initially set to one year for all the cells and ended up around 6 years (std. = 0.5). After the 100-year period the invader was introduced at the left-most column of cells and the simulation was resumed for 200 years more. The initial density of the invader was randomly allocated from zero to a relatively low density (10 percent of its carrying capacity) at the leftmost cells and zero at all other cells. The invasion speed and the average abundance at the end of the simulation period were determined for three cases: 1) when only mesquite competes ($\gamma_x = 0, \gamma_y = \gamma$), 2) when only saltcedar competes ($\gamma_x = \gamma, \gamma_y = 0$) and 3)

when both species compete equally ($\gamma_x = \gamma$,$\gamma_y = \gamma$).

The results are shown in Figure 5.7. Two main observations from these results are that 1) saltcedar can invade (expand its range and grow in density) only if the native species compete bellow a coexistence threshold and 2) the competitive effect of saltcedar on the native species does not accelerate the invasion rate. Figure 5.7(c) shows that saltcedar's competition level has negligible effect on its invasion speed. In contrast, the effects of mesquite on saltcedar's invasion can be significant. The chance of saltcedar to expand its range decrease rapidly as the competition level of mesquite approach to a coexistance threshold (which seems to be around 0.6). No expansion was observed for competition levels of mesquite greater than the coexistence threshold during the 200-years period, and the invader was soon excluded by competition in most cases. Similar behavior was observed (data not shown) for several parameter combinations other than those shown in Table 5.1. Although some of these parameters are known to promote the speed of the invader, such as percent of seeds available for long-distance dispersion, the probability that a cell catch long-distance dispersed seeds and the dispersion range (Kawasaki *et al.*, 2006; Nehrbass *et al.*, 2007), when held constant with varying competition levels, the same conclusions were met.

5.5   Conclusions

A cellular automata-based metapopulation model was conveniently parameterized in terms of colonization probabilities, extinction probabilities and interspecific competition coefficients. This parameterization level allowed

(a)

(b)

(c)

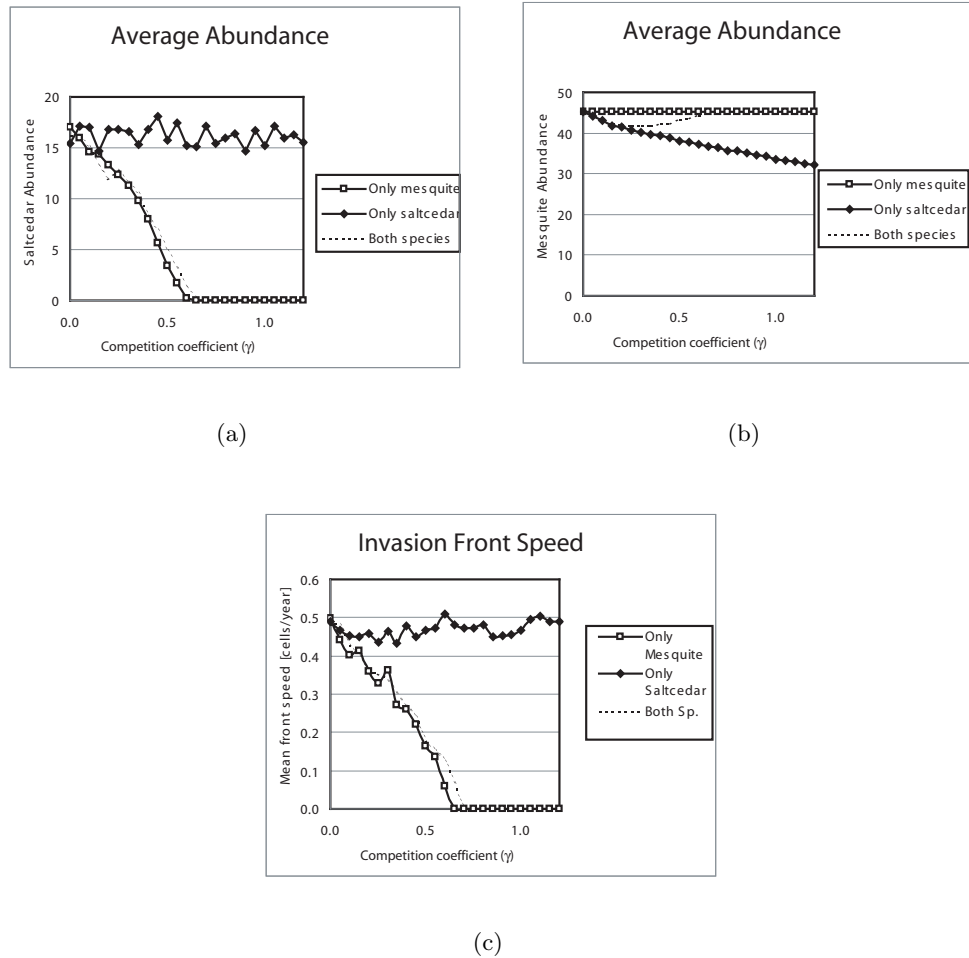Figure 5.7: Effects of competition level on saltcedar abundance (a), mesquite abundance (b), and invasion front speed (c) for three competition scenarios. The competition scenarios were defined as 1) only mesquite competes ($\gamma_x = 0, \gamma_y = \gamma$), 2) only saltcedar competes ($\gamma_x = \gamma, \gamma_y = 0$), and 3) both species compete equally ($\gamma_x = \gamma, \gamma_y = \gamma$).

incorporating relevant species traits and coupling moderate resolution remote sensing observations. The parameterization at the level of species traits yielded an age-dependent mortality model that only depends on the average age per cell, whereas the colonization probabilities incorporate a model of seed dispersal in which the average population in the reproductive maturity is estimated from expected survival rates. Both approximations were shown to lead to estimates that are comparable to those determined when the age structure is maintained. Although this detailed specification incorporated some of the species traits that are desirable for studying saltcedar invasion, it was at the level of extinction and colonization probabilities that remote sensing observations could be matched with the model parameters. Specifically, the metapopulation model was used to derive a model, termed the COEXOD model, that is more suitable for studying the dynamics from a remote sensing perspective. The COEXOD model is a spatially explicit model that prescribes the changes among site states in terms of transition probability matrices. The transition probabilities are derived from the metapopulation model and are parameterized in terms of species colonization and extinction probabilities as well as in term of canopy occlusion and dominance probabilities. The parameterization in terms of occlusion and dominance probabilities was a convenient way to express the competitive interaction as seen from the overhead.

The inversion of the COEXOD model through multi-temporal sub-pixel land cover change matrices showed interesting patterns of the saltcedar invasion in West Texas. First, the estimated abundance pattern confirmed the remarkable

influence of precipitation in driving the overall dynamics, thus illustrating one of the most cited paradigms in aridland ecology: Noy-Meir's 'pulse-reserve' conceptual model. The pulse-reserve model depicts a simple, direct relationship of plant growth with rainfall (Noy-Meir, 1974). As it appears, a pulse event of precipitation in 2004 triggered a pulse of plant growth that was most significant for saltcedar. The underlaying mechanism is now recognized to be much more complex and highly dependent on soil storage capabilities and plant functioning (Reynolds *et al.*, 2004; Schwinning *et al.*, 2004). Second, the estimated model parameters supported the superiority of saltcedar over the native mesquite and willow communities in terms of per-capita colonization and extinction rates, as well as in terms of canopy-dominance along the river banks. Third, the modelling approach enabled the estimation of abundance and distribution of saltcedar and native species (previously unavailable), which can be further analyzed for hypothesis formulation and/or for guiding the modelling at the level of extinction and colonization rates.

On the other hand, the metapopulation model was used to analyze the competitive effects on the speed of a virtual invasion. A simple experimental settings was used to measure the rate of advance of an invasion front in presence of an established species. Saltcedar invasion of a mesquite-dominated landscape was taken as a case study. Results from computer simulations indicate that saltcedar does not actively increase its dispersion speed over a wide range of competition levels. In contrast, the competition level of the native can slowdown the invasion process and, eventually, prevent it. Consistent with the coexistence principle of

ecology (Chesson, 2000), the model predicts that saltcedar can invade without competing, provided that the native species's intra-specific competition is more significant than its interspecific competition. It must be recognized that this finding may not extrapolate to the saltcedar invasion in West Texas, primarily because the experiment relies on fairly simple seed dispersal and extinction models. In the extinction model, individuals die only because they get older, but not because of a direct effect from competitive interactions (or from exogenous disturbances). Also, the seed dispersal model does not consider water and animal seed dispersal mechanisms which are important factors of invasion. Unfortunately, the relative proportions of seeds dispersed through wind, water and animals are unknown and difficult to measure in the field (Hedrick, 2005).

Chapter 6

DISCUSSION

6.1   Sub-pixel accuracy assessment

Determining land cover information accurately from remote sensing is crucial to understand several ecological and environmental processes occurring at a range of scales, such as saltcedar invasion. Since the spatial pattern of land cover information can be smaller than the sensor footprint, sub-pixel classifications offer a flexible way to infer sub-pixel land cover information. However, accuracy assessment of these representations has been recognized to be far more difficult than traditional crisp classifications (Foody, 2002). A great variety of measures derived from the traditional error matrix exists for describing the accuracy of crisp classifications (Congalton, 1991; Congalton and Green, 1999; Stehman and Czaplewski, 1998). However, this method is appropriate only for hard classification, where it is assumed that each pixel is associated with only one class in both the assessed and the reference datasets. For sub-pixel classifications, where multiple classes are assigned to a single pixel, a comparable standardized assessment procedure has not been established yet. The main contribution in sub-pixel accuracy assessment (Chapter 2) were: 1) a thorough review of existing methods for accuracy assessment of sub-pixel classifications, and 2) the development of a more ontologically-grounded cross-tabulation matrix that accounts for the sub-pixel distribution uncertainty.

145

For the cross-comparison report to be useful for identifying a perfect match between the reference and assessed data, it was necessary to constrain the agreement measure at the pixel level. Even though, it was shown that there is no analytical way to determine uniquely the actual confusion based solely on the information of land cover fractions. This problem was termed the sub-pixel area allocation problem. In this context, it was shown how a previously recommended composite operator (Pontius Jr and Cheuk, 2006) provides one of (possibly) infinite number of solutions to the sub-pixel area allocation problem. This solution corresponds to the expected sub-pixel class overlap constrained to the unmatched sub-pixel fraction. Two new composite operators were introduced to provide the minimum and maximum possible sub-pixel class overlap constrained to the unmatched sub-pixel fraction. The intervals defined by these operators are arranged within a matrix, in the form of a center value plus-minus its uncertainty, termed the sub-pixel confusion-uncertainty matrix (SCM). Furthermore, accuracy indices from the traditional confusion matrix were also generalized from the SCM to account for the sub-pixel distribution uncertainty.

It was shown that when at most one class is either under- or overestimated at each pixel the SCM results in the original composite matrix (Pontius Jr and Cheuk, 2006), meaning that no uncertainty arise on the interclass confusions. One typical instance of this occurs when at least one of the compared sets is crisp, as in the assessment of continental and global products through moderated resolution images (Latifovic and Olthof, 2004). In this case, crisp classification from coarse resolution images are assessed using fractions derived from moderate/high

resolution images. The cross-comparison of crisp- against soft-classified pixels also arises in the assessment of historical datasets for which ground-truth data is unavailable. In this case, the hardened version of a fuzzy classification can be assessed using the fuzzy values (Okeke and Karnieli, 2006). Another common instance of uncertainty-free matrices arises when the number of classes is less than four. This is also significant because many remote sensing methods for producing soft classifications, typically based on spectral mixing models, use three classes (end-members) to describe a wide variety of land cover characteristics (Carpenter *et al.*, 1999; Milton, 1999; Roberts *et al.*, 1993; Small, 2004). Bottom line, the SCM results in the traditional confusion matrix if both datasets are crisp, in which case, the generalized accuracy indices result in the traditional ones as well.

6.2   Sub-pixel mapping techniques

In the past, the poor classification accuracy obtained from Landsat-like sensors for species identification has been largely attributed to the sensor's spatial and spectral characteristics. However, since the theoretical bounds of the accuracy from such limitations are unknown, one should conjecture on the existence of more sophisticated methods that can improve over prior ones. Among other things, this study (Chapter 3) has tested the conjecture that the incorporation of some non-linear relationship arising from the light-canopy interaction can produce more accurate estimations of sub-pixel canopy cover. Moreover, several linear and non-linear spectral unmixing methods were tested for retrieval of saltcedar canopy cover to serve as a guidance for subsequent repetitive mapping tasks. The main

contribution of Chapter 3 is two fold: 1) the identification of a practical and accurate method for repetitive mapping of the canopy cover of invasive saltcedar and associated species, and 2) the elucidation on the practical implications of applying a physically-based model that accounts for the light-canopy interaction.

More specifically, results reported in Chapter 3 indicated that linear models can achieve low to moderate accuracy if properly constrained. Although the linear model can afford good predictions of mixed reflectance from Landsat, the relative contribution of end-members to the mixed reflectance does not accurately represent its areal coverage. It was shown that despite its physical basis and simple parameterization, a method that incorporates multiple-scattering processes (Huang *et al.*, 2007; Lewis and Disney, 2007; Smolander and Stenberg, 2005) has high requirements that cannot be met by multi-spectral Landsat data. Furthermore, while within-canopy end-members are essentially non-linearly mixed due to multiple scattering, MSA can only achieve low to moderate performance if used with above-canopy end-members, which are mostly linearly mixed (Roberts *et al.*, 1993). A piecewise linear unmixing method termed TLSU was implemented as a means of assessing to what extent the broadly defined end-members were a factor affecting the predicted species canopy cover from linear mixture models. The superior performance of TLSU over FCLSU demonstrated that the number and relative location of end-members within the cloud of mixed pixels might have been a major factor affecting the linear spectral unmixing results. Although lacking a physical basis, the TLSU method can be useful when the feature of interest cannot be described in terms of extreme points of the mixed pixel cloud,

such as green vegetation, soil/rock substrate, and dark surface/shadow (Small, 2004). Results also confirmed prior findings showing that backpropagation neural networks can outperform linear and other nonlinear methods (Atkinson *et al.*, 1997; Carpenter *et al.*, 1999; Liu and Wu, 2005), yet they require numerous training samples that are hard to collect in the field. Less obvious is the fact that a significant higher efficiency, in nearly a factor of 60, can be achieved with a well-sized BPNN over the best linear spectral unmixing method. This means that, for example, if one were to process an entire Landsat scene ($\sim$50M pixels), once the end-members have been determined and the network has been trained, BPNN5 would take around 42 minutes, whereas FCLSU would take around 41 hours to run on a conventional personal computer. Therefore, the simplicity of the LSM model, largely responsible for its popularity in the remote sensing community, is not necessarily translated into a more efficient method for repeatable sub-pixel mapping tasks. Further research should also consider time complexity analysis of unmixing methods for tackling regional and global environmental problems by means of remote sensing.

6.3 Sub-pixel change detection analysis of saltcedar invasion

Chapter 4 demonstrated the application of a sub-pixel change detection technique for vegetation change analysis of saltcedar invasion along the Rio Grande. A cross-tabulation matrix termed the sub-pixel change matrix (SChM) was adopted as the main change analysis tool because it provides full information on change directions. The SChM was used for estimating transition probabilities,

which were further correlated with a number of environmental factors known to influence the dynamics of riparian vegetation. The main contributions and findings from this study were: 1) a new method for sub-pixel change detection analysis, which provides full information on change direction, 2) disclose the relative merit of factors that have influenced species dynamics in the region, and 3) provide supporting evidence on the significantly higher impact of saltcedar abundance on river discharge as compared to native species abundance.

Contrary to suspicions, sub-pixel classifications of multi-temporal Landsat data acquired at five dates within the period 1993-2005 showed no continuous expansion of areas covered by saltcedar nor continuous reduction of areas covered by native species. Nonetheless, saltcedar dynamics appeared more sensitive to environmental fluctuations, confirming its ability to recover from droughts and periods of groundwater drop (Smith *et al.*, 1998). Simple correlations between estimated yearly transition probabilities with environmental data suggested that the most significant, yet somewhat redundant, determinants of changes occurred in the study area and period were the average annual precipitation, the average minimum temperature and maximum groundwater depth in the period.

Although saltcedar seems to be confined to relatively dry lands (Zavaleta and Royval, 2001), increasing precipitation in warm regions seems to stimulate the displacement of native vegetation by saltcedar and, at the same time, promote the colonization of bare exposed soil by either species. The issue is not simply that an increment of precipitation leads to an increment of changes from native into saltcedar. As a matter of fact, the reverse change direction is also stimulated by

increments in precipitation, but this type of change would occur more slowly. Therefore, the associated traits that enable saltcedar to grow faster under favorable conditions is what may be causing the displacement of the native vegetation. Closely related to the annual precipitation was the peak winter discharge (October-March). The extreme discharge during this season can promote more channel movement, vegetation scour, sediment reworking, and thus provides prolonged moisture essential to sustain seedlings and exposes competition-free seed beds for both the native and non-native species (Stromberg, 1998).

Likewise, although the minimum annual mean temperature correlates positively with saltcedar occurrence on a large scale (Friedman *et al.*, 2005), it negatively influences the displacement of native species by saltcedar. The mechanism is related to the maximum groundwater depth because at higher temperatures the water table drops due to high evapotranspiration rates. Under these stress condition, the dynamics of both native and non-native species appear to slowdown.

Interestingly, the discharge during the first year of the period was the only factor that correlated well with estimated transition probabilities from saltcedar land cover into native species land cover. This confirms that hydrologic regimes represent a unique equilibrating force that may aid both to maintain native species and control the proliferation of saltcedar (Busch and Smith, 1995; Stromberg, 1998). Furthermore, estimated mean maximum sub-pixel fractions and steady extinction probabilities grouped by percentiles of elevation, slope and distance to main channel showed that local capacity of saltcedar appear superior than local

capacity of native species under varying topographic conditions and confirmed the lower extinction rates respect to native species at increasing distances from the river channel, which is consistent with physiological traits that enable saltcedar to survive in the upland habitats (Di Tomaso, 1998).

Although not consistently increasing throughout the period, saltcedar extent was positively correlated with the loss of discharge in the region, confirming a long suspected significant impact in water availability of the region. In contrast, a relationship between the extent of native species and discharge loss could not be established. Although estimated water lost within the segment of the river does not take into account contributions from local storms or losses from surface evaporation and local irrigation, estimated consumption by saltcedar was consistent with field measurements (Cleverly *et al.*, 2002; Shafroth *et al.*, 2005). This is by no means a recommendation on how to estimate water consumption by saltcedar, but rather a demonstration where remote sensing observations coupled with a modelling approach are able to confirm suspected impacts on water availability.

The study presented here may be extended in many different directions. Further research should confirm the observed relations over larger study areas and longer periods. The incorporation of many more image acquisition dates with concurrent field observations would enable a more robust analysis. Unfortunately, field observations are rarely available for historical data and interpretations need to be guided by knowledge of phenomena in question. The approach presented here also opens the possibility for building models of transition probabilities that can

account for meaningful driving factors. Such models may be useful in forecasting invasion severity, assessing impact on ecosystems and supporting decision making.

6.4 Development of a metapopulation model for estimating population parameters from land cover change

In Chapter 5, a cellular automata-based metapopulation model to establish the links between remote sensing land cover change and the underlying population dynamics was described. The metapopulation model is an attempt to account explicitly for the main mechanisms suggested by previous works as involved in a plant invasion process (Higgins and Richarson, 1996; Marco *et al.*, 2002). The simulation approach was inspired in traditional metapopulation models (Gotelli, 2001, Ch.4). The original metapopulation model was extended in this dissertation to incorporate interspecific competition (Vandermeer and Goldberg, 2003). The linking process led to a land cover model termed the COEXOD model, which is a spatially explicit model based on land cover transition probabilities. Such probabilities are parameterized in terms of species colonization and extinction as well as canopy occlusion and dominance.

The inversion of the COEXOD model using remote sensing measurements for the saltcedar invasion in West Texas led to confirm the superiority of saltcedar in terms of per-capita colonization and extinction rates across a range of habitat characteristics dictated by the distance to the river channel, as well as in terms of canopy dominance along habitats located next to the banks of the river. The COEXOD model also enabled the estimation of spatially distributed abundance of saltcedar along the riparian corridor, which is hard to acquire otherwise. It can be

anticipated that such information will play a crucial role in understanding environmental fluctuations associated to species dynamics. For example, the remarkable influence of precipitation in driving the overall dynamics in such an arid environment was easily confirmed by the high correlation between estimated overall abundance and precipitation measurements.

On the other hand, the metapopulation model proved a reasonable means to analyze the effects of inter-specific competition on an invasion process. Simple experimental settings were used to measure the rate of advance of an invasion front in presence of an established species. Saltcedar invasion of a mesquite-dominated landscape was taken as a case study. Results from computer simulations indicated that saltcedar does not actively increase its dispersion speed over a wide range of competition levels. In contrast, the competition level of the native can slowdown the invasion process and, eventually, prevent it. Consistent with the coexistence principle of ecology (Chesson, 2000), the model predicts that saltcedar can invade without competing, provided that the native species's intra-specific competition is more significant than its interspecific competition. While habitat invasibility was determined by competitive levels of the native species rather than by traits of the invasive species, the persistence of the former is very much dependent on the levels of competition of the later. Prior work had shown that species' demographic traits and dispersal capabilities, such as long distance dispersal mechanism, have also a positive impact on the speed of invasion (Kawasaki *et al.*, 2006; Nehrbass *et al.*, 2007). A simple test where the percent of available seeds that can undergo long-distance dispersal (data not shown) by

random chance confirmed that, in effect, saltcedar's ability to colonize distant locations from its original range plays also an important role in its expansion.

Although these observations are largely based on a pure modelling approach, they should serve as a motivation to find out the relative importance of major driving factors in general invasion mechanism. This modelling approach could provide new insights into the debate as to when saltcedar can outcompete native plants and if it is actively displacing native plants or it is just taking advantage of disturbance by removal of natives by humans and changes in flood regimes (Everitt, 1998; Pratt and Black, 2006). Mechanisms of superior seedling establishment above- and bellow- ground of native species over saltcedar reveals that saltcedar is not a good competitor at the seedling stage (Sher *et al.*, 2002), yet it can displace a native species over time. The issue is complicated because the relative importance of competitive interactions is not well understood yet.

There were a number of parameters that were held constant in the model. Further research is needed to account for their relative importance for species invasiveness. Future research should also focus on the incorporation of factors of habitat invasibility. Specifically, identify what determines the susceptibility of a riparian habitat to the establishment and spread of saltcedar? Suggestions have been made that perfect timing between riverbank flooding and seed availability are the key factors in the successful establishment of saltcedar (Everitt, 1998; Warren and Turner, 1975). Preliminary results on simulated populations with varied survival probability across gradients of groundwater table depth revealed interesting patterns (data not shown) that might be useful for explaining, in future

work, the actual plant distribution as observed from remote sensing imagery.

Appendices

Appendix I

TIGHT CONFUSION INTERVALS

Consider the n-th reference and assessed pixels with membership values r_{nk} and s_{nk}, respectively, of belonging to class k, for $k = 1, ..., K$, where $K > 1$. If no class is underestimated nor overestimated, then there is a perfect match, and the proof for tight intervals is straightforward. The analysis when only one class is underestimated follows. Assume underestimation for class i at pixel n, so that $s_{ni} < r_{ni}$ and $s_{nk} \geq r_{nk}$ for $k \neq i$. The contributions to the diagonal elements, from both the MIN-LEAST and MIN-MIN operators, will be r_{nk}, at row $k \neq i$, and s_{ni}, at row i. Then, the contribution to the confusion intervals for columns $l \neq i$ becomes zero. Whereas the contributions to the lower and upper bounds of the confusion interval, at column i row $k \neq i$, become

$\max(s_{nk} - r_{nk}, 0) = s_{nk} - r_{nk}$ and $\min(s_{nk} - r_{nk}, r_{ni} - s_{ni}) = s_{nk} - r_{nk}$,

respectively. The latter equality can be concluded from the sum-to-unity constraint. Table I.1 shows the form of the contribution by the n-th pixel to both the upper and lower bounds of the matrix. A similar matrix can be obtained when only one class is overestimated, wherein only one row has non-null elements in the off-diagonal positions. Therefore, the confusion intervals are tight if at most one class is either overestimated or underestimated on a per-pixel basis.

Table I.1: Contribution of the n-th pixel to the upper and lower bounds of the confusion intervals for K classes, when only class i is overestimated.

Class	1	2	...	i	...	$K-1$	K	Row Tot.
1	r_{n1}	0	...	$s_{n1} - r_{n1}$	...	0	0	s_{n1}
2	0	r_{n2}	...	$s_{n2} - r_{n2}$	...	0	0	s_{n2}
$\vdots$	$\vdots$	$\vdots$	$\ddots$	$\vdots$	$\ddots$	$\vdots$	$\vdots$	$\vdots$
i	0	0	...	s_{ni}	...	0	0	s_{ni}
$\vdots$	$\vdots$	$\vdots$	$\ddots$	$\vdots$	$\ddots$	$\vdots$	0	$\vdots$
$K-1$	0	0	...	$s_{nK-1} - r_{nK-1}$	...	r_{nK-1}	0	s_{nK-1}
K	0	0	...	$s_{nK} - r_{nK}$	...	0	r_{nK}	s_{nK}
Col. Tot.	r_{n1}	r_{n2}	...	r_{ni}	...	r_{nK-1}	r_{nK}	1

Appendix II

MULTIPLE SCATTERING APPROXIMATION

Let z_j denote the proportion of light reflected from the jth end-member (or the output of the jth box in the diagram of Figure 3.4(b)), then

$$z_j = x_j \left(\alpha_j + \sum_{i=1}^{m} p_{ij} z_i \right) \tag{II.1}$$

where the first term in parenthesis corresponds to the proportion of light reflected directly and the second term corresponds to the proportion light that undergoes multiple scattering. This equation can be solved for the z's using matrix notation as follows:

$$\mathbf{z} = \mathbf{X} \left(\alpha + \mathbf{P}^T \mathbf{z} \right)$$

$$= \left(\mathbf{I} - \mathbf{X} \mathbf{P}^T \right)^{-1} \mathbf{X} \alpha$$

where $\mathbf{I}$ is the identity matrix of order m, $\mathbf{X} = \mathbf{diag}(x_1, \ldots, x_m)$ is a diagonal matrix of end-members spectra, and $\mathbf{P} = [p_{ij}]_{i,j=1,\ldots,m}$ is the matrix of re-collision probabilities. Furthermore, following the flow diagram of Figure 3.4(b), the MSA mixture model can be written as:

$$y = \sum_{j=1}^{m} z_j q_j$$

$$= \sum_{j=1}^{m} z_j \left(1 - \sum_{k=1}^{m} p_{jk} \right)$$

160

where q_j is the escaping probability from end-member j, i.e., the probability of no re-colliding. Using matrix notation, and replacing the expression for $\mathbf{z}$ above, results in

$$y = (\mathbf{1} - \mathbf{P1})^T \left(\mathbf{I} - \mathbf{XP}^T\right)^{-1} \mathbf{X}\alpha \qquad \text{(II.2)}$$

where $\mathbf{1}$ is a m-column vector of ones.

Appendix III

METAPOPULATION MODEL

III.1   Definitions and notation

For the dynamical analysis of the model, I consider here a generic cell to avoid indexing the cells. At each time t, $X_t = \sum_a X_{a,t}$ is the *population density*, expressed in terms of *age-structured population densities* $X_{a,t}$, i.e., the population density of the *a-age class* for each a; C_t is the *colonization rate*, i.e., the number of off-springs; $E_t = \sum_a E_{a,t}$ is the *extinction rate* expressed in term of *age-structured extinctions rates* $E_{a,t}$, i.e., number of dying individuals in the a-age class. Sums are over all ages, $a = 1, 2, \ldots$ By definition $X_{0,t} = 0$, for all t, and the zero-age class density is given by C_t. The *average age* at time t is defined as

$$\bar{a}_t = \frac{\sum_a a X_{a,t}}{X_t} \tag{III.1}$$

with squared *standard error*

$$\mathrm{SE}_t = \frac{\sum_a (a - \bar{a}_t)^2 X_{a,t}}{X_t} \tag{III.2}$$

Likewise, the *average extinction age* at time t is defined as

$$\bar{a}_{e,t} = \frac{\sum_a a E_{a,t}}{E_t} \tag{III.3}$$

The *survival distribution function* for the a-age class is expressed as $P_s(a) = \mathbf{Pr}(A > a)$, where $\mathbf{Pr}$ is read as 'the probability that', and the capital

letter A denotes a random variable defined as the age at which an individual die. The survival at an age a, given the survival at the previous year, is denoted as $s(a) = \mathbf{Pr}(A > a | A > a - 1)$ and is referred to as the *yearly survival probability*. Likewise, the *probability of extinction* at an age a is denoted by $p_e(a) = \mathbf{Pr}(A = a) = P_s(a - 1) - P_s(a)$. The survival distribution function is prescribed by the Bayes rule as $P_s(a) = s(a)P_s(a - 1)$, for $a = 1, 2 \ldots$, and $P_s(0) = 1$, or, after recursive substitutions,

$$P_s(a) = \prod_{k=1}^{a} s(k) \tag{III.4}$$

III.2 The extinction model

At each year, each individual in the a-age class survives with probability $s(a)$ and dies with probability $e(a) = 1 - s(a)$, where $e(a)$ is the *yearly extinction probability*. Then, the expected extinction rate is given by Equation (III.5):

$$\hat{E}_t = \sum_a e(a)X_{a,t} \tag{III.5}$$

where the hat $(\hat{x})$ is used to denote expectation. Because tracking the age structure in a spatial explicit model is not efficient, it is desirable to be able to predict the extinction rate from total density without knowing the age structure. The following expression for the extinction rate is more desirable:

$$\hat{E}_t = e(\bar{a}_t)X_t \tag{III.6}$$

This relation holds only if the yearly survival function is linear in a. Under this constraint, the simplest model for the yearly survival function is a constant, say

$1 - p$, in which case the survival density function corresponds to a geometric density function with one parameter p, the probability of dying each year. Although easy to implement, the geometric model may not be realistic because there is a small, yet positive chance that an individual live for ages significantly larger than the maximum longevity, and because the extinction probability of a younger individual is always larger than the extinction probability of an older one, which might not be always the case for real plants such as saltcedar. A more realistic model is obtained for non-constant yearly survival function.

The linear model can be parameterized in terms of the maximum longevity $a_{\max}$ and the extinction probability during the first year q, i.e.,

$$s(a) = q\frac{a_{\max} - a}{a_{\max} - 1} \tag{III.7}$$

Replacing this expression in Equation (III.4), the survival distribution function results:

$$P_s(a) = \left(\frac{q}{a_{\max} - 1}\right)^a \frac{(a_{\max} - 1)!}{(a_{\max} - 1 - a)!} \tag{III.8}$$

for $a = 0, 1, \ldots, a_{\max}$. Consequently, the probability of dying at the exact age a becomes:

$$p_e(a) = \left(1 - q\frac{a_{\max} - a}{a_{\max} - 1}\right)\left(\frac{q}{a_{\max} - 1}\right)^{a-1} \frac{(a_{\max} - 1)!}{(a_{\max} - a)!} \tag{III.9}$$

for $a = 1, 2, \ldots, a_{\max}$. Since this probability density function converges to the geometric distribution as $a_{\max}$ tend to infinity, I refer to it as a *truncated geometric distribution*. Plots of this distribution are shown in Figure III.2 for several values of q and $a_{\max} = 100$.
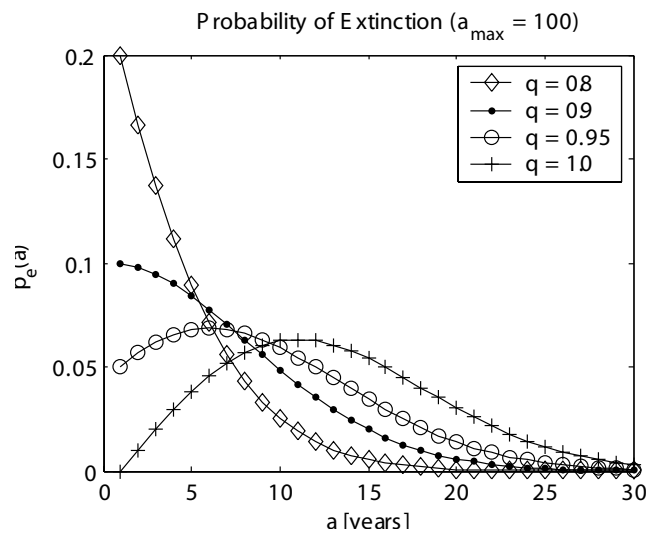
Figure III.1: Plots of the truncated geometric distribution for several values of the probability of success for the first trial (q) and maximum number of success $(a_{\max})$ of 100.

III.3 Average age update

The dynamical equations for the a-age class can be written as:

$$X_{a,t} = X_{a-1,t-1} + \delta_{a,1}C_{t-1} - E_{a-1,t-1} \tag{III.10}$$

where $\delta_{n,m}$ is the Kronecker delta (i.e., $\delta_{n,m} = 1$, for $n = m$ and $\delta_{n,m} = 0$ otherwise), and the sum over all ages yields

$$X_t = X_{t-1} + C_{t-1} - E_{t-1} \tag{III.11}$$

Using these expressions with the definitions of Equations III.1 and III.3, results in the recursive expression for the average age:

$$\bar{a}_t = 1 + \left(1 - \frac{C_{t-1}}{X_t}\right)\bar{a}_{t-1} - (\bar{a}_{e,t-1} - \bar{a}_{t-1})\frac{E_{t-1}}{X_t} \tag{III.12}$$

for $X_t > 0$. Furthermore, using the expected extinction rates in Equation III.3, it can be shown that the third term in this expression is proportional to the standard error (Eq. III.2) and, after algebraic manipulation, it results in the recursive formula

$$\bar{a}_t = 1 + \left(1 - \frac{C_{t-1}}{X_t}\right)\bar{a}_{t-1} - \frac{q\mathrm{SE}_t E_{t-1}}{(a_{\max} - 1)X_t} \tag{III.13}$$

where rightmost term can be neglected for large values of $a_{\max}$. For small $a_{\max}$, the term SE_t is approximated by the variance of the truncated geometric distribution.

III.4 Reproductive maturity population

The population in the reproductive maturity age is based on the age-structured density. An explicit expression for the age structure can be

obtained by using expected extinction values in Eq. III.10, so that

$$X_{a,t} = s(a-1)X_{a-1,t-1} + \delta_{a,1}C_{t-1}$$
$$= C_{t-a} \prod_{k=1}^{a-1} s(k)$$
$$= C_{t-a}P_s(a-1)$$

Then, the *reproductive maturity density* can be determined as

$$M_t = X_t - \sum_{a=1}^{a_{\text{mat}}-1} P_s(a-1)C_{t-a} \qquad \text{(III.14)}$$

where a_{mat} is the minimum age of reproductive maturity.

III.5   Land cover change counterpart

The first step consists of expressing the fractional densities in terms of the fraction of sites occupied by native species alone x, invasive species alone y, both species together z, and the fraction of empty sites w. This is accomplished by making the variable substitutions $\tilde{X}_t = x_t + z_t$, $\tilde{Y}_t = y_t + z_t$ and $w_t = 1 - x_t - y_t - z_t$ in the system of Equations (5.6), and then defining the common terms of both equations as z_{t+1}. Therefore, the first equation of the

system can be expressed as:

$$
\begin{aligned}
\tilde{X}_{t+1} ={}& s_x x_t + s_x z_t + c_x[1 - x_t - z_t - \gamma_x(y_t + z_t)] \\
={}& s_x x_t + s_x z_t + c_x w_t + (1 - \gamma_x)c_x y_t - \gamma_x c_x z_t \\
={}& s_x x_t + s_x(s_y + e_y)z_t + c_x(c_y + 1 - c_y)w_t + (1 - \gamma_x)c_x y_t - \gamma_x c_x z_t \\
={}& s_x x_t + s_x e_y z_t + c_x(1 - c_y)w_t - (1 - \gamma_y)c_y x_t + \gamma_y c_y z_t \\
& + s_x s_y z_t + c_x c_y w_t + (1 - \gamma_x)c_x y_t + (1 - \gamma_y)c_y x_t - \gamma_x c_x z_t - \gamma_y c_y z_t \\
={}& (s_x - (1 - \gamma_y)c_y)x_t + (s_x e_y + \gamma_y c_y)z_t + c_x(1 - c_y)w_t \\
& + (1 - \gamma_y)c_y x_t + (1 - \gamma_x)c_x y_t + (s_x s_y - \gamma_x c_x - \gamma_y c_y)z_t + c_x c_y w_t
\end{aligned}
$$

where the appropriate conditions have been applied. Proceeding in the same way with the second equation yields:

$$
\begin{aligned}
\tilde{Y}_{t+1} ={}& (s_y - (1 - \gamma_x)c_x)y_t + (s_y e_x + \gamma_x c_x)z_t + c_y(1 - c_x)w_t \\
& + (1 - \gamma_y)c_y x_t + (1 - \gamma_x)c_x y_t + (s_x s_y - \gamma_x c_x - \gamma_y c_y)z_t + c_x c_y w_t
\end{aligned}
$$

If the common part of both equations is defined as the joint occupancy term, z_{t+1}, then the dynamical equations of the fractional densities can be expressed as:

$$
x_{t+1} = (s_x - (1 - \gamma_y)c_y)x_t + (s_x e_y + \gamma_y c_y)z_t + c_x(1 - c_y)w_t \tag{III.15}
$$

$$
y_{t+1} = (s_y - (1 - \gamma_x)c_x)y_t + (s_y e_x + \gamma_x c_x)z_t + c_y(1 - c_x)w_t \tag{III.16}
$$

$$
z_{t+1} = (1 - \gamma_y)c_y x_t + (1 - \gamma_x)c_x y_t + (s_x s_y - \gamma_x c_x - \gamma_y c_y)z_t + c_x c_y w_t \tag{III.17}
$$

and, consequently, the fraction of empty sites results in:

$$
w_{t+1} = e_x x_t + e_y y_t + e_x e_y z_t + (1 - c_x)(1 - c_y)w_t \tag{III.18}
$$

The second step consists of splitting the proportion of jointly occupied sites into two parts, one where the native is canopy-dominant (z_x) and other where the invasive species is canopy-dominant (z_y). This is accomplished by making the variable substitution $z_t = z_{x,t} + z_{y,t}$ and by forcing the coefficients of the resulting system to reflect the conditions outlined in Section 5.3. For example, the term $(s_x e_y + \gamma_y c_y)z_t$ in Equation (III.15) is expressed as $(s_x e_y + \gamma_y c_y/\delta)z_{x,t} + s_x e_y z_{t,y}$ because it reflects the fact that the competitive effect on the invasive species (γ_y) does not play a role in driving the change from canopy-dominant invasive species (z_y) into native species alone (x), but it does play a role in driving the change from canopy-dominant native ($z_{x,t}$) into native species alone (x). Note that for the above term to be equivalent to that in Equation (III.15), the relations $z_{x,t} = \delta z_t$ and $z_{y,t} = (1 - \delta)z_t$ must hold, and hence δ defines the proportion jointly occupied sites where the native species dominates the canopy. Therefore, the application of the above conditions to equations Equation (III.17) through (III.18) yields the following dynamical system of five state variables:

$$x_{t+1} = (s_x - (1 - \gamma_y)c_y)x_t + (s_x e_y + \gamma_y c_y/\delta)z_{x,t} + s_x e_y z_{y,t} + c_x(1 - c_y)w_t$$

$$y_{t+1} = (s_y - (1 - \gamma_x)c_x)y_t + s_y e_x z_{x,t} + (s_y e_x + \gamma_x c_x/(1 - \delta))z_{y,t} + c_y(1 - c_x)w_t$$

$$z_{x,t+1} = (1 - \gamma_y)c_y x_t + (s_x s_y - \gamma_y c_y/\delta)z_{x,t} + \delta c_x c_y w_t \qquad \text{(III.19)}$$

$$z_{y,t+1} = (1 - \gamma_x)c_x y_t + (s_x s_y - \gamma_x c_x/(1 - \delta))z_{y,t} + (1 - \delta)c_x c_y w_t$$

$$w_{t+1} = e_x x_t + e_y y_t + e_x e_y z_{x,t} + e_x e_y z_{y,t} + (1 - c_x)(1 - c_y)w_t$$

The last step consists of merging states with similar above-canopy cover. The idea here is to evaluate the conditional probabilities of observing a land cover

at a given time step given the observed land cover at previous time step, where the fractions $a = x + z_x$, $b = y + z_y$ and w at initial time step are considered as prior probabilities. Let X, Y, Z_x, Z_y and W denote the events of observing the land cover types: native only, invasive only, both with canopy dominating native, both with canopy-dominating invasive and clear, respectively. Let $A = X \bigcup Z_x$ denote the event of observing the native species from above, and $B = Y \bigcup Z_y$ denote the event of observing the invasive species from above. Then, the probability of observing a land cover (LC) i at time $t + 1$ given that a land cover j has been observed at time t, is denoted by $p_{i,j} = P(LC_{t+1} = j | LC_t = i)$. Here I just evaluate $p_{a,a}$ and $p_{a,b}$ for the sake of illustrating the idea and present the results for the other probabilities:

$$
\begin{aligned}
p_{a,a} &= P(A|A) = P(A|X \cup Z_x) \\
&= P(X \cup Z_x|A) \frac{P(A)}{P(X \cup Z_x)} \\
&= \frac{P(X|A)P(A) + P(Z_x|A)P(A)}{P(X \cup Z_x)} \\
&= \frac{P(A|X)P(X) + P(A|Z_x)P(Z_x)}{P(X) + P(Z_x)} \\
&= \frac{P(X|X)P(X) + P(Z_x|X)P(X) + P(X|Z_x)P(Z_x) + P(Z_x|Z_x)P(Z_x)}{P(X) + P(Z_x)} \\
&= \frac{(s_x - (1 - \gamma_y)c_y)x + (1 - \gamma_y)c_y x + (s_x e_y + \gamma_y c_y/\delta)z_x + (s_x s_y - \gamma_y c_y/\delta)z_x}{x + z_x} \\
&= \frac{s_x x + (s_x e_y + s_x s_y)z_x}{x + z_x} = s_x
\end{aligned}
$$

where I have used Bayes rule to go from line one to line two and from line three to

line four. Likewise,

$$
\begin{aligned}
p_{a,b} &= P(B|A) = P(B|X \cup Z_x) \\
&= P(X \cup Z_x|B)\frac{P(B)}{P(X \cup Z_x)} \\
&= \frac{P(X|B)P(B) + P(Z_x|B)P(B)}{P(X \cup Z_x)} \\
&= \frac{P(B|X)P(X) + P(B|Z_x)P(Z_x)}{P(X) + P(Z_x)} \\
&= \frac{P(Y|X)P(X) + P(Z_y|X)P(X) + P(Y|Z_x)P(Z_x) + P(Z_y|Z_x)P(Z_x)}{P(X) + P(Z_x)} \\
&= \frac{0x + 0x + e_x s_y z_x + 0z_x}{x + z_x} \\
&= e_x s_y \frac{z_x}{x + z_x} = \lambda_x e_x s_y
\end{aligned}
$$

where λ_x is the probability that the observed native species is occluding the invasive species in the understory.

Proceeding similarly for the other land cover change probabilities results in the following land cover change model, here expressed in the form of a system of linear equations:

$$
a_{t+1} = s_x a_t + \lambda_y s_x e_y b_t + c_x(1 - (1 - \delta)c_y)w_t
$$

$$
b_{t+1} = \lambda_x e_x s_y a_t + s_y b_t + c_y(1 - \delta c_x)w_t \tag{III.20}
$$

$$
w_{t+1} = [(1 - \lambda_x)e_x + \lambda_x e_x e_y]a_t + [(1 - \lambda_y)e_y + \lambda_y e_x e_y]b_t + (1 - c_x)(1 - c_y)w_t
$$

where the new parameters $\lambda_x = z_x/(x + z_x)$ and $\lambda_y = z_y/(y + z_y)$ represent the probability that the observed species is occluding the other species in the understory.

Bibliography

Adams, J., Smith, M., and Gillespie, A. (1993). Imaging spectroscopy: Interpretation based on spectral mixture analysis. *Remote Geochemical Analysis: Elemental and Mineralogical Composition*, **7**, 145–166.

Adams, J. B., Sabol, D. E., Kapos, V., Filho, R. A., Roberts, D. A., Smith, M. O., and Gillespie, A. R. (1995). Classification of multispectral images based on fractions of endmembers: Application to land-cover change in the Brazilian Amazon. *Remote Sensing of Environment*, **52**, 137–154.

Alpert, P., Bone, E., and Holzapfel, C. (2000). Invasiveness, invasibility and the role of environmental stress in the spread of non-native plants. *Perspectives in Plant Ecology, Evolution and Systematics*, **3**(1), 52–66.

Ansley, R., Huddle, J., and Kramp, B. (1997). Mesquite ecology. *Brush Sculptors: Innovations for Tailoring Brushy Rangelands to Enhance Wildlife Habitat and Recreational Value, TAMU Agricultural Research & Extension Center, San Angelo*, pages 21–25.

Atkinson, P. M., Cutler, M. E. J., and Lewis, H. (1997). Mapping sub-pixel proportional land cover with AVHRR imagery. *Int. J. Remote Sensing*, **18**(4), 917–935.

Auble, G., Friedman, J., and Scott, M. (1994). Relating riparian vegetation to present and future streamflows. *Ecological Applications*, **4**(3), 544–554.

Baum, B. R. (1967). Introduced and naturalized tamarisks in the United States and Canada. *Bayleya*, **15**, 19–25.

Binaghi, E., Brivio, P. A., Ghezzi, P., and Rampini, A. (1999). A fuzzy set-based assessment of soft classification. *Pattern Recognition Letters*, **20**, 935–948.

Bini, D. A., Higham, N. J., and Meini, B. (2005). Algorithms for the matrix pth root. *Numerical Algorithms*, **39**, 349–378.

Borel, C. and Gerstl, S. (1994). Nonlinear spectral mixing models for vegetative and soil surfaces. *Remote Sensing of Environment*, **47**, 403–416.

Brotherson, J. D. and Field, D. (1987). *Tamarix*: Impacts of a successful weed. *Rangelands*, **9**, 110–112.

Busch, D. E. and Smith, S. D. (1995). Mechanisms associated with decline of woody species in riparian ecosystems of the southwestern U.S. *Ecological Monography*, **65**(3), 347–370.

Canty, J. M. and Nielsen, A. A. (2008). Automatic radiometric normalization of multitemporal satellite imagery with the iterativelly re-weighted MAD transformation. *Remote Sensing of Environment*, **112**(3), 1025–1036.

Canty, M. (2006). *Image Analysis, Classification and Change Detection in Remote Sensing: With Algorithms in ENVI/IDL*. CRC Press.

Carpenter, G. A., Gopal, S., Martens, S., and Woodcock, C. E. (1999). A neural network method for mixture estimation for vegetation mapping. *Remote Sensing of Environment*, **70**, 138–152.

Carruthers, R., Anderson, G., DeLoach, J., Knight, J., Ge, S., and Gong, P. (2006). Remote sensing of saltcedar biological control effectiveness. *USDA Forest Service*, pages 50–56.

Chang, C.-I. and Heinz, D. C. (2000). Constrained sub-pixel target detection of remotely sensed imagery. *IEEE Transaction on Geoscience and Remote Sensing*, **38**(3), 1114–1159.

Chesson, P. (2000). Mechanisms of maintenance of species diversity. *Annual Review of Ecology and Systematics*, **31**, 343–358.

Cleverly, J. R., Smith, S. D., Sala, A., and Devitt, D. A. (1997). Invasive capacity of *Tamarix ramosissima* in a Mojave Desert floodplain: The role of drought. *Oecologia*, **111**, 12–18.

Cleverly, J. R., Dahm, C. N., Thibault, J. R., Gilroy, D. J., and A., C. J. E. (2002). Seasonal estimates of actual evapo-transpiration from *Tamarix ramosissima* stands using three-dimensional eddy covariance. *Journal of Arid Environments*, **52**, 181–197.

Cohen, J. (1960). A coefficient of agreement for nominal scales. *Educational and Psychological Measurement*, **20**(1), 37–46.

Congalton, R. G. (1991). A review of assessing the accuracy of classifications of remotely sensed data. *Remote Sensing of Environment*, **37**, 35–46.

Congalton, R. G. and Green, K. (1999). *Assessing the Accuracy of Remotely Sensed Data: Principles and Practices*. Lewis, Boca Raton, FL.

Cross, A. M., Settle, J. J., Drake, N. A., and Paivinen, R. T. M. (1991). Subpixel measures of tropical forest cover using AVHRR data. *International Journal of Remote Sensing*, **12**, 1119–1129.

CSR (2007). Forgotten river: Datasets compiled for the U.S. Army Corps of Engineers Forgotten River watershed management plan: Ft. Quitman to Presidio, Texas. On line: magic.csr.utexas.edu/Project/ForgottenRiver/Index.htm. Viewed 17 March 2008.

Daniel, W. W. (1990). *Applied Nonparametric Statistics*, chapter Spearman rank correlation coefficient, pages 358–364. Duxbury, Canada.

de Almeida, C. M., Batty, C., Monteiro, A. M. V., Cámara, G., Soares-Filho, B. S., Cerqueira, G. C., and Pennachin, C. L. (2003). Stochastic cellular automata modeling of urban land use dynamics: Empirical development and estimation. *Computer, Environment and Urban Systems*, **27**, 481–509.

DeLoach, C. J., Carruthers, R. I., Dudley, T. L., Eberts, D., Kazmer, D. J., Knutson, A. E., Bean, D. W., Knight, J., Lewis, P. A., Milbrath, L. R., Tracy, J. L., Tomic-Carruthers, N., Herr, J. C., Abbott, G., Prestwich, S., Glenn, H., Everitt, J. H., Thompson, D. C., Mityaev, I., Jashenko, R., Li, B., Sobhian, R., Kirk, A., Robbins, T., and Delfosse, E. S. (2004). First results for control of saltcedar (*Tamarix* spp.) in the open field in the Western United States. In R. Cullen, editor, *XI International Symposium on Biological Control of Weeds*, pages 505–513, Canberra, Australia.

Di Tomaso, J. M. (1998). Impact, biology, and ecology of saltcedar (*Tamarix* spp.) in the Southern United States. *Weed Technology*, **12**, 326–336.

Drake, J. A., Mooney, H. A., Castri, F. D., Groves, R. H., Kruger, F. J., Aejmamek, M., and Williamson, M. (1989). *Biological Invasions: A Global Perspective*. John Wiley & Sons, Chichester.

Everitt, B. L. (1980). Ecology of saltcedar: A plea for research. *Environmental Geology*, **3**, 77–84.

Everitt, B. L. (1998). Chronology of the spread of tamarisk in the central rio grande. *Wetlands*, **18**(4), 658–668.

Everitt, J. (1996). Using spatial information technologies to map chinese tamarisk (*Tamarix chinensis*) infestations. *Weed Science*, pages 194–201.

Everitt, J. H. and DeLoach, C. J. (1990). Remote sensing of chinese tamarisk (*Tamarix chinensis*) and associated vegetation. *Weed Science*, **38**, 273–278.

Everitt, J. H., Escobar, D. E., Alaniz, M. A., Villareal, R., and Davis, M. R. (1992). Distinguishing brush and weeds on rangelands using video remote sensing. *Weed Technology*, **6**, 913–921.

Fisher, P. and Pathirana, S. (1990). An evaluation of fuzzy memberships of land cover classes in the suburban zone. *Remote Sensing of Environment*, **34**, 121–132.

Foody, G. M. (1995). Cross-entropy for the evaluation of the accuracy of a fuzzy land cover classification with fuzzy ground data. *ISPRS Journal of Photogrammetry and Remote Sensing*, **80**, 185–201.

Foody, G. M. (2002). Status of land cover classification accuracy assessment. *Remote Sensing of Environment*, **80**, 185–201.

Friedman, J. M., Auble, G. T., Shafroth, P. B., Scott, M. L., Merigliano, M. F., Freehing, M. D., and Griffin, E. R. (2005). Dominance of non-native riparian trees in western USA. *Biological Invasions*, **7**, 747–751.

Gaskin, J. F. and Schaal, B. A. (2002). Hybrid tamarix widespread in US invasion and undetected in native asian range. *Proc. of the National Academy of Science*, **99**(12), 11256–11259.

Gillespie, A. R. (1992). Spectral mixture analysis of multi-spectral thermal infrared images. *Remote Sensing of Evironment*, **42**, 137–145.

Glenn, N., Mundt, J., Weber, K., Prather, T., Lass, L., and Pettingill, J. (2005). Hyperspectral data processing for repeat detection of small infestations of leafy spurge. *Remote Sensing of Environment*, **95**(3), 399–412.

Gopal, S. and Woodcock, C. E. (1994). Theory and methods for accuracy assessment of thematic maps using fuzzy sets. *Photogrammetric Engineering and Remote Sensing*, **60**(2), 181–188.

Gotelli, N. J. (2001). *A Primer of Ecology*. Sinauer Associates, Inc., Sunderland, MA.

Green, K. and Congalton, G. (2004). *Remote Sensing and GIS Accurcacy Assessment*, chapter An Error Matrix Approach to Fuzzy Accuracy Assessment: The NIMA Geocover Project, pages 163–172. CRC Press, Boca Raton.

Gutman, G. and Ignatov, A. (1998). The derivation of the green vegetation fraction from NOAA/AVHRR data for use in numerical weather prediction models. *International Journal of Remote Sensing*, **60**(2), 181–188.

Hamada, Y., Stow, D., Coulter, L., Jafolla, J., and Hendricks, L. (2007). Detecting tamarisk species (*Tamarix* spp.) in riparian habitats of Southern California using high spatial resolution hyperspectral imagery. *Remote Sensing of Environment*, **109**(2), 237–248.

Harris, S. (1999). Forgotten River: Rio Grande streamflow and the availability of water for restoration-Ft. Quitman to Candelaria. *Rio Grande Restoration, Albuquerque, NM. February*, **10**. Online http://www.riogranderestoration.com/index.html. Viewed 1 February 2007.

Hart, C. R., White, L. D., McDonald, A., and Sheng, Z. (2005). Saltcedar control and water salvage on the Pecos River, Texas, 1999-2003. *Journal of Environmental Management*, **75**, 399–409.

Hedrick, P. (2005). *Genetics of Populations*. Jones & Bartlett Publishers.

Heinz, D. C. and Chang, C.-I. (2001). Fully constrained least square linear spectral unmixing analysis method for matherial quantification in hyperspectral imagery. *IEEE Transactions on Geoscience and Remote Sensing*, **39**(3), 529–545.

Hengeveld, R. (1989). *Dynamics of biological invasions*. Springer.

Higgins, S., Richardson, D., and Cowling, R. (1996). Modeling invasive plant spread: The role of plant-environment interactions and model structure. *Ecology*, **77**(7), 2043–2054.

Higgins, S. I. and Richarson, D. M. (1996). A review of models of alien plant spread. *Ecological Modeling*, **87**, 249–265.

Howe, W. H. and Knopf, F. L. (1991). On the imminent decline of Rio Grande cottonwoods in central New Mexico. *The Southwestern Naturalist*, **36**(2), 218–224.

Hu, Y. H., Lee, H. B., and Scarpace, F. L. (1999). Optimal linear spectral unmixing. *IEEE Transactions on Geoscience and Remote Sensing*, **37**(1), 639–644.

Huang, D., Knyazikhin, Y., Dickinson, R. E., Rautianen, M., Stenberg, P., Disney, M., Lewis, P., Cescatti, A., Tian, Y., Verhoef, W., Martonchik, J. V., and Myneni, R. B. (2007). Canopy spectral invariants for remote sensing and model applications. *Remote Sensing of Environment*, **106**, 106–122.

Hunt, E. R., Everitt, J. H., Ritchie, J. C., Moran, M. S., Booth, D. T., Anderson, G. L., Clark, P. E., and Seyfried, M. S. (2003). Application and research using remote sensing for range management. *Photogrammetric Engineering & Remote Sensing*, **69**(6), 675–693.

ISFC (2008). Invasive species forecasting system. Online: http://isfs.gsfc.nasa.gov. Viewed 16-July-2008.

Joshi, C., de Leeuw, J., and Van Duren, I. C. (2004). Remote sensing and GIS applications for mapping and spatial modelling of invasive species. In M. O. Altan, editor, *XXth ISPRS Congress*, volume XXXV part B7, pages 669–677, Istambul, Turkey. International Society for Photogrammetry and Remote Sensing.

Katul, G. G., Porporato, A., Nathan, R., Siqueira, M., Soons, M. B., Poggi, D., Horn, H. S., and Levin, S. A. (2005). Mechanistic analyitical models for long-distance seed dispersal by wind. *The American Naturalist*, **166**(3), 368–381.

Kawasaki, K., Takasu, F., Caswell, H., and Shiguesada, N. (2006). How does stochasticity in colonization accelerate the speed of invasion in a cellular automaton model. *Ecological Research*, **21**, 334–345.

Keshava, N. and Mustard, J. F. (2002). Spectral unmixing. *IEEE Signal Processing Magazine*, **19**(1), 44–57.

Keymer, J. E., Marquet, P. A., and Johnson, A. R. (1998). Pattern formation in a patch occupancy metapopulation model: A cellular automata approach. *J. Theor. Biology*, **21**, 334–345.

Kruse, F. A., Lefkoff, A. B., Boardman, J. B., Heidebrecht, K. B., Shapiro, A. T., Barloon, P. J., and Goetz, A. F. H. (1993). The spectral image processing system (SIPS) - interactive visualization and analysis of imaging spectrometer data. *Remote Sensing of Environment*, **44**, 145–163.

Kuzera, K. and Pontius Jr, R. (2004). Categorical coefficients for assessing soft-classified maps at multiple resolutions. In *Conference proceedings of the joint meeting of The Fifteenth Annual Conference of The International Environmetrics Society and The Sixth Annual Symposium on Spatial Accuracy Assessment in Natural Resources and Environmental Sciences. Portland ME*, volume 28.

Lass, L. W., Prather, T. S., Glenn, N. F., Weber, K. T., Mundt, J. T., and Pettingill, J. (2005). A review of remote sensing of invasive weeds and example of the early detection of spotted knapweed (*Centaurea maculosa* and babysbreath (*Gypsophila paniculata*) with a hyperspectral sensor. *Weed Science*, **53**, 242–251.

Latifovic, R. and Olthof, I. (2004). Accuracy assessment using sub-pixel fractional error matrices of global land cover products derived from satellite data. *Remote Sensing of Environment*, **90**(2), 153–165.

Lewis, H. G. and Brown, M. (2001). A generalized confusion matrix for assessing area estimates from remotely sensed data. *International Journal of Remote Sensing*, **22**, 3223–3235.

Lewis, P. and Disney, M. (2007). Spectral invariants and scattering across multiple scales from within-leaf to canopy. *Remote Sensing of Environment*, **109**, 196–206.

Liu, W. and Wu, E. Y. (2005). Comparison of nonlinear mixture models: Sub-pixel classification. *Remote Sensing of Environment*, **94**, 145–154.

Lockwood, J. L., Hoopes, M. F., and Marchetti, M. P. (2007). *Invasion Ecology*. Blackwell Publishing, MA.

Lu, D., Mausel, P., Brondizio, E., and Moran, E. (2004). Change detection techniques. *Int. J. Remote Sensing*, **25**(12), 2365–2407.

Marco, D. E., Páez, S. A., and Cannas, S. A. (2002). Species invasiveness in biological invasions: A modelling approach. *Biological Invasions*, **4**, 193–205.

Merritt, D. and Cooper, D. (2000). Riparian vegetation and channel change in response to river regulation: A comparative study of regulated and unregulated streams in the Green River Basin, USA. *Regulated Rivers: Research & Management*, **16**(6), 543–564.

Meyn, S. P. and Tweedie, R. L. (2008). *Markov Chains and Stochastic Stability*. Cambridge University Press, MA, 2nd edition.

Miao, X., Gong, P., Swope, S., Ruiliang, P., Carruthers, R., Anderson, A., Heaton, J. S., and Tracy, C. R. (2006). Estimation of yellow starthisle abundance through CASI-2 hyperspectral imagery using linear spectral mixture models. *Remote Sensing of Environment*, **101**, 329–341.

Milton, E. J. (1999). Image endmembers and the scene model. *Canadian Journal of Remote Sensing*, **25**(2), 112–120.

Morisette, J. T., Jarnevich, C. S., Ullah, A., Cai, W., Pedelty, J. A., Gentle, J. E., Stohlgren, T. J., and Schnase, J. L. (2006). A tamarisk habitat suitability map for the continental United States. *Front Ecol Environ*, **4**(1), 11–17.

National Invasive Species Council (2001). Management plan: Meeting the invasive species challenges. on Line: http://www.invasivespecies.gov/council/mp.pdf. Viewed September 24, 2007.

Nehrbass, N., Winkler, E., Müllerová, J., Pergl, J., Pyšek, P., and Perglová, I. (2007). A simulation model of plant invasion: Long-distance dispersal determines the pattern of spread. *Biological Invasions*, **9**(4), 383–395.

Nielsen, A. A. (2007). The regularized iteratively reweighted MAD method for change detection in multi- and hyperspectral data. *IEEE transaction on image processing*, **16**(2), 463–478.

Noy-Meir, I. (1974). Desert ecosystems: Higher trophic levels. *Annual Review of Ecology and Systematics*, **5**(1), 195–214.

Okeke, F. and Karnieli, A. (2006). Methods for fuzzy classification and accuracy assessment of historical aerial photographs for vegetation change analyses. Part i: Algorithm development. *International Journal of Remote Sensing*, **27**(1), 153–176.

Owens, M. and Moore, G. (2007). Saltcedar water use: Realistic and unrealistic expectations. *Rangeland Ecology & Management*, **60**(5), 553–557.

Ozdogan, M. and Woodcock, C. E. (2006). Resolution dependent errors in remote sensing of cultivated areas. *Remote Sensing of Environment*, **103**, 203–217.

Pearce, C. M. and Smith, D. G. (2003). Saltcedar: Distribution, abundance, and dispersal mechanisms, Northern Montana, USA. *Wedlands*, **23**(2), 215–228.

Plaza, A., Perez, P., and Plaza, J. (2004). A quantitative and comparative analysis of endmember extraction algorithms from hyperspectral data. *IEEE Transactions on Geoscience and Remote Sensing*, **42**(3), 650–663.

Pontius Jr, R. G. (2002). Statistical methods to partition effects of quantity and location during comparison of categorical maps at multiple resolutions. *Photogrammetric Engineering and Remote Sensing*, **68**(10), 1041–1049.

Pontius Jr, R. G. and Cheuk, M. L. (2006). A generalized cross-tabulation matrix to compare soft-classified maps at multiple resolutions. *International Journal of Geographical Information Science*, **20**(1), 1–30.

Pontius Jr, R. G. and Connors, J. (2006). Expanding the conceptual, mathematical and practical methods for map comparison. In *Spatial Accuracy Meeting*, Lisbon, Portugal. available from www. clarku. edu/∼rpontius.

Pratt, R. B. and Black, R. A. (2006). Do invasive tree have a hydraulic advantage over native trees? *Biological Invasions*, **8**(6), 1331–1341.

Rees, M. and Paynter, Q. (1997). Biological control of Scotch broom: Modelling the determinants of abundance and the potential impact of introduced insect herbivores. *Journal of Applied Ecology*, **34**(5), 1203–1221.

Reynolds, J., Kemp, P., Ogle, K., and Fernández, R. (2004). Modifying the pulse–reserveparadigm for deserts of north america: Precipitation pulses, soil water, and plant responses. *Oecologia*, **141**(2), 194–210.

Richards, J. A. and Jia, X. (1999). *Remote Sensing Digital Image Analysis*. Springer-Verlag, Berlin, 3rd edition.

Roberts, D. A., Smith, M. O., and Adams, J. B. (1993). Green vegetation, non-photosynthetic vegetation and soils in AVIRIS data. *Remote Sensing of Environment*, **44**, 255–269.

Roberts, D. A., Batista, G. T., Pereira, J. L. G., Waller, E. K., and Nelson, B. W. (1998). *Remote Sensing Change Detection: Environmental Monitoring Methods and Applications*, chapter Chage identification using multitemporal spectral mixture analysis: applications in eastern Amazonia, pages 137–161. Ann Arbor Press, Chelsea, MI.

Rogan, J., Frankling, J., and Roberts, D. A. (2002). A comparison of methods for monitoring multitemporal vegetation change using tematic mapper imagery. *Remote Sensing of Environment*, **80**, 143–156.

Rumelhart, D. E., Hinton, G. E., and Williams, R. J. (1986). Learning representations by back-propagating errors. *Nature*, **323**, 533–536.

Scanlon, T., Caylor, K., Levin, S., and Rodriguez-Iturbe, I. (2007). Positive feedbacks promote power-law clustering of kalahari vegetation. *Nature*, **449**(7159), 209–212.

Schwinning, S., Sala, O., Loik, M., and Ehleringer, J. (2004). Thresholds, memory, and seasonality: Understanding pulse dynamics in arid/semi-arid ecosystems. *Oecologia*, **141**(2), 191–193.

Scott, R., James Shuttleworth, W., Goodrich, D., and Maddock III, T. (2000). The water use of two dominant vegetation communities in a semiarid riparian ecosystem. *Agricultural and Forest Meteorology*, **105**(1-3), 241–256.

Shabanov, N. V., Lo, K., Gopal, S., and Myneni, R. B. (2005). Subpixel burn detection in moderate resolution imaging spectroradiometer 500-m data with ARTMAP neural networks. *Journal of Geophysical Research*, **110**, 1–17.

Shafroth, P. B., Cleverly, J. R., Dudley, T. L., Taylor, J. P., Van Riper III, C., Weeks, E. P., and Stuart, J. N. (2005). Control of tamarix in the Western United States: Implications for water slavage, wildlife use, and riparian restoration. *Environmental Management*, **35**(3), 231–246.

Shea, K. and Chesson, P. (2002). Community ecology theory as a framework for biological invasions. *Trends in Ecology and Evolution*, **17**(4), 170–176.

Sher, A. A., Marshall, D. L., and Taylor, J. P. (2002). Establishmet pattern of native *Populus* and *Salix* in the presence of invasive nonnative *Tamarix*. *Ecological Applications*, **12**(3), 760–772.

Silván-Cárdenas, J. L. and Wang, L. (2008a). Retrieval of sub-pixel tamarix canopy cover from landsat data: Assessing the in influence of multiple scattering. Submitted.

Silván-Cárdenas, J. L. and Wang, L. (2008b). Sub-pixel confusion-uncertainty matrix for the assessment of soft classifications. *Remote Sensing of Environment*, **112**, 1081–1095.

Silvertown, J., Holtier, S., Johnson, J., and Dale, P. (1992). Cellular automaton models of interspecific competition for space - the effect of pattern on process. *Journal of Ecology*, **80**, 527–534.

Small, C. (2004). The landsat ETM+ spectral mixing space. *Remote Sensing of Environment*, **93**, 1–17.

Smith, S. D., David, D. A., Sala, A., Cleverly, J. R., and Busch, D. E. (1998). Water relations of riparian plants from warm desert regions. *Wetlands*, **18**(4), 687–696.

Smolander, S. and Stenberg, P. (2005). Simple parameterizations of the radiation budget of uniform broadleaved and coniferous canopies. *Remote Sensing of Environment*, **94**(3), 355–363.

Stehman, S. V. and Czaplewski, R. L. (1998). Design and analysis for thematic map accuracy assessment: Fundamental principles. *Remote Sensing of Environment*, **64**, 331–344.

Stenquist, S. M. (2000). Salt cedar integrated weed management and the endangered speceis act. In N. R. Spenser, editor, *X Int. Symp. On Biol. Control of Weed*, pages 487–504.

Stromberg, J. (1998). Dynamics of fremont cottonwood (*Populus fremontii*) and saltcedar (*Tamarix chinensis*) populations along the San Pedro River, Arizona. *Journal of Arid Environments*, **40**, 133–155.

Tamarisk Coalition (2003). Impact of tamarisk infestation on the water resources of Colorado. Prepared for the Colorado Department of Natural Resources Colorado Water Conservation Board. On line: http://cwcb.state.co.us/Resource_Studies/Tamarisk_Study_2003.pdf.

Taylor, J. P. and McDaniel, C. K. (1998). Restoration of salt cedar (*Tamarirk* sp.)-infested floodplains on the bosque del apache national wildlife refuge. *Weed Technology*, **12**(2), 345–352.

Tickner, D. P., Angold, P. G., Gurnell, A. M., and Mountford, J. O. (2001). Riparian plant invasions: Hydrogeomorphological control and ecological impacts. *Progress in Physical Geography*, **25**(1), 22–52.

Townsend, P. A. (2000). A quantitative fuzzy approach to assess mapped vegetation classifcations for ecological applications. *Remote Sensing of Environment*, **72**, 253–267.

Turner, W., Spector, S., Gardiner, N., Fladeland, M., Sterling, E., and Steininger, M. (2003). Remote sensing for biodiversity science and conservation. *Trends in Ecology & Evolution*, **18**(6), 306–314.

US Department of Interior (2005). Press release. On line: www.doi.gov/news/05_News_Releases/050513b. Viewed 10 February 2007.

Vandermeer, J. H. and Goldberg, D. E. (2003). *Population Ecology: First Principles*. Princeton Unversity Press, Princeton, NJ.

Vitousek, P., DAntonio, C., Loope, L., and Westbrooks, R. (1996). Biological invasions as global environmental change. *American Scientist*, **84**(5), 468–478.

Warren, D. K. and Turner, R. (1975). Saltcedar (*Tamarix chinensis*) seed production, seedling establishment, and response to inundation. *J. of the Arizona Academy of Science*, **10**(3), 135–144.

Wolfram, S. (1984). Cellular automata as model of complexity. *Nature*, **311**, 419–424.

Woodcock, C. E. and Gopal, S. (2000). Fuzzy set theory and thematic maps: Accuracy assessment and area estimation. *International Journal of Geographical Information Science*, **14**(2), 153–172.

Young, J. A., Clements, C. D., and Harmon, D. (2004). Germination of seeds of tamarix ramosissima. *J. Range Manage.*, **57**, 475–481.

Zavaleta, E. (2000). The economic value of controlling an invasive shrub. *Ambio*, **29**, 462–467.

Zavaleta, E. S. and Royval, J. L. (2001). *Climate Change and the Susceptibility of U.S. Ecosystems to Biological Invasions: Two Cases of Expected Range Expansion*, chapter Wild Life Response to Climate Change: Northamerican Case Studies, pages 277–341. Island Press, Washington, D.C.

VITA

JOSE LUIS SILVAN CARDENAS was born in Nuevo Progreso, Campe-che, Mexico, in 1973. He received the B.C. Eng. degree in 1998 and the M.E. Eng. degree in 2002 from the Mexico National Autonomous University (UNAM). His main research interest at the time was image coding and image analysis based on models of the human visual system. He joined the Geography and Geomatic Research Center (CentroGeo), Mexico, in July of 2001. There, his research interests broadened to image classification for land cover mapping, automatic road detection from multi-spectral imagery and artificial intelligence techniques applied to image processing and geospatial modelling. In September of 2004 he moved to San Marcos, Texas for pursuing a Ph.D. in Geographic Information Sciences. He is the recipients of several academic recognitions including the "Alfoso Caso" medal which is granted yearly by UNAM to the most outstanding graduate student.

Permanent address: Prol. Aldama 188
Misiones de la Noria, Xochimilco
Mexico, D.F. 16010

This dissertation was typeset with LaTeX[†] by the author.

[†]LaTeX is a document preparation system developed by Leslie Lamport as a special version of Donald Knuth's TeX Program.